


REMOTE SENSING OF ARCTIC LANDSCAPE DYNAMICS

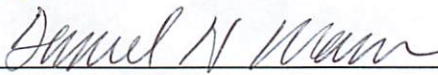
By

Benjamin M. Jones

RECOMMENDED:



Dr. Christopher D. Arp



Dr. Daniel H. Mann



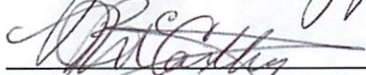
Dr. Vladimir E. Romanovsky



Dr. David L. Verbyla

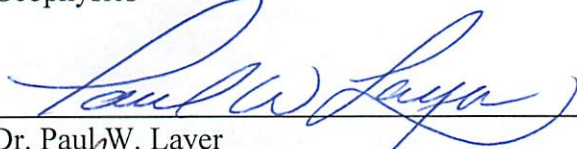


Dr. Guido Grosse, Advisory Committee Chair

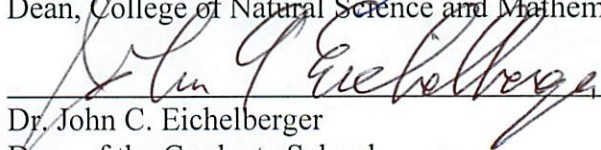


Dr. Paul J. McCarthy, Chair, Department of Geology and Geophysics

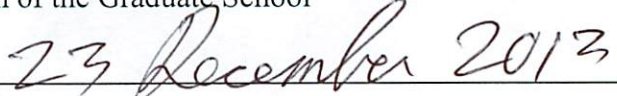
APPROVED:



Dr. Paul W. Layer
Dean, College of Natural Science and Mathematics



Dr. John C. Eichelberger
Dean of the Graduate School



Date

Remote Sensing of Arctic Landscape Dynamics

A
DISSERTATION

Presented to the Faculty
of the University of Alaska Fairbanks

in Partial Fulfillment of the Requirements
for the Degree of

DOCTOR OF PHILOSOPHY

By

Benjamin M. Jones, M.A., B.S.

Fairbanks, Alaska

December 2013

Abstract

Amplified warming in the Arctic has likely increased the rate of landscape change and disturbances in northern high latitude regions. Remote sensing provides a valuable tool for assessing the spatial and temporal patterns associated with arctic landscape dynamics over annual, decadal, and centennial time scales. In this dissertation, I focused on remote sensing studies associated with four primary components of arctic landscape change and disturbance: (1) permafrost coastline erosion, (2) thermokarst lake dynamics, (3) tundra fires, and (4) using repeat airborne LiDAR for the measurement of vertical deformation in an arctic coastal lowland landscape. By combining observations from several high resolution satellite images for a 9 km segment of the Beaufort Sea Coast between 2008 and 2012, I demonstrated that the report of heightened erosion at the beginning of the 2000s was equaled or exceeded in every year except 2010 and that the mean annual erosion rate was tightly coupled to the number of open water days and the number of storms. By combining historical aerial photographs from the 1950s and 1980s with recent high-resolution satellite imagery from the mid-2000s, I assessed the expansion and drainage of thermokarst lakes on the northern Seward Peninsula. I found that more than half of the lakes in the study area were expanding as a result of permafrost degradation along their margins but that the rate of expansion was fairly consistent (0.35 and 0.39 m/yr) between the 1950s and 1980s and 1980s and mid-2000s, respectively. However, it appeared that in a number of instances that expansion of lakes led to the lateral drainage and that over the 55-year study period the total lake area decreased by 24%. While these

studies highlight the utility of quantifying disturbance during the remotely sensed image archive period (~1950s to present) they are inherently limited temporally. Thus, I also demonstrated techniques in which field studies and remote sensing data could be combined to extend the identification of landscape disturbance events that occurred prior to the remote sensing archive. I identified two large regions indicative of past disturbance caused by tundra fires on the North Slope of Alaska, which doubled the delineated area of tundra fire disturbance on the North Slope over the last 100 to 130 years. I conclude the dissertation by demonstrating the utility of repeat airborne light detection and ranging (LiDAR) data for arctic landscape change studies, in particular vertical surface deformation, and provide momentum for going forward with this emerging technology for remote sensing of arctic landscape dynamics. The quantification of arctic landscape dynamics during and prior to the remote sensing archive is important for ongoing monitoring and modeling efforts of the positive and negative feedbacks associated with amplified Arctic climate change.

Table of Contents

	Page
Signature Page.....	i
Title Page....	iii
Abstract.....	v
Table of Contents	vii
List of Figures.....	xii
List of Tables	xiv
Preface.....	xv
Chapter 1: Introduction	1
1.1 Research topic background and dissertation overview	1
1.2 Rapid erosion of a permafrost coastline.....	4
1.3 Modern thermokarst lake dynamics in the continuous permafrost zone	5
1.4 Unrecognized tundra fire events on the North Slope of Alaska.....	6
1.5 Repeat airborne LiDAR for arctic landscape dynamics	7
1.6 Summary	9
1.7 References	9
Chapter 2: High spatial and temporal resolution remote sensing of a rapidly eroding segment of arctic coastline	15
2.1 Abstract	15
2.2 Introduction	16
2.3 Study area	19

2.4 Imagery and methodology	21
2.4.1 Imagery	21
2.4.2 Erosion rate measurements	23
2.4.3 Sea surface temperature data	24
2.4.4 Meteorological data	24
2.5 Results	25
2.5.1 Bluffline delineation from remotely sensed imagery	25
2.5.2 Annual and seasonal erosion	26
2.5.2 Environmental conditions.....	26
2.6 Discussion.....	27
2.6.1 Comparison to historical erosion rates at Drew Point	27
2.6.2 Comparison to annual erosion at other study sites	28
2.6.3 Seasonal erosion patterns at Drew Point and other sites	29
2.6.4 Annual and seasonal erosion relative to environmental conditions	29
2.7 Conclusion.....	33
2.8 Acknowledgements.....	34
2.9 References	34
2.10 Figures.....	39
2.11 Tables.....	45
Chapter 3: Modern thermokarst lake dynamics in the continuous permafrost zone, northern Seward Peninsula, Alaska.....	49
3.1 Abstract.....	49

3.2 Introduction	50
3.3 Study area	53
3.4 Methods.....	55
3.4.1 Imagery and classification	55
3.4.2 Lake shoreline change	58
3.4.3 Climate data analysis	59
3.5 Results and discussion.....	61
3.5.1 Lake and pond abundance and surface area	61
3.5.2 Thermokarst lake expansion rates	64
3.5.3 Thermokarst lake drainage	68
3.5.4 Climate data observations from 1950 to 2007.....	72
3.5.5 Thermokarst lake and carbon cycle dynamics.....	73
3.6 Conclusion.....	76
3.7 Acknowledgements.....	76
3.8 References	77
3.9 Figures	84
3.10 Tables.....	93
3.11 Supporting online material.....	94
Chapter 4: Identification of unrecognized tundra fire events on the North Slope of Alaska	95
4.1 Abstract.....	95
4.2 Introduction	96

4.3 Study area and methods	98
4.3.1 Landscape-scale aerial observations.....	98
4.3.2 Ground observations and surveys.....	99
4.3.3 Analysis of remotely sensed imagery	101
4.3.4 Field verification of unrecognized fire events.....	102
4.4 Results	102
4.4.1 Delineation of unrecognized tundra fires	102
4.4.2 Charred material and age control.....	103
4.4.3 Vegetative and geomorphic characteristics	104
4.5 Discussion.....	105
4.5.1 Spatial and temporal context of fire on the North Slope of Alaska.....	105
4.5.2 Wildland fires and shrub invasion of tundra	110
4.5.3 Fire history and permafrost degradation.....	111
4.6 Broader implications.....	114
4.7 Conclusions	115
4.8 Acknowledgements.....	115
4.9 References	116
4.10 Figures.....	121
4.11 Tables.....	128
4.12 Supporting online material.....	129
Chapter 5: Quantifying landscape change in an arctic coastal lowland using repeat airborne LiDAR	135

5.1 Abstract	135
5.2 Introduction	136
5.3 Study area	138
5.4 Methods	140
5.4.1 Airborne LiDAR data.....	140
5.4.2 Geomorphic classification of landscape change units.....	141
5.4.3 Air and permafrost temperature and active layer thickness measurements...	142
5.5 Results	143
5.6 Discussion	144
5.6.1 Airborne LiDAR change detection.....	144
5.6.2 Factors contributing to landscape change.....	146
5.6.3 Organic carbon mobilization.....	148
5.7 Conclusion	149
5.8 Acknowledgements	149
5.9 References	150
5.11 Figures	155
5.10 Tables	161
Chapter 6: Summary	163
6.1 Overview	163
6.2 Dissertation results	163
6.3 Future directions	166
6.4 References	167

List of Figures

		Page
Chapter 2		
Figure 1	Drew Point study coast along Beaufort Sea	39
Figure 2	Field photographs showing erosional processes	40
Figure 3	High-resolution satellite imagery	41
Figure 4	Decadal and annual erosion rates	42
Figure 5	Mean annual erosion rate from 2002 to 2012.....	43
Figure 6	Scatterplots of annual erosion vs. environmental conditions	44
Chapter 3		
Figure 1	Arctic and Sub-Arctic lake change detection studies	84
Figure 2	Cape Espenberg Lowlands study area.....	84
Figure 3	Number of water bodies in various size classes	86
Figure 4	Thermokarst lake expansion rate measurements.....	87
Figure 5	Field photographs showing difference in bluff types	88
Figure 6	Topographic profile adjacent to a recently drained lake.....	89
Figure 7	Image time series showing lake dynamics	90
Figure 8	Climate data parameters during the study period	91
Figure 9	Landscape-scale observations of lake dynamics.....	92

	Page
Chapter 4	
Figure 1	Fire distribution on the North Slope of Alaska.....121
Figure 2	Oblique photography of tundra fire sites122
Figure 3	High-resolution satellite imagery of tundra fire sites.....123
Figure 4	Enhanced Landsat imagery of Meade and Ketik sites124
Figure 5	Charred material preserved in soil column125
Figure 6	Differences in vegetation at burned and unburned sites.....126
Figure 7	Ground-based surveys at burned and unburned sites127
SOM Figure 1	Late-1940s aerial photography of fire sites129
SOM Figure 2	Likely tundra fire site near the Chandler River130
Chapter 5	
Figure 1	Repeat airborne LiDAR study area155
Figure 2	Oblique photos of features in the study region156
Figure 3	Example showing agreement between the two datasets.....157
Figure 4	Examples of permafrost degradation features.....158
Figure 5	Air temperature and thawing degree day sums.....159
Figure 6	Permafrost temperature and active layer data160

List of Tables

	Page
Chapter 2	
Table 1 Satellite imagery information.....	45
Table 2 Erosion rate error estimates and mean erosion	46
Table 3 Mean annual erosion and environmental conditions.....	47
Table 4 Mean seasonal erosion and environmental conditions	48
Chapter 3	
Table 1 Thermokarst lake change numbers.....	93
Table 2 A synthesis of thermokarst lake expansion rates	93
SOM Table 1 Imagery information.....	94
Chapter 4	
Table 1 Age control for Meade and Ketik fire sites.....	128
SOM Table 1 Raw data table compiled from vegetation surveys	131
Chapter 5	
Table 1 Classified landscape change objects	161

Preface

This dissertation consists of six chapters. Chapter 1 serves as the introduction and provides background information on climatic changes occurring in the Arctic and the response of the landscape. Chapters 2, 3, 4, and 5 detail the studies that I led during my dissertation degree and are written and included in manuscript format. Chapter 2 has been formatted for a Cryospheric Remote Sensing special issue in the journal *Remote Sensing* and it is currently in review. Chapter 3 was published in the *Journal of Geophysical Research Biogeosciences* in 2011 and Chapter 4 was published in *Journal of Geophysical Research Biogeosciences* in 2013. Chapter 5 is *in press* in *Environmental Research Letters*.

I am the primary contributor and senior author for all of the material included in the body of this dissertation. I developed the study design and led the remote sensing analysis for all remote sensing components associated with each of the studies. I took the lead role in drafting each of the manuscripts and identifying colleagues with expertise and knowledge of a particular field that contributed greatly to the outcome of each study. Since my interests and this dissertation are in fulfillment of a degree in Interdisciplinary Studies, each chapter benefitted from the contribution of scientists with diverse expertise. Chapter 2 benefited from the contributions to data compilation, interpretation, and analysis provided by Guido Grosse, Christopher Arp, and Jinlun Zhang. Chapter 3 was strengthened by analysis of climate data by Christopher Arp, interpretation of modern thermokarst lake and permafrost dynamics by Guido Grosse and Vladimir Romanovsky, and the broader carbon cycle implications associated with the observed patterns of

landscape change by Miriam Jones and Katey Walter Anthony. Chapter 4 represented a broad collaborative effort that combined field surveys with remotely sensed image analysis. Amy Breen, Ben Gaglioti, Dan Mann, Guido Grosse, Christopher Arp, and Mike Kunz assisted with fieldwork, data analysis, and manuscript writing. Adrian Rocha and Skip Walker assisted with manuscript writing and vegetation and fire history discussions. For Chapter 5, Jason Stoker, Ann Gibbs, Guido Grosse, Nicole Kinsman, and Bruce Richmond helped with data acquisition, data processing, and manuscript writing. Vladimir Romanovsky and Tom Douglas helped with interpretation of results and manuscript writing.

Funding for this research was partially provided by NASA grant NNX08AJ37G, NSF IPY grant 0732735, and the U.S. Geological Survey Alaska Science Center and Alaska Regional Directors Office. Additional support for my dissertation studies were provided by the Bureau of Land Management Arctic Field Office, the Arctic Landscape Conservation Cooperative, and the National Park Service. Paul Morin and Tom Cecere were instrumental in the acquisition of recent high-resolution satellite imagery used in Chapter 2. Chapter 5 benefited from the efforts of the U.S. Geological Survey National Shoreline Change Assessment program that was responsible for the acquisition of the 2010 LiDAR data.

I would like to thank my advisor Dr. Guido Grosse for taking me on as a PhD student. I would like to thank my other committee members Drs. Christopher Arp, Daniel Mann, Vladimir Romanovsky, and David Verbyla for serving on my committee and providing guidance. I also thank Dr. Katey Walter Anthony for her early

contributions to my committee. I am indebted to all of my coauthors that contributed to each of my dissertation chapters. I would also like to thank Carl Markon, Marti Miller, Tony Degange, and Mark Shasby of the U.S. Geological Survey for allowing me to pursue a PhD while maintaining my primary affiliation and work duties. I would like to thank Wendy Eisner, Kenneth Hinkel, Kim Peterson, Jim Bockheim, and Richard Beck for introducing me to the Arctic. I would like to thank my family for continued support throughout my college education experience and my wife and hounds for dealing with my overcommitted lifestyle these past five years.

Chapter 1: Introduction

1.1 Research topic background and dissertation overview

Surface air temperatures in the Arctic have warmed by $\sim 0.35^{\circ}\text{C}$ per decade between 1970 and 2000, which is two times faster than the average global rate of warming [Serreze and Francis, 2006]. The reasoning behind the so called Arctic Amplification is still a matter of debate, but one of the primary drivers is thought to be the positive feedback associated with the sea ice – climate system [Serreze et al., 2009; Screen and Simmonds, 2010]. In Alaska, the continual decline in sea ice extent in the Beaufort and Chukchi Seas is thought to be driving the continued warming in the Arctic region, while the remainder of the state has entered a cooling trend [Wendler et al., 2012]. The ongoing changes occurring in the coupled Arctic system appear to be driving a host of responses in terrestrial, aquatic, and marine ecosystems and landscapes [Hinzman et al., 2005; Richter-Menge et al., 2010; AMAP, 2011]. In particular, changes to the ground thermal regime and the rate of disturbance in the Arctic may have powerful impacts on landscape dynamics [Rowland et al., 2010] and carbon cycling [Grosse et al., 2011].

Permafrost has warmed throughout much of the Northern Hemisphere since the 1980s, with colder permafrost sites warming more rapidly than warmer permafrost sites [Romanovsky et al., 2010; Smith et al., 2010; Heginbottom et al., 2012]. Warming of the near surface permafrost may lead to widespread terrain instability in ice-rich permafrost deposits in the Arctic and result in thermokarst development and other thaw-related landscape features [Jorgenson et al., 2006; Gooseff et al., 2009]. The term thermokarst originated in the Russian literature and its scientific use has varied substantially over time

[Shur and Osterkamp, 2007]. The modern definition of thermokarst refers to the process by which characteristic landforms result from the thawing of ice-rich permafrost or the melting of massive ice [van Everdingen, 1998]; or more specifically, thaw of ice-rich permafrost and/or melting of massive ice that result in consolidation and deformation of the soil surface and formation of specific forms of relief [Shur, 1988]. Jorgenson [2013] identifies 23 distinct thermokarst and other thaw-related features in the Arctic, Sub-Arctic, and Antarctic based primarily on differences in terrain condition, ground-ice volume, and heat and mass transfer processes. An increase in active layer depth, water accumulation on the soil surface, permafrost degradation and retreat of the permafrost table, and changes to lake and coastal erosion act and interact to create thermokarst features on the landscape [Shur and Osterkamp, 2007]. There is increasing interest in the spatial and temporal dynamics of thermokarst and other thaw-related features from a wide diversity of disciplines including: landscape ecology, hydrology, engineering, and biogeochemistry.

Remote sensing provides an excellent tool for observing, documenting, and better understanding landscape change in the Arctic from local, to regional, to Pan-Arctic scales. In particular, it has emerged as one of the primary tools for advancing the field of thermokarst research [Kokelj and Jorgenson, 2013] and more than half of the references identified in Jones et al. [2013] used remote sensing to some degree in their studies of thermokarst and thaw-related landscape features. Further, Rowland et al. [2010] noted that with the scale of questions and facets of landscape change in the Arctic that “a

particular focus must be placed on identifying existing and developing new remote sensing technologies to detect near-surface and subsurface changes in the Arctic”.

My dissertation focuses on the application of various remote sensing image sources and techniques for the quantification and detection of Arctic landscape dynamics over various time scales. In particular, I focused on permafrost coastline erosion, thermokarst lake dynamics, fire-related arctic landscape change and disturbance, and the quantification of surface deformation using repeat airborne LiDAR data. The dissertation is divided into six chapters, with Chapter 1 being this introduction and Chapter 6 providing a summary of the research results. Chapter 2 focuses on the use of high-spatial resolution satellite imagery acquired at high-temporal resolution coupled with an analysis of varying environmental conditions over the study period for the same segment of permafrost coastline located on the Alaska Beaufort Sea. Chapter 3 examines the dynamics associated with thermokarst lakes on the northern portion of the Seward Peninsula using aerial photography and high-resolution satellite imagery acquired in the early 1950s, late 1970s, and mid-2000s. Chapter 4 demonstrates the utility of combining field surveys with various remotely sensed image sources in the identification of previously unrecognized tundra fire disturbances that occurred on the North Slope of Alaska prior to the period of record keeping and highlights the need for combining information from various remotely sensed image sources to extend records beyond just those events that happened during the remote sensing period. Chapter 5 assesses the ability to detect surface elevation changes in an arctic coastal lowland on the Beaufort Sea Coastal Plain using repeat airborne Light Detection and Ranging (LiDAR) data.

1.2 Rapid erosion of a permafrost coastline

Permafrost influences 30 to 34% of the coastlines on Earth and these primarily occur in the Arctic [Walker, 2005; Lantuit et al., 2012]. Arctic climate change will likely increase the vulnerability of these coasts and cause significant changes in coastal morphologies, ecosystems, and subsistence lifestyles. These changes include reductions in sea ice extent [Stroeve et al., 2012], rising air [ACIA, 2005] and sea surface [Steele et al., 2008] temperatures, sea-level rise [Richter-Menge et al., 2010], warming permafrost [Romanovsky et al., 2010; Smith et al., 2010], and increased storminess [Simmonds and Rudeva, 2012] and storm surges [Vermaire et al., 2013]. However, several observation sites in the Arctic have yet to link decadal-scale erosion rates with changing environmental conditions, which likely results in part from the broad temporal gaps in suitable remote sensing data to address the relative role of potential drivers of change.

In this chapter, I utilized the ability to task high-spatial resolution satellite imagery. Ten images were acquired for a rapidly eroding segment of the Beaufort Sea Coast in Alaska in order to derive bluffline positions on an annual to seasonal basis between 2008 and 2013. This analysis was combined with local meteorological data over the period of interest as well as open water duration and sea surface temperature derived in part from remotely sensed observations. This effort more than doubled the number of suitable high-spatial resolution satellite images acquired for this study site since the 1950s and when combined with an analysis of environmental conditions thought to be responsible for the rate at which permafrost coasts erode provide some interesting insights. The detailed observations made possible by the availability of high-spatial

resolution satellite imagery provide a necessary step forward when attempting to link changes occurring in the Arctic and the response of the coastline and will help improve monitoring and modeling efforts and assessments of coastal vulnerability.

1.3 Modern thermokarst lake dynamics in the continuous permafrost zone

Thermokarst lakes mainly formed during the Holocene and are a sign of local permafrost degradation following post glacial climate warming [Rampton, 1988; Romanovskii et al., 2004; Walter et al., 2007]. Thermokarst lakes are abundant surface features across many high latitude regions, such as the Seward Peninsula [Hopkins, 1949; West and Plug, 2008; Plug and West, 2009], the Arctic Coastal Plain [Sellmann et al., 1975; Hinkel et al., 2005] as well as several areas in Interior Alaska [Jorgenson and Osterkamp, 2005]; in Canada on Banks Island [Harry and French, 1983], Tuktoyaktuk Peninsula [Mackay, 1988], the Yukon Coastal Plain [West and Plug, 2008; Plug and West, 2009], and Richards Island [Burn, 2002], and in large regions of Siberia [Romanovskii et al., 2004, Tomirdiaro and Ryabchun, 1973; Zimov et al., 1997; Smith et al., 2005; Grosse et al., 2006; Walter et al., 2007; Grosse et al., 2013]. Their importance to global climate change and northern high latitude soil and permafrost-stored carbon cycling has been noted [Zimov et al., 1997; Walter et al., 2006; Walter et al., 2007]. Therefore quantifying changes in thermokarst lakes is important for understanding potential positive and negative feedbacks to the atmospheric carbon budget. A suite of recent studies have utilized remotely sensed imagery to document changes in thermokarst lake extent in various locations across the Arctic and Subarctic (e.g. Yoshikawa and Hinzman, 2003; Smith et al., 2005, Riordan et al., 2006). In general, thermokarst lakes

are thought to be increasing in abundance and surface area in regions of continuous permafrost and decreasing in abundance and surface area in transitional permafrost zones (discontinuous, isolated, sporadic) [Smith et al., 2005].

In this chapter, I conducted a thermokarst lake change detection study using historical aerial photography and more recent high-resolution satellite imagery for a 700 km² study area on the northern Seward Peninsula of northwestern Alaska. I was interested in testing how this continuous permafrost site compared to observations elsewhere in the Arctic and whether thermokarst lake formation and expansion rates could account for such dramatic increases in the lake area thus far reported [Smith et al., 2005]. I assessed the general patterns of change in surface area across the study area as well as the expansion rate and drainage rate of thermokarst lakes. I also summarized the available literature on thermokarst lake expansion rates from other studies in the Arctic and Subarctic. A short discussion at the end of the chapter highlights the complexities associated with thermokarst lakes on the northern high latitude carbon budget.

1.4 Unrecognized tundra fire events on the North Slope of Alaska

Fire influences vegetation distribution and structure, carbon cycling, land-atmosphere energy exchange, and climate, and it represents an important and widespread disturbance mechanism in several major biomes [Bowman et al., 2009]. However, the role of fire in shaping ecosystem patterns in arctic tundra remains poorly resolved due to the rarity of reported fires, the geographic remoteness of the region, and the short observational record in the region [Barney and Comiskey, 1973; Wein, 1976; Giglio et al., 2006; Rocha et al., 2012]. As a result, an accurate representation of the Arctic in models depicting the

geographic distribution of wildfires and potential shifts in global wildfire activity and pyrogenic gas emissions is lacking [Bond et al., 2005; Krawchuk et al., 2009; van der Werf et al., 2010]. Given ongoing climate change in the Arctic [ACIA, 2005; AMAP, 2011], the frequency, severity, and areal extent of tundra fires is predicted to increase [Higuera et al., 2008; Hu et al., 2010]. Thus, a better understanding of the role of fires in the tundra biome is needed since tundra vegetation, peat, and frozen soils in the Arctic store large, globally significant amounts of labile carbon [McGuire et al., 2009; Tarnocai et al., 2009], and pulse disturbances like fire, can play an important role in releasing this carbon [Grosse et al., 2011; Mack et al., 2011].

In this study, I developed diagnostic landscape characteristics of past known tundra fire disturbances on the North Slope of Alaska by combining field surveys with remotely sensed imagery. This information was then used to extend the fire history beyond those events that have occurred since the start of the remote sensing period. Various remotely sensed image sources were used to scale-up the field observations to delineate an estimated perimeter for the tundra fire events. Identification of these sites also provides a centennial-scale chronosequence of post-fire vegetation and geomorphic change providing a valuable temporal context for better understanding the impacts of tundra fires during a period in which they are expected to increase in their number, size, and frequency.

1.5 Repeat airborne LiDAR for arctic landscape dynamics

Terrestrial, aquatic, and marine environmental changes occurring in the Arctic may be interacting to increase erosion of coastal lowland landscapes [Jorgenson et al.,

2006; Overeem et al., 2011; Romanovsky et al., 2010; Smith et al., 2010; Stroeve et al., 2012]. Thus far, most remote sensing studies focused on identifying landscape change of near surface permafrost terrain in arctic lowland regions primarily rely on 2-dimensional measurements to quantify lateral rates of change for thermokarst lakes [Arp et al., 2011; Jones et al., 2011], thermokarst lake drainage [Hinkel et al., 2007; Marsh et al., 2009], retrogressive thaw slump headwall retreat [Lantz and Kokelj, 2008], thermo-erosional gully formation and expansion [Fortier et al., 2007], erosion of coasts by block collapse and mass wasting [Jones et al., 2009], and degradation of ice wedges and thermokarst pit formation [Jorgenson et al., 2006].

In this study, I tested the ability of utilizing repeat airborne Light Detection and Ranging (LiDAR) data for quantifying vertical surface deformation in a 100 km² study located on the Arctic Coastal Plain along the Beaufort Sea coast. Using a conservative measure of change between two data collection efforts separated by four years, I was able to detect erosional features indicative of ice-rich permafrost degradation were associated with ice-bonded coastal, river, and lake bluffs, frost mounds, ice-wedges, and thermo-erosional gullies as well as erosional and depositional features associated with coastal and riverine processes. The results from this study provide stimulus for going forward with repeat airborne LiDAR data acquisitions in other permafrost terrain at sub-decadal time-scales.

1.6 Summary

This concluding chapter reviews the four studies that compose my dissertation and how this work will feed into ongoing efforts interested in quantifying landscape change in the Arctic.

1.7 References

ACIA (2005), *Impacts of a warming arctic: arctic climate impact assessment*, Cambridge University Press, Cambridge, UK.

AMAP (2011), *Snow, Water, Ice and Permafrost in the Arctic (SWIPA): Climate Change and the Cryosphere*, Arctic Monitoring and Assessment Programme (AMAP), Oslo, Norway. 538 pp.

Arp, C.D., B.M. Jones, F.E. Urban, and G. Grosse (2011), Hydrogeomorphic processes of thermokarst lakes with grounded-ice and floating-ice regimes on the Arctic coastal plain, Alaska, USA, *Hydrological Processes*, 25, 2422-2438.

Barney, R. J., and A.L. Comiskey (1973), Wildfires and thunderstorms on Alaska's North Slopes, USDA Forest Service Pacific Northwest Forest and Range Experiment Station, Portland, OR Research Note PNW-311.

Bond, W. J. et al., (2005), The global distribution of ecosystems in a world without fire, *New Phytologist*, 165, 525-538.

Bowman, D. M. J. S. et al. (2009), Fire in the Earth System, *Science*, 324, 481-484.

Burn, C.R. (2002), Tundra lakes and permafrost, Richards Island, western Arctic coast, Canada, *Canadian Journal of Earth Sciences*, 39, 1281-1298.

Fortier D., M. Allard, and Y. Shur (2007), Observation of rapid drainage system development by thermal erosion of ice wedges on Bylot Island, Canadian Arctic Archipelago, *Permafrost and Periglacial Processes*, 18, 229-243.

Giglio, L., I. Csiszar, and C. O. Justice (2006), Global distribution and seasonality of active fires as observed with the Terra and Aqua Moderate Resolution Imaging Spectroradiometer (MODIS) sensors, *J. Geophys. Res.*, 111, G02016 doi:10.1029/2005JG000142.

Gooseff, M. N., A. Balsler, W. B. Bowden, and J. B. Jones (2009), Effects of hillslope thermokarst in northern Alaska, *Eos, Transactions American Geophysical Union*, 90(4), 29-36.

Grosse, G., L. Schirrmeister, and T.J. Malthus (2006), Application of Landsat-7 satellite data and a DEM for the quantification of thermokarst-affected terrain types in the periglacial Lena-Anabar coastal lowland, *Polar Research*, 25, 51-67.

Grosse, G., et al. (2011), Vulnerability of high-latitude soil organic carbon in North America to disturbance, *Journal of Geophysical Research*, 116(G4), G00K06.

Grosse, G., B. M. Jones, and C. D. Arp (2013), Thermokarst lakes, drainage, and drained basins, In: Editor-in-Chief: John F. Shroder, *Treatise on Geomorphology*, Academic Press, San Diego, 325-353, ISBN 9780080885223, doi: 10.1016/B978-0-12-374739-6.00216-5.

Harry, D. G., and H. M. French (1983), The orientation and evolution of thaw lakes, southwest Banks Island, Canadian Arctic, in *Fourth International Conference on Permafrost*, edited by T. L. Pewe and J. Brown, pp. 456–461, Natl. Acad. Press, Fairbanks, Alaska.

Heginbottom J. A., J. Brown, O. Humlum, and H. Svensson (2012), Permafrost and periglacial environments. In *State of the Earth's Cryosphere at the Beginning of the 21st Century: Glaciers, Global Snow Cover, Floating Ice, and Permafrost and Periglacial Environments*, Williams RS Jr, Ferrigno JG (eds). *US Geological Survey Professional Paper 1386-A*, 546 p.

Higuera, P. E., L. B. Brubaker, P. M. Anderson, T. A. Brown, A. T. Kennedy, and F. S. Hu (2008), Frequent fires in ancient shrub tundra: implications of paleorecords for arctic environmental change, *PLoS ONE*, 3, e0001744 doi: 10.1371/journal.pone.0001744.

Hinkel, K.M., R.C. Frohn, F.E. Nelson, W.R. Eisner, and R.A. Beck (2005), Morphometric and Spatial Analysis of Thaw Lakes and Drained Thaw Lake Basins in the Western Arctic Coastal Plain, Alaska, *Permafrost & Periglacial Processes*, 16, 327-341.

Hinkel, K. M., B. M. Jones, W. R. Eisner, C. J. Cuomo, R. A. Beck, and R. C. Frohn (2007), Methods to assess natural and anthropogenic thaw lake drainage on the western Arctic Coastal Plain of northern Alaska, *J. Geophys. Res.*, 112, F02S16, doi:10.1029/2006JF000584.

Hinzman L. D. et al. (2005), Evidence and implications of recent climate change in northern Alaska and other arctic regions, *Climatic Change*, 72, 251-298.

Hopkins, D. M. (1949), Thaw lakes and thaw sinks in the Imuruk Lake area, Seward Peninsula, Alaska, *Journal of Geology*, 57, 119-131.

Hu, F. S., P. E. Higuera, J. E. Walsh, W. L. Chapman, P. A. Duffy, L. B. Brubaker, and M. L. Chipman (2010), Tundra burning in Alaska: linkages to climatic change and sea-ice retreat, *J. of Geophys. Res.*, *115*, G04002 doi:10.1028/2009JG001270.

Jones, B. M., C. D. Arp, M. T. Jorgenson, K. M. Hinkel, J. A. Schmutz, and P. L. Flint (2009), Increase in the rate and uniformity of coastline erosion in Arctic Alaska, *Geophys. Res. Lett.*, *36*, L03503, doi:10.1029/2008GL036205.

Jones B. M., G. Grosse, C. D. Arp, M. C. Jones, K. M. W. Anthony, and V. E. Romanovsky (2011), Modern thermokarst lake dynamics in the continuous permafrost zone, northern Seward Peninsula, Alaska, *Journal of Geophysical Research*, *116*, G00M03.

Jones, B. M., C. L. Amundson, J. C. Koch, and G. Grosse (2013), Thermokarst and thaw-related landscape dynamics—An annotated bibliography with an emphasis on potential effects on habitat and wildlife, *U.S. Geological Survey Open-File Report 2013-1161*, 60 p., <http://pubs.usgs.gov/of/2013/1161>.

Jorgenson, M. T. (2013), Thermokarst Terrains. In: Editor-in-Chief: John F. Shroder, Editor(s)-in-Chief, *Treatise on Geomorphology*, Academic Press, San Diego, pp. 313-324.

Jorgenson, M. T., and T. Osterkamp (2005), Response of boreal ecosystems to varying modes of permafrost degradation, *Canadian Journal of Forestry Research*, *35*, 2100-2111.

Jorgenson, M. T., Y. L. Shur, and E. R. Pullman (2006), Abrupt increase in permafrost degradation in Arctic Alaska, *Geophys. Res. Lett.*, *33*, L02503, doi:10.1029/2005GL024960.

Kokelj, S. V., and M. T. Jorgenson (2013), Advances in Thermokarst Research, *Permafrost and Periglacial Processes*, *24*(2), 108-119.

Krawchuk, M. A., M. A. Moritz, M-A. Parisien, J. Van Dorn, and K. Hayhoe (2009), Global Pyrogeography: the Current and Future Distribution of Wildfire, *PLoS ONE*, *4*, e5102 doi:10.1371/journal.pone.0005102.

Lantuit, H., V. Rachold, W. H. Pollard, F. Steenhuisen, R. Ødegård, and H. W. Hubberten (2009), Towards a calculation of organic carbon release from erosion of Arctic coasts using non-fractal coastline datasets, *Marine Geology*, *257*, 1-10.

Lantuit, H. et al. (2012), The Arctic Coastal Dynamics database: A new classification scheme and statistics on Arctic permafrost coastlines, *Estuaries and coasts*, *35*, 383-400.

Lantz, T. C., and S. V. Kokelj (2008), Increasing rates of retrogressive thaw slump activity in the Mackenzie Delta region, N.W.T., Canada, *Geophys. Res. Lett.*, *35*, L06502, doi:10.1029/2007GL032433.

Mack, M. C., M. S. Bret-Harte, T. N. Hollingsworth, R. R. Jandt, E. A. G. Schuur, G. R. Shaver, and D. L. Verbyla (2011), Carbon loss from an unprecedented Arctic tundra wildfire, *Nature*, *475*, 489-492 doi:10.1038/nature10283.

Mackay, J.R. (1988), Catastrophic lake drainage, Tuktoyaktuk Peninsula area, District of Mackenzie, *Current Research, Part D, Geological Survey of Canada, Paper 88-1D*, 83-90.

Marsh, P., M. Russell, S. Pohl, H. Haywood, and C. Onclin (2009), Changes in thaw lake drainage in the western Canadian Arctic from 1950 to 2000, *Hydrol. Processes*, *23*, 145–158, doi:10.1002/hyp.7179.

McGuire, A. D. et al. (2009), Sensitivity of the carbon cycle in the Arctic to climate change, *Ecol. Monogr.*, *79*, 523–555 doi:10.1890/08-2025.1.

Overeem I., R. S. Anderson, C. W. Wobus, G. D. Clow, F. E. Urban, and N. Matell (2011), Sea ice loss enhances wave action at the Arctic coast, *Geophysical Research Letters*, *38*, L17503.

Plug, L.J. and J.J. West (2009), Thaw lake expansion in a two-dimensional coupled model of heat transfer, thaw subsidence, and mass movement, *Journal of Geophysical Research*, *114*, F01002.

Rampton, V.M. (1988), Quaternary Geology of the Tuktoyaktuk Coastlands, Northwest Territories, *Geological Survey of Canada memoir*, *423*, 98 pp.

Richter-Menge, J., et al. (2010), Arctic Report Card 2010, NOAA, Silver Spring, Md. (Available at <http://www.arctic.noaa.gov/reportcard>).

Riordan, B., D. Verbyla, and A.D. McGuire (2006), Shrinking ponds in subarctic Alaska based on 1950–2002 remotely sensed images, *Journal of Geophysical Research*, *111*, G04002.

Rocha, A. V. et al. (2012), The footprint of Alaskan tundra fires during the past half-century: implications for surface properties and radiative forcing, *Env. Res. Lett.*, *7*, 044039 doi:10.1088/1748-9326/7/4/044039.

Rowland, J. C., et al. (2010), Arctic landscapes in transition: Responses to thawing permafrost, *Eos, Transactions American Geophysical Union*, *91(26)*, 229-230.

Romanovskii, N. N., H.-W. Hubberten, A.V. Gavrilov, V.E. Tumskoy, and A. Kholodov (2004), Permafrost of the east Siberian Arctic shelf and coastal lowlands, *Quaternary Science Reviews*, 23, 1359-1369.

Romanovsky, V. E., S. L. Smith, and H. H. Christiansen (2010), Permafrost thermal state in the polar Northern Hemisphere during the international polar year 2007–2009: A synthesis, *Permafrost and Periglacial Processes*, 21, 106-116.

Screen, J. A., and I. Simmonds (2010), The central role of diminishing sea ice in recent Arctic temperature amplification, *Nature*, 464(7293), 1334-1337.

Sellmann, P.V., J. Brown, R.I. Lewellen, H.L. McKim, and C.J. Merry (1975), The classification and geomorphic implications of thaw lakes on the Arctic Coastal Plain, Alaska, U.S. Army Cold Regions Research and Engineering Laboratory, Hanover, New Hampshire, 21 pp.

Serreze, M. C., and J. A. Francis (2006), The Arctic amplification debate, *Climatic Change*, 76, 241-264.

Serreze, M. C., A. P. Barrett, J. C. Stroeve, D. N. Kindig, and M. M. Holland (2009), The emergence of surface-based Arctic amplification, *Cryosphere*, 3, 11–19.

Shur, Y.L., (1988), The upper horizon of permafrost and thermokarst, Novosibirsk "Nauka". 210 p.

Shur, Y.L., and T. E. Osterkamp (2007), Thermokarst, *Institute of Northern Engineering, University of Alaska Fairbanks, Fairbanks, AK, Rep. INE06.11*, 50 pp.

Simmonds, I., and I. Rudeva (2012), The great Arctic cyclone of August 2012, *Geophys. Res. Lett.*, 39, L23709, doi:10.1029/2012GL054259.

Smith, L.C., Y. Sheng, G.M. MacDonald, and L.D. Hinzman (2005), Disappearing Arctic Lakes, *Science*, 308, 1429.

Smith, S. L., et al. (2010), Thermal state of permafrost in North America: A contribution to the International Polar Year, *Permafrost and Periglacial Processes*, 21, 117-135.

Steele, M., W. Ermold, and J. Zhang (2008), Arctic Ocean surface warming trends over the past 100 years, *Geophysical Research Letters*, 35(2), L02614.

Stroeve J. C., M. C. Serreze, M. M. Holland, J. E. Kay, J. Malanik, and A. P. Barrett (2012), The Arctic's rapidly shrinking sea ice cover: a research synthesis, *Climatic Change*, 110, 1005-1027.

Tarnocai C., J. G. Canadell, E. A. G. Schuur, P. Kuhry, G. Mazhitova, and S. Zimov (2009), Soil organic carbon pools in the northern circumpolar permafrost region, *Global Biogeochem. Cycles*, 23, GB2023 doi:10.1029/2008GB003327.

Tomirdiaro, S.V., and V.K. Ryabchun (1973), Lake thermokarst on the Lower Anadyr Lowland. In: Permafrost: USSR Contribution to the Second International Conference, Yaktusk, USSR. Washington, DC, National Academy of Science, pp. 94-100.

van der Werf, G. R. et al. (2010), Global fire emissions and the contribution of deforestation, savanna, forest, agricultural, and peat fires (1997–2009), *Atmos. Chem. Phys.*, 10, 11707-11735 doi:10.5194/acp-10-11707-2010, 2010.

van Everdingen, Robert, ed. 1998 revised May 2005. Multi-language glossary of permafrost and related ground-ice terms,. Boulder, CO: National Snow and Ice Data Center.

Vermaire, J. C., M. F. J. Pisaric, J. R. Thienpont, C. J. Courtney Mustaphi, S. V. Kokelj, and J. P. Smol (2013), Arctic climate warming and sea ice declines lead to increased storm surge activity, *Geophys. Res. Lett.*, 40, 1386–1390, doi:10.1002/grl.50191.

Walker H. J. (2005), Arctic coastal geomorphology, In Encyclopedia of Coastal Science, Schwartz ML (ed). Springer: 49–50.

Walter, K. M., S.A. Zimov, J.P. Chanton, D. Verbyla, and F.S. Chapin, III (2006), Methane bubbling from Siberian thaw lakes as a positive feedback to climate warming, *Nature*, 443, 71–75.

Walter, K. M., M. E. Edwards, G. Grosse, S. A. Zimov, and F. S. Chapin III (2007), Thermokarst lakes as a source of atmospheric CH₄ during the last deglaciation, *Science*, 318, 633–636, doi:10.1126/science.1142924.

Wein, R. W. (1976), Frequency and characteristics of Arctic tundra fires, *Arctic*, 29, 213–222.

West, J. J., and L. J. Plug (2008), Time-dependent morphology of thaw lakes and taliks in deep and shallow ground ice, *Journal of Geophysical Research*, 113, F01009.

Yoshikawa, K. and L.D. Hinzman (2003), Shrinking thermokarst ponds and groundwater dynamics in discontinuous permafrost near Council, Alaska, *Permafrost & Periglacial Processes*, 14, 151-160.

Zimov, S.A., Y.V. Voropaev, I.P. Semiletov, S.P. Davidov, S.F. Prosiannikov, F.S. Chapin III, M.C. Chapin, S. Trumbore, and S. Tyler (1997), North Siberian Lakes: A Methane Source Fueled by Pleistocene Carbon, *Science*, 277, 800-802.

Chapter 2: High spatial and temporal resolution remote sensing of a rapidly eroding segment of arctic coastline¹

2.1 Abstract

Eroding permafrost coasts in the Arctic are increasingly susceptible to the combined effects of declining sea ice extent, more frequent and effective storms, sea level rise, and warming permafrost. However, several observation sites in the Arctic have yet to firmly link decadal-scale erosion rates with changing environmental conditions. This partially results from the broad temporal gaps in suitable remote sensing observations necessary to address the relative role of potential drivers of change. Here we used high spatial resolution optical satellite imagery acquired at high temporal resolution between 2008 and 2013 to better understand recent patterns of erosion for a 9 km segment of permafrost coastline at Drew Point, Beaufort Sea Coast, Alaska. Mean annual erosion rates for the open water periods between 2008 and 2012 were 16.3 m/yr and in line with heightened erosion documented here between 2002 and 2007. Mean annual erosion ranged from 6.7 m in 2010 to 22.5 m in 2012, with 2008, 2009, and 2011 eroding between 16 and 19 m. The strong correlation of annual erosion rate with the modeled number of open water days ($R^2=0.77$) and the number of storms ($R^2=0.84$) over this five year period highlight the linkage of declining sea ice with accelerating retreat of the coastline at this site. In 2008 and 2011, ~70% of the annual erosion occurred in the early portion of the open-water season. This study shows how detailed observations of arctic coasts, now possible

¹ Jones.B. M., G. Grosse, C. D. Arp, and J. Zhang (*In Review*), High spatial and temporal resolution remote sensing of a rapidly eroding segment of arctic coastline, *Remote Sensing*.

using high-spatial resolution satellite imagery, provide an essential step forward in linking changes at the Arctic land-sea interface with those in the broader Arctic system.

2.2 Introduction

Permafrost influences 30 to 34 % of the coastlines on Earth, most of which occur in the Arctic [1,2]. Arctic climate change will likely increase the vulnerability of these coasts to erosion and drive significant changes to coastal morphologies, ecosystems, and human subsistence lifestyles. These changes include reductions in sea ice extent [3], rising air [4] and sea surface [5] temperatures, sea-level rise [6], warming permafrost [7,8], and increased storminess [9] and storm surges [10].

Despite the prevalence of permafrost coasts in the northern hemisphere and their apparent vulnerability to change, there remains a paucity of information regarding their recent dynamics. Lantuit et al. [11] identified only 15 coastal change detection studies conducted between 2008 and 2012 accounting for less than 1% of the Arctic permafrost coastline, with only one study reporting a time series of annual retreat rates [12]. The *State of the Arctic Coast 2010* [13] highlights the primary limiting issue related to a better understanding of arctic coastal dynamics is the lack of an Arctic-wide distribution of coastal observatories or locations of site-specific studies. These deficiencies largely result from the remoteness associated with permafrost coasts and the lack of archived remotely sensed data for such analyses. The majority of the studies (9 of 15) outlined in Lantuit et al. [11] have focused on coastline change in Alaska, while eight of these have focused specifically on the Beaufort Sea coast.

The Alaskan Beaufort Sea Coast (ABSC) is composed of a low-lying (maximum elevation of ~10 m) tundra plain that extends for ~1,950 km from the Canadian Border to Barrow, Alaska, USA. Unconsolidated permafrost sediments in bluffs along the coast tend to be bonded by ground ice and have a very high average total volumetric ice content of 77% [14]. Spatial and temporal rates of coastal change along the ABSC are known to be highly variable [2,15,16]. This is due to variability in ground-ice content as well as variation in erosional processes, geomorphology, lithology, coastal orientation, near shore bathymetry, and the presence of barrier islands [15]. Jorgenson and Brown [15] and Gibbs et al. [16] report that the long-term average erosion rate along the ABSC between the late-1940s and early-2000s was 2 m/yr. However some individual locations eroded as much as 16 m/yr, and homogenous segments as much as 9 m/yr. Ping et al. [17] assessed 48, 1km segments distributed across the ABSC and found that erosion from 1950 to 1980 was 0.6 m/yr and that it had increased to 1.2 m/yr for the period 1980 to 2000. Mars and Houseknecht [18] compared land loss due to erosion by differencing Landsat satellite imagery with legacy topographic map sheets and found a doubling in the rate of erosion between 1985 and 2005 relative to 1955 and 1985. Jones et al. [19] used more accurate techniques based on aerial photography for the exposed and north-facing, 60 km segment of the ABSC between Cape Halkett and Drew Point and found that the erosion rate increased from 6.7 m/yr (1955 to 1979), to 9.7 m/yr (1979 to 2002), to 13.6 m/yr (2002 to 2007). These last two studies encompass the 9 km Drew Point segment of coastline reported here in this paper.

Since most coastal change detection studies report rates averaged over years to decades, it is difficult to determine the relations between changes in environmental forcing and the response of the coast. Lantuit et al. [20] assessed the change in mean annual erosion rates for the Bykovsky Peninsula in Siberia and found no connection with the storm climatology for the region over the 55 year study period. Overeem et al. [21] indicated that the duration of open water conditions could be a good first order predictor of coastal erosion based on similar increases in open water duration and measured erosion rates at Drew Point between 1979-2002 and 2002-2007 as extracted from Jones et al. [19]. However, with observations of erosion on the order of 25-40 m during single storm events along some arctic coastal segments [2,22] the heightened erosion rates reported by Jones et al. [19] could have been a result of one or two large storm events averaged over a short time period. Thus, it is uncertain if the enhanced erosion at Drew Point was a result of a few catastrophic events or whether this pattern of erosion was linked to the atmospheric, terrestrial, and oceanic conditions persisting in the Arctic coastal zone during this period of rapid sea ice retreat [3].

In this study, we combined the use of high-spatial resolution (sub-meter) satellite imagery derived from optical (Quickbird, IKONOS, GEOEYE, Worldview-1 and -2) sensors to document annual as well as seasonal erosion between 2008 and 2012 along a 9 km segment of ABSC coast located near Drew Point. By combining multi-source imagery we acquired 10 scenes over this five-year period. This effort more than doubled the number of high-spatial resolution remotely sensed observations at this site since the 1950s. We compare the erosion measurements to the number of open water days in a

given period, the corresponding sea surface temperature, daily air temperature, and the number and strength of storms. We also document and discuss annual and seasonal erosion patterns over the last five years in relation to historic patterns of erosion at Drew Point as well as several environmental variables thought to play a role in driving erosion of permafrost coasts.

2.3 Study area

The 9-km study coast is located in the western region of the ABSC about 100 km east of Barrow and 200 km west of Prudhoe Bay (Figure 1). The Drew Point coastal segment has historically eroded at the fastest rate along the ABSC [15,16,23] and subsequently has been the focus of several recent investigations [19,22,24-26]. This is in part due to the rapid nature of erosion at this site and its likely sensitivity to environmental forcing as well as the ability to observe change over relatively short durations. Based on values extracted from Jones et al. [19] for this 9 km segment, erosion increased from 7.0 m/yr between 1955 and 1979, to 9.4 m/yr between 1979 and 2002, to 16.3 m/yr between 2002 and 2007.

As derived from airborne LiDAR data acquired on 6 August 2011, the bluff height ranges from 1.6 m to 7.1 m with a mean of 4.4 m above the mean water level during LiDAR data acquisition. Estimates of total volumetric ice-content for permafrost along these bluffs approaches 80-90% [14] with segregated and pore ice volumes accounting for 50 to 80% [26], and wedge ice contributing nearly 30% in some locations. The remainder of the bluff composition consists of organic material and clay, silt, and sand, with the exception of coarser sandy horizons near the base of the taller bluffs. Estimates

of ice wedge polygon dimensions, range from 6-25 m with a mean size of ~15 m [14,25]. The near shore water depth is 2 m within a distance of 500 m from the shoreline and slowly drops to 3 m at 2000 m from the coast.

Rapid shoreline retreat rates in this region may partially be explained by the presence of coastal bluffs with ice-rich permafrost [22,27]. Lantuit et al. [28] demonstrated a weak but statistically significant relation between ground-ice content and mean retreat rate, with higher mean annual retreat rates typically corresponding to areas with higher ground-ice content. Block failure as a result of thermo-abrasion and thaw slump activity (thermo-denudation) are common modifiers of Arctic coastal morphology and tend to be dominant erosional processes along ice-rich coastal bluffs [22,29]. The dominant erosional process at Drew Point consists of thermo-erosional niche formation and block collapse (thermo-abrasion) although thermo-denudation does occur here on a smaller scale (Figure 2). Niche development at the base of the frozen bluff leads to the collapse of large blocks of frozen sediments, with the size of blocks strongly dependent on the ice-wedge polygon diameter [26]. These blocks then buffer the coast from further niche development until they are removed through thermal and mechanical erosion. However, as observed through time-lapse photography acquired in the field these blocks tend to persist for less than one week given the current atmospheric and oceanic conditions [26,20]. Observations made along this coast in 1901 [30] indicate that the formation of erosional-niches followed by block collapse have been modifying the coast since at least this time [31].

The nearshore open water duration at Drew Point more than doubled between 1979 and 2009, increasing from ~45 days to ~90 days, with a higher proportion of the increase in open water duration occurring in the fall (~0.9 days/yr) relative to the early summer (~0.7 days/yr) [21]. Between 2007 and 2012, the Beaufort Sea experienced the lowest September sea ice extents yet observed since the late 1970s [32]. This increase in open water days has been accompanied by a warming trend in sea surface temperature (SST) in the Beaufort Sea [5]. Air temperature has continued to increase in this region since 2000 as measured at Barrow, AK [33]. Permafrost at a depth of 20 m at coastal sites along the ABSC has also warmed by 0.6°C to 2.2°C between 1989 and 2008 [8].

There are currently no human inhabitants along this segment of coast but historical and cultural sites that date to as recent as the early to mid-1900s are located here [34]. In addition, an exploratory oil well was drilled onshore in the late-1970s. At the time it was located approximately 300 m inland [34]. This site was remediated in 2010 as a result of the increase in erosion along this coastal segment. This region provides important aquatic and terrestrial habitat to a number of migratory and resident wildlife that have been affected by erosion and storm surge flooding [24].

2.4 Imagery and methodology

2.4.1 Imagery

Our primary objective in this study revolved around mapping the changing coastline over annual and seasonal time-scales by using high spatial resolution satellite imagery (sub-meter) acquired at high temporal resolution. The ability to acquire and task high-resolution commercial, optical satellite imagery during the past several years has

increased the potential of covering a study site with suitable spatial and temporal resolution for observing the coastal bluffline in this remote Arctic setting. Between April of 2008 and June of 2013, we acquired 10 high-resolution satellite images (Table 1). Within a given year these images ranged from early April to late October and were from five different satellites: Quickbird, IKONOS, GEOEYE-1, and Worldview-1 and -2 (Figure 3). We only used the high-resolution panchromatic band provided by each of these satellites. Airborne LiDAR data for our study area was acquired on 6 August 2011, which provided a common base layer for geocorrecting all of the imagery as well as to derive information on bluff heights.

Initially, optical images were automatically orthorectified using the RPC information embedded in the image file and the LiDAR DTM (1 m postings), but the results showed variability in the position of ice-wedge intersections on the order of 2 to 5 m. So we selected 20 ground control points per image strip with the LiDAR DTM as the base and using a second order polynomial transformation the images were georectified to UTM NAD83 zone 5N with spatial resolutions ranging from 0.5 m to 1.0 m. The mean RMS associated with the georegistration process ranged from 0.44 m to 0.85 m, with a maximum RMS error always less than 1.5 m (Table 1). Visual comparison of each optical image strip for our study area showed excellent spatial agreement and suitability for further analysis (e.g. see Figure 3 for comparison).

The bluffline position in our images was manually delineated because of differences in tundra and ocean conditions at the time of image acquisition, which made automated bluffline mapping challenging (Figure 3). This difficulty in the use of

automated approaches for delineating blufflines in high-spatial resolution optical imagery was recently noted by Lantuit et al. [20] and Günther et al. [35,36]. In all images where the bluffline was clearly discernible (8 of 10), it was manually digitized in a GIS independent of one another at a scale of 1:1,000.

2.4.2 Erosion rate measurements

Erosion rate measurements of the bluffline were made at 10 m increments along the study coast using the Digital Shoreline Analysis System (DSAS v. 4) [37]. This tool has previously been used for coastal change detection studies in the Arctic [16,17,19,24,31,34] and measures the change in distance between two line vectors relative to an arbitrary baseline. The baseline in our study was created by taking a buffer of the 2008 shoreline and isolating the offshore line vector. Transects were cast every 10 m along this baseline using a 200 m smoothing algorithm to account for subtle undulations in the coastline and to ensure perpendicular transects. This resulted in 888 transects along the ~9 km baseline. Since two small segments of this coast represent small streams flowing into the ocean and not exposed coastal bluffs, these were removed from further analysis. The end result provided a measure of bluffline erosion at 876 measurement points along the study coast.

While it is difficult to assess errors in erosion rate measurements associated with this type of analysis [11], we adopted techniques used in previous coastal change detection studies [19,38,39,40]. These techniques are based on identification of factors that contribute to the error associated with feature delineation in the images under comparison (Table 2). These errors include the resolution of the imagery (0.5 to 1.0 m),

the RMS error associated with image registration, and the ability to accurately map the bluffline in the same optical image (0.14 m) as averaged from the digitization of the same image three times as an indicator of user error.

2.4.3 Sea surface temperature data

Daily SST data were derived from a hindcast, coupled sea ice-ocean model (the Bering Ecosystem Study ice-ocean Modeling and Assimilation System or BESTMAS). The BESTMAS model domain covers the northern hemisphere north of 39°N [41]. The finite-difference grid configuration of the model is based on a generalized, orthogonal, curvilinear coordinate system, which optimizes horizontal resolution along the Alaskan coast and in the Bering, Chukchi, and Beaufort Seas, ranging from an average of 4 km in Alaskan coastal areas to an average of about 10 km for the whole Chukchi and Beaufort seas. In addition, BESTMAS incorporates satellite-based measures of sea ice concentration and sea surface temperature data into the daily output product. BESTMAS is commonly used for retrospective simulations of the Arctic sea ice-ocean system from 1970 to present [41]. The near-surface water temperature (upper 5 m) of the BESTMAS ocean grid cell closest to Drew Point was used to delineate the open-water period (days with above freezing SST conditions) for each year between 2008 and 2012 as well as the variability in SST within and among years. Fetch was not included in our analysis as erosion at this site is non-fetch limited [21].

2.4.4 Meteorological data

The U.S. Geological Survey has been operating a meteorological station at Drew Point since 1998 (Figure 1). We compiled hourly air temperature data from June to

October and wind speed/direction data for the open water period for each respective year between 2008 and 2012. The hourly air temperature data have been summed to daily means and used to calculate the number of thawing degree days (based on 0°C) for each period. The wind data were used to identify wind events or storms capable of eroding the base of the bluff toe. We classified storms likely responsible for niche erosion at Drew Point as winds greater than 5 m/s [20] from directions of 0° to 90° and 270° to 360° [24] for a period of at least 12 hours with a lull not lasting longer than 6 subsequent hours. Each storm event was further summarized according to the storm-power value metric, which is described as the square of a storm's average wind velocity relative to its duration [24,42].

2.5 Results

2.5.1 Bluffline delineation from remotely sensed imagery

Of the ten images acquired during the study period we were able to distinguish the bluffline in eight. The bluffline along the 9 km study coast at Drew Point was readily distinguished in each of the examples in Figure 3. The two images where it was not possible to delineate the bluffline were affected by thick cloud cover (21 July 2011) or a continuous and thick snow cover with large drifts that obscured the bluffline (02 April 2009). Overall, error associated with the comparison of various image pairs used to derive an erosion measurement averaged 1.27 m. Error measurement estimates ranged from a low of 1.14 m to a high of 1.48 m (Table 2). These error estimates are well below the mean annual and seasonal erosion rates.

2.5.2 Annual and seasonal erosion

The mean annual bluffline erosion rate at Drew Point was 16.3 m/yr between 2008 and 2012. Mean erosion rates exceeded 16 m/yr in each year except for 2010 where the average was 6.7 m (Table 3; Figure 4). The highest mean annual erosion rate of 22.5 m occurred in 2012. Maximum annual erosion rates exceeded 40 m/yr in each year except for 2010. In 2008 the maximum annual retreat was nearly 50 m. The total volumetric loss of land along the 9 km coastal stretch as estimated from the mean bluff height for each measurement transect over the five-year study period was $2.9 \times 10^6 \text{ m}^3$. The pattern of volume loss on an annual basis was closely related to the mean distance of erosion in a given year (Table 3).

Intermediate images acquired in 2008 and 2011 allowed for the bracketing of erosion into an early season and late season interval (Table 4). Between ice-out and 20 August 2008 (25 days) mean erosion was 10.9 m and between 20 August 2008 and ice-on mean erosion was 5.2 m (58 days). In 2011, early season and late season erosion were bracketed by an image acquired on 11 September 2012 and the mean erosion was 11.3 m (49 days) and 5.7 m (36 days), respectively. Unfortunately, attempts at acquiring intermediate images during other years were hampered by the persistent coastal fog and cloud cover common in this region.

2.5.2 Environmental conditions

The number of near-shore days with above freezing SST conditions ranged from 83 in 2010 to 106 in 2012 with an average open water duration of 94 days over the five-year period (Table 3). Average open water SST during the study period was 3.7°C with a

high of 4.2°C in 2012 and a low of 3.2°C in 2008. TDDs were highest in 2012 (707) and lowest in 2008 (429) and averaged 530 over the five-year period. There were 46 storms identified during the open water periods of 2008 to 2012. Thirty-three were classified as northeasterly (0° to 90°) and 13 were classified as northwesterly (270° to 360°). Accumulated storm power ($\text{m}^2/\text{s}^2 \times \text{days}$) averaged 1,082 over the study period. The year with the highest accumulated storm power value was 2011 and the year with the lowest was 2012.

2.6 Discussion

2.6.1 Comparison to historical erosion rates at Drew Point

The Drew Point coastal segment has historically eroded at the fastest rate along the ABSC [15, 16, 23]. Jones et al. [19] documented an increase in mean annual erosion rates for this 9 km segment of coastline of 7.0 m/yr between 1955 and 1979, 9.4 m/yr between 1979 and 2002, and 16.3 m/yr between 2002 and 2007. However, it was uncertain whether the heightened erosion over the more recent five-year period was a result of one or two extreme events averaged over a shorter time period relative to the ~20 years between available images in the latter half of the 20th Century. Arp et al. [24] documented a rate of 17.1 m/yr from 2007 to 2009 for the 60 km segment of coast between Cape Halkett and Drew Point, with interannual variability in erosion over two successive years on the order of 6 m. Thus, it appeared that the increase in erosion relative to historic rates reported in Jones et al. [19] had continued over the next two years in spite of annual variation in total erosion. Results presented here that are based on the high spatial and temporal resolution remote sensing time series of bluffline erosion

indicate that the rate of erosion documented in Jones et al. [19] has generally been maintained. The mean annual erosion exceeded 16 m/yr in each of the five years with the exception of 2010 (6.7 m/yr) and this corresponds to a mean decadal-scale (2002 to 2012) erosion rate of 16.4 m/yr for this 9 km segment of coast near Drew Point (Figure 5).

2.6.2 Comparison to annual erosion at other study sites

Some assessments of long-term decadal scale erosion rates at sites in Siberia [20] and in Canada [38,43] do not find an increase in erosion relative to historic rates. However, increases in erosion over the greater ABSC may have begun in the 1980s [17,18]. Since few studies have reported on Arctic coastal erosion rates on an annual basis during the period of rapid changes in the Arctic since the early-2000s [11], it may be that other sites have responded in a similar way.

Two such examples where recent annual measurements exist also provide evidence for a shift in the pattern of erosion since the early 2000s. Tweedie et al. [12] documented recent annual erosion trends of 1 to 4 m /yr from 2003 to 2011 which is 2 to 4 times higher than historic rates reported for their ~11 km study coast located in a lagoon setting on the western ABSC [44]. The increase in erosion at this site appears to be linearly consistent ($R^2 = 0.96$) among years from 2003 to 2011 demonstrating that the conditions likely responsible for the increase in erosion have been sustained since 2003. Observations from Ice Complex deposits throughout the Laptev Sea region in Siberia also indicate a rate that is 1.5 to 3 times higher today than historic patterns [35,36].

2.6.3 Seasonal erosion patterns at Drew Point and other sites

We were able to assess seasonal variability in erosion in two of the five years analyzed. Both years (2008 and 2011) indicated that mean erosion was greatest earlier in the season relative to later in the season. Erosion was 2.1 and 2.0 times faster between break-up and late-August/early-September, relative to the intermediate image acquisitions and freeze-up. One other study has documented the seasonality associated with erosion on the ABSC. At Elson Lagoon, Tweedie et al. [12] documented patterns of seasonal erosion (ice-out to late August vs late August to ice-on) from 2007 to 2010 and reported that erosion was typically higher during the fall relative to the summer but when normalized to the number of ice-free days that erosion rates were faster in the summer period. Overeem et al. [21] hypothesized that in general the number of open water days was a good predictor of annual erosion and that the increase in the open water period in the summer would have a larger impact on erosion when compared to an increase in open water period during the fall.

2.6.4 Annual and seasonal erosion relative to environmental conditions

We compared the annual erosion patterns at Drew Point from 2008 to 2012 to a number of environmental variables that are thought to impact the rate at which permafrost coasts erode (Figure 6). The years 2009 and 2012 had the longest duration of open water and also the highest mean rates of erosion, whereas 2010 had the shortest open water duration period and the lowest mean rate. Directly comparing the number of modeled open water days to annual erosion shows good agreement (Figure 6a). Thus, as hypothesized by Overeem et al., [21] based on averages over one long-term (20 yr) and one short-term (5

yr) period, the number of open water days likely provides a good first order predictor of total annual erosion at Drew Point. Standardizing the average annual distance of erosion to the duration of the open water season shows a range of 0.18 to 0.21 m/day, with the exception of 2010 where the rate was 0.08 m/day and more similar to historic annual retreat rates (Table 3). Seasonally, the relation between open water days became less apparent. During 2008, the change rate (m/open water days) was 0.35 m/day greater during the summer relative to the fall whereas in 2011, the change rate was fairly consistent in both the summer and fall when normalized to the number of open water days in each period (Table 4). Thus, other factors were likely at play here.

The number of storms impacting the coast are somewhat related to the open water duration in each year as a longer period of open water results in a greater number of storms impacting the coast. Mean annual erosion patterns at Drew Point also show good agreement with the number of storms (Figure 6b) but seasonally this relation breaks down. The link between annual erosion and particularly seasonal erosion with storm power values calculated based on easterly and westerly storm events did not reveal a relation (Figure 6c). This could be due to the fact that the onshore wind measurements used to derive the metric may not be representative of the winds responsible for ocean wave generation and erosion of the coast. Alternatively, it could also indicate that wind events of even lesser velocities may impact this coast that we simply did not capture in our analysis. Interestingly, two large westerly storm events occurred in the early erosion season 2008, whereas no westerly storm events occurred during the entirety of the 2011 erosion season. Also, the maximum measured erosion occurred in the early season in

2008 and in the late season in 2011. This likely reflects differences in part in the direction and magnitude of storms in these two different years.

Mean annual erosion was not well correlated with sea surface and air temperatures (Figure 6d and 6e). In fact, there was essentially no correlation between erosion and SST even though this is thought to play an important role in driving erosion of permafrost coasts [26]. Thus, our representation of SST could underestimate the actual conditions prevailing along the very near-shore ocean water. The accumulated TDD sums were consistently highest during these early season periods where erosion was highest (Table 4). Furthermore, if 2010 is removed from Figure 6e the connection between TDD and annual erosion becomes much stronger ($R^2 = 0.91$). Thus, while open water duration and the number of storms appear to control the overall mean erosion at Drew Point, TDD variability among years with similar open water duration and storm conditions could help explain more subtle variations in erosion.

Recent analysis (2010 to 2012) of high-resolution satellite imagery and ground surveys from Muostakh Island in the Laptev Sea, Siberia where erosion is currently progressing at a rate ~2 times more rapid than historic measurements, found the two most important controls on annual erosion to be open water duration and summer air temperatures, with variation in TDD sums explaining the most variation ($R^2=0.95$) [36]. The high correlation between TDD and bluff top erosion at this study site result from the relative role of thermo-denudation versus thermo-abrasion operating over short time periods. However, the coupled erosion over a period of 3 years or more highlights the importance of thermo-abrasion and thermo-denudation operating together in maintaining

year-to-year trends in erosion [36]. At the Drew Point study coast, thermo-denudation is also an active process, but the dominant driver of erosion is thermo-abrasion and the collapse of large blocks of permafrost and is thus more sensitive to the number of open water days. Wobus et al. [26] reported that maximum thermo-denudation rates of the bluff top at Drew Point are 1 to 6 cm/day during the period of maximum summer insolation. These values pale in comparison to the measurable change in linear distance associated with the collapse of 9 to 12 m wide blocks of permafrost that result from development of an erosional niche due to thermo-abrasion.

One aspect not addressed in these comparisons is the inter-relation between erosion of the bluff toe in the previous year and the apparent measurement of erosion in the following year. In previous studies of bluff erosion at Drew Point some potentially important factors were not considered. Frost cracking in the winter along the ice wedges nearest the bluff edge could potentially contribute to destabilization of coastal edge polygonal blocks. Well-developed niches formed during the previous erosion season and a freezing front penetrating from two sides into the ground could contribute to more intense crack formation and block destabilization that may aid early season block failure. Following snow melt in the early summer we have observed small overflow channels disappearing in sinkholes along ice wedge troughs, suggesting that ice wedge frost cracks along the coast could be rapidly widened by spring meltwater. Thus, the winter processes associated with ice wedge cracking could play a role in early summer block collapse events and measurable erosion of the bluff edge. In addition, the erosion measured early in one year could also be a result of well-developed niches from the prior year. However,

it appears that averaging observations of erosion over a five-year period at Drew Point does an adequate job of capturing the annual variability inherent in decadal-scale observations of coastal change at this site. Modeling of the prior increase in erosion at Drew Point highlighted the important role of warmer ocean water in driving the loss of land here [25,26]. While this likely factors into the erosion equation here, the duration of the open water period in a given year coupled with the number of storms impacting the coastline currently are of more importance. Thus, our observational results are consistent with the hypothesis posed by Overeem et al. [21], indicating that open water duration and the number of storms provide a good first order predictor of erosion at this site.

2.7 Conclusion

We demonstrate the utility of high spatial resolution optical remotely sensed imagery acquired at high temporal resolution for the quantification of erosion along a rapidly eroding segment of permafrost coast in the Arctic. Mean annual erosion at Drew Point, Beaufort Sea Coast, Alaska for the open water period between 2008 and 2012 was 16.3 m/yr. Mean annual erosion varied from 6.7 m in 2010 to 22.5 m in 2012, with 2008, 2009, and 2011 eroding on average between 16 and 19 m. Updating patterns of erosion at this site over the first decade of the 21st Century indicate a mean erosion rate of 16.4 m/yr, which is 2.3 times higher than mean annual erosion rates at this site from 1955 to 1979. However, year-to-year variation in erosion between 2008 and 2012 was as high as 15.8 m indicating the importance of annual observations. Comparing the patterns in annual erosion over the recent five year period with a number of environmental variables thought to be responsible for the erosion of permafrost coasts in the Arctic shows that

open water duration and the number of storms during a given year provide good first order predictors of erosion at this site. The availability of high-spatial resolution optical satellite imagery will prove to be a valuable monitoring tool for ongoing Arctic coastal dynamics studies along permafrost influenced coastlines.

2.8 Acknowledgements

We would like to thank Paul Morin (Polar Geospatial Center at University of Minnesota) and Tom Cecere (U.S. Geological Survey) for tasking high-resolution optical imagery for Drew Point. Any use of trade, product, or firm names is for descriptive purposes only and does not imply endorsement by the US Government.

2.9 References

1. Walker, H.J. Arctic coastal geomorphology. *In* Encyclopedia of Coastal Science, Schwartz ML (ed). Springer, **2005**, pp 49–50.
2. Lantuit, H. et al. The Arctic Coastal Dynamics database: A new classification scheme and statistics on Arctic permafrost coastlines. *Estuaries and coasts* **2012**, 35(2), 383-400.
3. Stroeve, J.C.; Serreze, M.C.; Holland, M.M.; Kay, J.E.; Malanik, J.; Barrett A.P. The Arctic's rapidly shrinking sea ice cover: a research synthesis. *Clim. Change* **2012**, 110, 1005-1027.
4. ACIA (Arctic Climate Impact Assessment). *Impacts of a warming arctic: arctic climate impact assessment*, Cambridge University Press, Cambridge, UK, 2004.
5. Steele, M.; Ermold, W.; Zhang, J. Arctic Ocean surface warming trends over the past 100 years. *Geophys. Res. Lett.* **2008**, 35(2), L02614.
6. Richter-Menge, J. (Ed.). (2011). *Arctic report card 2010*. DIANE Publishing.
7. Romanovsky, V.E.; Smith, S.L.; Christiansen, H.H. Permafrost thermal state in the polar Northern Hemisphere during the international polar year 2007–2009: A synthesis. *Permafr. and Periglac. Process.* **2010**, 21, 106-116.
8. Smith, S.L. et al. Thermal state of permafrost in North America: A contribution to the International Polar Year. *Permafr. and Periglac. Process.* **2010**, 21, 117-135.

9. Simmonds, I.; Rudeva, I. The great Arctic cyclone of August 2012, *Geophys. Res. Lett.* **2012**, 39, L23709, doi:10.1029/2012GL054259.
10. Vermaire, J. C.; Pisaric, M.F.J.; Thienpont, J.R.; Courtney Mustaphi, C.J.; Kokelj, S.V.; Smol, J.P. Arctic climate warming and sea ice declines lead to increased storm surge activity, *Geophys. Res. Lett.* **2013**, 40, 1386–1390, doi:10.1002/grl.50191.
11. Lantuit, H.; Overduin, P.P.; Wetterich, S. Recent Progress Regarding Permafrost Coasts. *Permafrost and Periglacial Processes*. **2013**, 24(2), 120-130.
12. Tweedie, C.E.; Aguire, A.; Vargas, C.S.; Brown, J. Spatial and temporal dynamics of erosion along the Elson Lagoon Coastline near Barrow, Alaska (2002-2011). In *Proceedings of the Tenth International Conference on Permafrost* **2012**, 425-430.
13. Forbes, D.L.; Kremer, H.; Lantuit, H.; Rachold, V.; Reiersen, L.O. *State of the Arctic Coast 2010: Scientific Review and Outlook*. Land-Ocean Interactions in the Coastal Zone, Institute of Coastal Research, 2011.
14. Kanevskiy, M. et al. Ground ice in the upper permafrost of the Beaufort Sea coast of Alaska. *Cold Reg. Science and Technol.* **2012**, 56-70.
15. Jorgenson, M.T.; Brown, J. Classification of the Alaskan Beaufort Sea Coast and estimation of carbon and sediment inputs from coastal erosion. *Geo-Marine Letters* **2005**, 25(2-3), 69-80.
16. Gibbs, A.E.; Harden, E.L.; Richmond, B.M.; Erikson, L.H. Regional shoreline change and coastal erosion hazards in Arctic Alaska. In *Solutions to Coastal Disasters 2011: Proceedings of the 2011 Solutions to Coastal Disasters Conference* **2012**, 25-29.
17. Ping, C.L.; Michaelson, G.J.; Guo, L.; Jorgenson, M.T.; Kanevskiy, M.; Shur, Y.; Dou, F.; Liang, J. Soil carbon and material fluxes across the eroding Alaska Beaufort Sea coastline. *J. Geophys. Res.* **2011**, 116, G02004.
18. Mars J.; Houseknecht, D. Quantitative remote sensing study indicates doubling of coastal erosion rate in past 50 yr along a segment of the Arctic coast of Alaska. *Geology* **2007**, 35, 583-586.
19. Jones, B.M.; Arp, C.D.; Jorgenson, M.T.; Hinkel, K.M.; Schmutz, J.A.; Flint, P.L. Increase in the rate and uniformity of coastline erosion in Arctic Alaska. *Geophys. Res. Lett.* **2009**, 36(3), L03503.
20. Lantuit, H.; Atkinson, D.; Overduin, P.P.; Grigoriev, M.; Rachold, V.; Grosse, G.; Hubberten, H.W. Coastal erosion dynamics on the permafrost-dominated Bykovsky Peninsula, north Siberia, 1951-2006. *Polar Res.* **2011**, 30, 7341.

21. Overeem, I.; Anderson, R.S.; Wobus, C.W.; Clow, G.D.; Urban, F.E.; Matell, N. Sea ice loss enhances wave action at the Arctic coast. *Geophys. Res. Lett.* **2011**, *38*(17), L17503.
22. Aré F.E. Thermal abrasion of sea coast. *Polar Geogr. and Geol.* **1988**, *12*, 1-157.
23. Reimnitz, E.; Graves, S.M.; Barnes, P.W. Beaufort Sea coastal erosion, sediment flux, shoreline evolution, and the erosional shelf profile. *U.S. Geol. Surv. Open-File Report* **1985**, 85-380, 1-67.
24. Arp, C.D.; Jones, B.M.; Schmutz, J.A.; Urban, F.E.; Jorgenson, M.T. Two mechanisms of aquatic and terrestrial habitat change along an Alaskan Arctic coastline. *Polar Biol.* **2010**, *33*(12), 1629-1640.
25. Ravens, T.M.; Jones, B.M.; Zhang, J.; Arp, C.D.; Schmutz, J.A. Process-Based Coastal Erosion Modeling for Drew Point, North Slope, Alaska. *J. of Waterw., Port, Coast., and Ocean Eng.* **2011**, *138*(2), 122-130.
26. Wobus, C.; Anderson, R.; Overeem, I.; Matell, N.; Clow, G.; Urban, F. Thermal erosion of a permafrost coastline: Improving process-based models using time-lapse photography. *Arct., Antarct., and Alp. Res.* **2011**, *43*(3), 474-484.
27. Dallimore, S.R.; Wolfe, S.A.; Solomon, S.M. Influence of ground ice and permafrost on coastal evolution, Richards Island, Beaufort Sea coast, N.W.T. *Can. J. of Earth Sci.* **1996**, *33*, 664-675.
28. Lantuit, H.; Overduin, P.P.; Couture, N.; Odegard, R.S. Sensitivity of coastal erosion to ground ice contents: an Arctic-wide study based on the ACD classification of Arctic coasts. In *NICOP 2008: Proceedings of the 9th International Conference on Permafrost*, D.L. Kane and K.M. Hinkel (Eds.) **2008**, pp. 1025-1029.
29. Walker, H.J. Permafrost and coastal processes. *Proceedings of the Fifth International Conference on Permafrost* **1988**, *3*, 35-42.
30. Schrader, F.C. A reconnaissance in northern Alaska across the Rocky Mountains, along the Koyukuk, John, Anaktuvuk, and Colville rivers, and the Arctic coast to Cape Lisburne, in 1901, with notes by W.T. Peters. *U.S. Geol. Surv. Prof. Paper* **1904**, *20*, pp. 1-139.
31. Jones, B.M.; Arp, C.D.; Beck, R.A.; Grosse, G.; Webster, J.M.; Urban, F.E. Erosional history of Cape Halkett and contemporary monitoring of bluff retreat, Beaufort Sea coast, Alaska. *Polar Geogr.* **2009**, *32*(3-4), 129-142.

32. Ballinger, T.J.; Rogers, J.C. Atmosphere and Ocean Impacts on Recent Western Arctic Summer Sea Ice Melt. *Geogr. Compass* **2013**, 7(10), 686-700.
33. Wendler, G.; Chen, L.; Moore, B. The First Decade of the New Century: A Cooling Trend for Most of Alaska. *Open Atmos. Sci. J.* **2012**, 6, 111-116.
34. Jones, B.M.; Hinkel, K.M.; Arp, C.D.; Eisner, W.R. Modern erosion rates and loss of coastal features and sites, Beaufort Sea coastline, Alaska. *Arctic* **2008**, 61, 361-372.
35. Günther, F.; Overduin, P.P.; Sandakov, A.V.; Grosse, G.; Grigoriev, M.N. Short- and long-term thermo-erosion of ice-rich permafrost coasts in the Laptev Sea region. *Biogeosciences* **2013**, 10, 4297-4318, doi:10.5194/bg-10-4297-2013.
36. Günther, F.; Overduin, P.P.; Baranskaya, A.; Opel, T.; Grigoriev, M.N. Observing Muostakh Island disappear: erosion of a ground-ice-rich coast in response to summer warming and sea ice reduction on the East Siberian shelf. *The Cryosphere Discuss.* **2013**, 7, 4101-4176, doi:10.5194/tcd-7-4101-2013.
37. Thieler, E.; Himmelstoss, E.A.; Zichichi, J.L.; Ergul, A. The Digital Shoreline Analysis System(DSAS) Version 4. 0- An ArcGIS Extension for Calculating Shoreline Change. U. S. Geological Survey, 2009.
38. Hapke, C.J. Estimation of regional material yield from coastal landslides based on historical digital terrain modeling. *Earth Surf. Process. Landf.* **2005**, 30, 679-697.
39. Lantuit H.; Pollard W.H. Fifty years of coastal erosion and retrogressive thaw slump activity on Herschel Island, southern Beaufort Sea, Yukon Territory, Canada. *Geomorphology* **2008**, 95, 84-102.
40. Gorokhovich, Y.; Leiserowiz, A. Historical and future coastal changes in northwest Alaska. *J. of Coast. Res.* **2011**, 28(1A), 174-186.
41. Zhang, J.; Woodgate, R.; Moritz, R. Sea ice response to atmospheric and oceanic forcing in the Bering Sea. *J. of Phys. Oceanograph.* **2010**, 40(8), 1729-1747.
42. Atkinson, D.E. Observed storminess patterns and trends in the circum-Arctic coastal regime. *Geo-Marine Lett.* **2005**, 25(2-3), 98-109.
43. Solomon, S.M. Spatial and temporal variability of shoreline change in the Beaufort Mackenzie region, north- west territories, Canada. *Geo-Marine Lett.* **2005**, 25, 127-137.
44. Brown, J.; Jorgenson, M.T.; Smith, O.P.; Lee, W. Long- term rates of erosion and carbon input, Elson Lagoon, Barrow, Alaska. In *ICOP 2003 Permafrost: Proceedings of*

the 8th International Conference on Permafrost. M. Phillips, S.M. Springman, and L.U. Arenson, (Eds.) A.A. Balkema Publishers, Netherlands, **2003**, pp. 101-106.

2.10 Figures

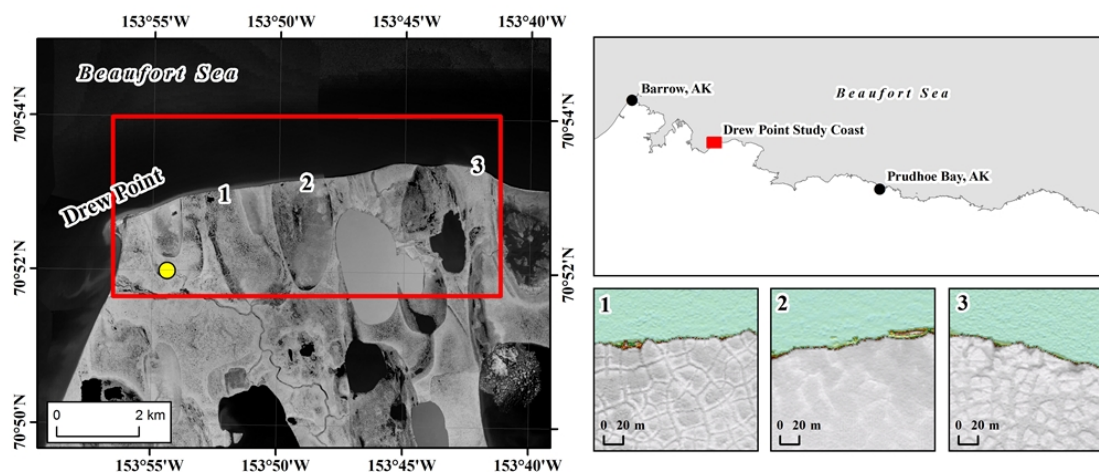


Figure 1. Drew Point study coast along Beaufort Sea. Rapidly eroding segment of Alaskan Beaufort Sea Coast (ABSC) near Drew Point. The overlapping footprint of remotely sensed imagery used in this study outlined with the red rectangle. The location of the meteorological station is shown with the yellow dot. Examples of ice-wedge polygonal networks along the coastal bluffs are shown in LiDAR image subsets. (1) Low-centered ice wedge polygons typical of the study area, (2) poorly developed ice wedge polygon network in a “young” drained lake basin, and (3) high-centered ice wedge polygons typical of upland sites. The location of Drew Point along the ABSC is shown with the red rectangle in the inset in the upper right.

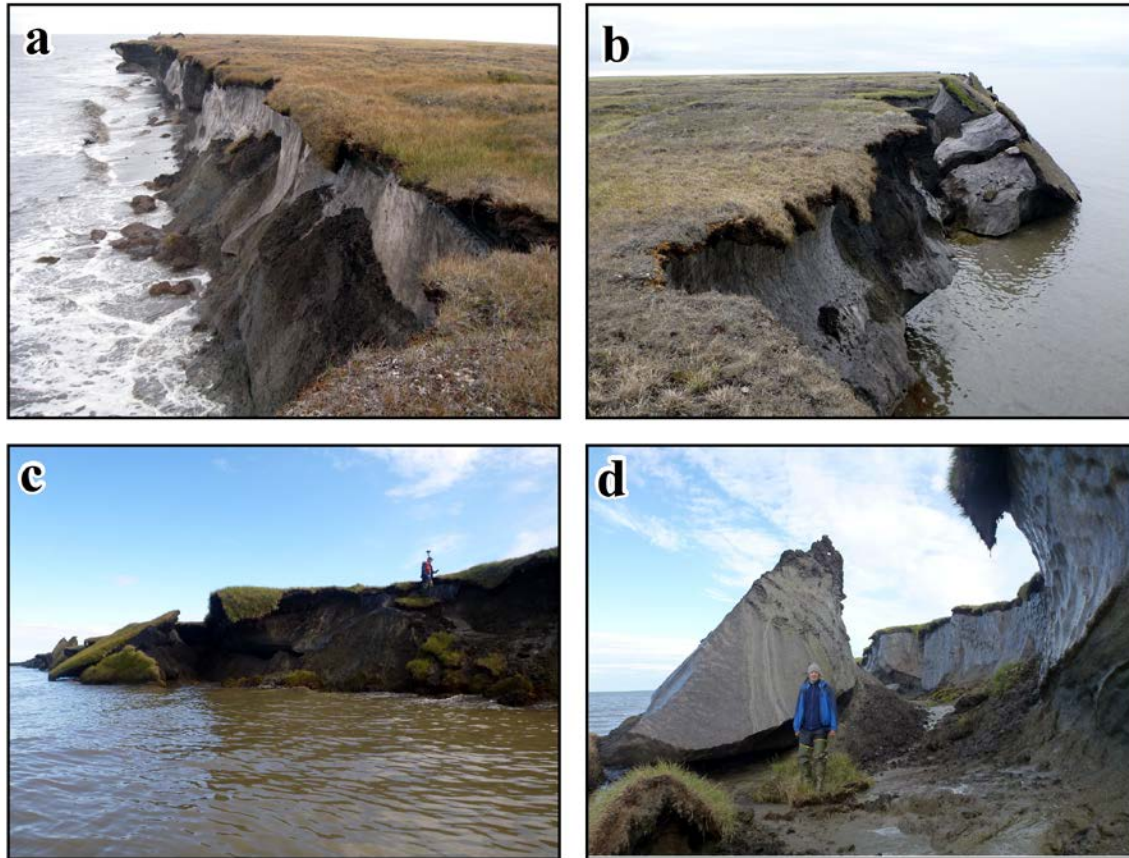


Figure 2. Field photographs showing erosional processes. Field photographs demonstrating the dominant erosional process of niche erosion and block collapse at Drew Point. (a) The exposed ice-rich bluff face showing development of a niche prior to a block collapse episode. (b) A photo of the study coast showing a well-developed niche and collapsed blocks of permafrost. (c) A photo looking back towards a 5 m high bluff from a small boat showing large collapsed blocks of permafrost as well as smaller-scale thermo-denudation to the right of the 1.9 m tall person. (d) A photo from the base of the bluff looking along a series of connected ice wedges showing the collapse of a block of permafrost along a 7 m high bluff. Note 1.9 m tall person for scale.

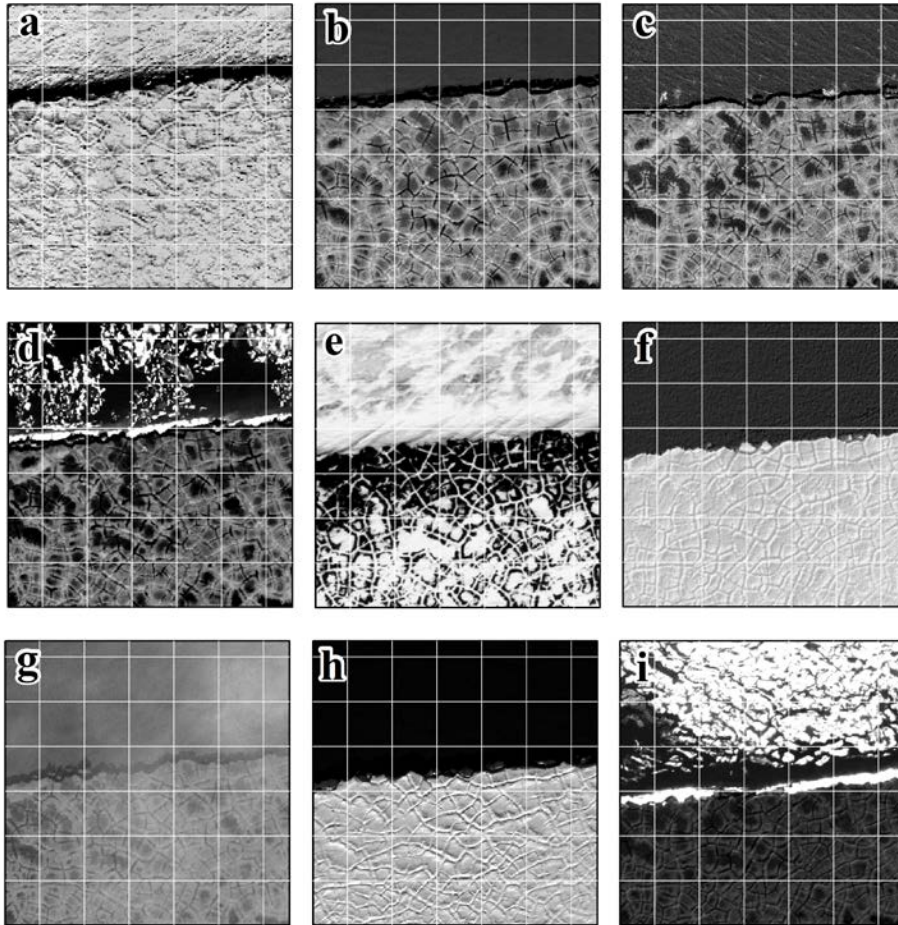


Figure 3. High-resolution satellite imagery. Example of a subset of the high resolution imagery sources for the same segment of coast between 2008 and 2013. The grid in each frame represents 50 m x 50 m. (a) Quickbird image from 06 April 2008 and the ability to distinguish the bluffline despite a continuous snow cover. (b) IKONOS image, the lowest resolution image in our study, from 20 August 2008. (c) Geoeye-1 image from 20 July 2009 during a period of relative strong northeasterly winds. (d) Worldview-1 image from 09 July 2010 and the ability to distinguish the bluffline despite remnant snow drifts persisting along the coast. (e) Worldview-2 image from 21 May 2011 during the initial phase of snow melt on the tundra and the ability to distinguish the bluffline in spite of large drifts along the bluff face. (f) LiDAR image from 06 August 2011 used in the geocoding of all optical images. (g) Worldview-1 image from 12 September 2011 and the ability to delineate the bluffline during the presence of patchy, broken coastal fog. (h) Worldview-1 image from 09 October 2011 and the nice contrast between fresh snowfall on the tundra and the unfrozen ocean. (i) Worldview-2 image from 22 June 2013, the final image in the time series, and similar conditions as observed in Figure 3d. This image was used to bracket the end of the 2012 erosion season since no erosion should have occurred during the winter.

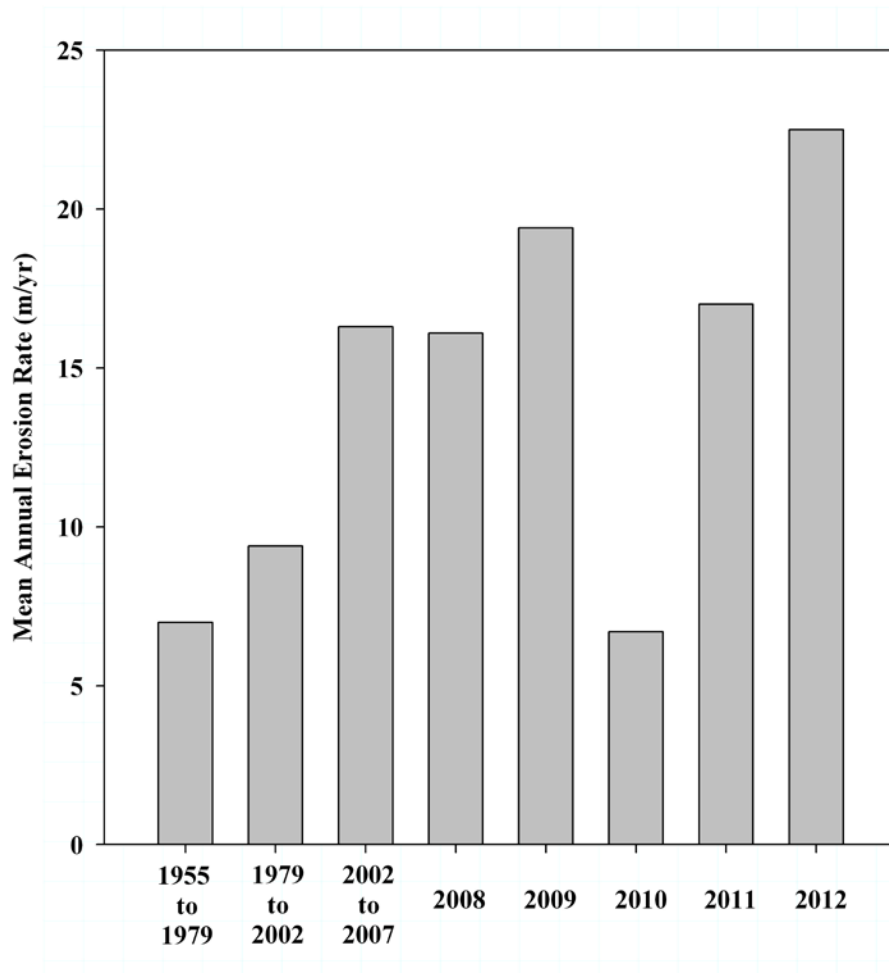


Figure 4. Decadal and annual erosion rates. Erosion rates measured for the Drew Point study coast for the periods 1955 to 1979 [18], 1979 to 2002 [18], 2002 to 2007 [18], and annually since 2008. Annual erosion exceeded 16 m/yr in every year except 2010 (6.7 m/yr). The mean decadal erosion rate from 2002 to 2012 is 16.4 m/yr indicating that the heightened erosion documented in Jones et al. 2009a has been maintained at this site, with the exception of 2010.

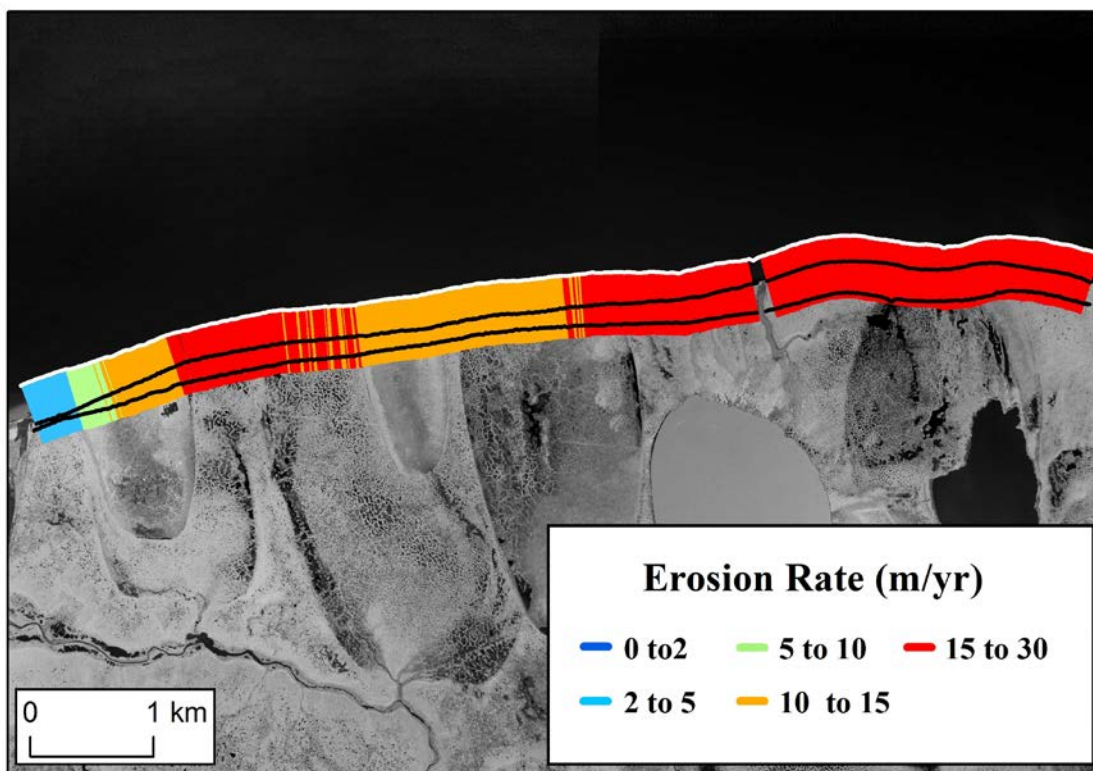


Figure 5. Mean annual erosion rate from 2002 to 2012. The erosion rate for the decade spanning from 2002 to 2012 along the Drew Point study coast. The generalized baseline (white line) used as a reference for the orthogonal transects (colored coded to erosion rate) are shown along with the 2002 and 2012 bluff top edge lines (black).

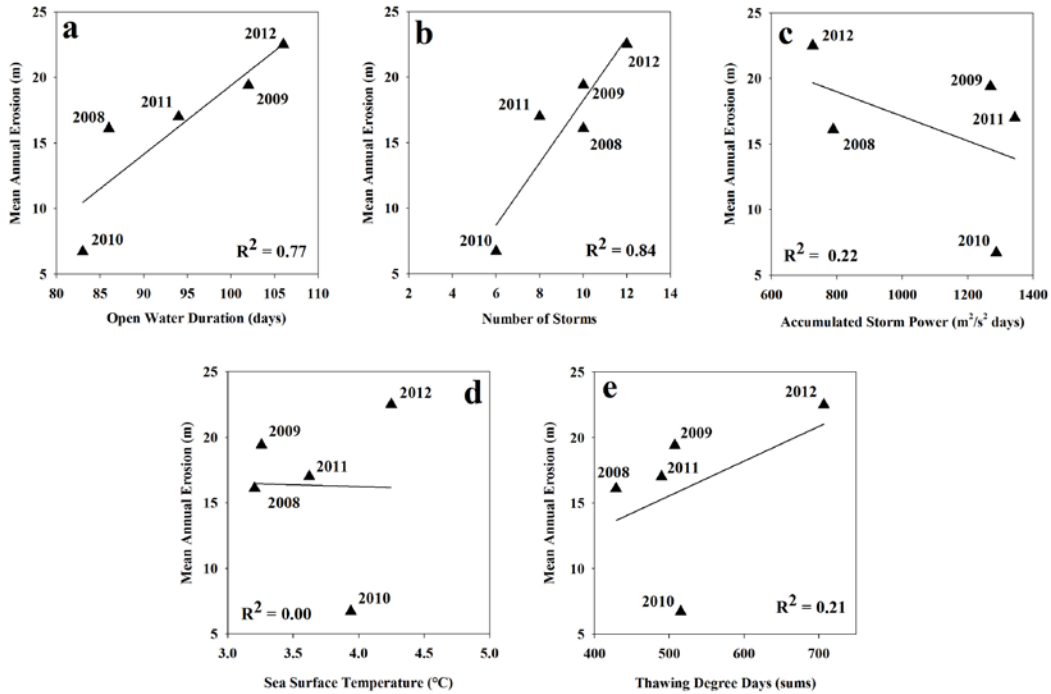


Figure 6. Scatterplots of erosion vs. environmental conditions. Scatterplots comparing mean annual erosion from 2008 to 2012 to (a) open water duration, (b) number of storms from the east and the west, (c) total accumulated storm power, (d) sea surface temperature during the open water period, and (e) summertime (June to September) thawing degree day sums.

2.11 Tables

Table 1. Satellite imagery information. Overview table describing image date, image source, observation geometry, georectification results, whether the image was incorporated into the coastal change analysis, and comments associated with a particular image.

Date	Image Type	Incidence Angle (°)	Pixel Resolution (m)	RMS Mean	RMS Min	RMS Max	GCPs	Polynomial	Blufftop Delineated	Comments
6-Apr-08	Quickbird	28.0	0.6	0.78	0.29	1.22	20	2nd Order	Yes	Continuous snow cover but good contrast along bluffline
20-Aug-08	IKONOS	8.9	1.0	0.44	0.09	0.83	20	2nd Order	Yes	Good contrast along bluffline
2-Apr-09	Worldview-1		0.5	-	-	-	-	-	No	Snow drifts prevented bluffline delineation
20-Jul-09	Geoeye-1	18.1	0.5	0.61	0.13	1.30	20	2nd Order	Yes	Good contrast along bluffline
9-Jul-10	Worldview-1	18.1	0.5	0.63	0.17	1.15	20	2nd Order	Yes	Good contrast along bluffline
25-May-11	Worldview-2	15.3	0.5	0.67	0.22	1.15	20	2nd Order	Yes	Patchy snow cover but good contrast along bluffline
21-Jul-11	Worldview-2		0.5	-	-	-	-	-	No	100% cloud cover
12-Sep-11	Worldview-1	22.9	0.5	0.60	0.13	1.08	20	2nd Order	Yes	Good contrast along bluffline
9-Oct-11	Worldview-1	21.2	0.5	0.85	0.33	1.50	20	2nd Order	Yes	Good contrast along bluffline
22-Jun-13	Worldview-2	5.6	0.5	0.61	0.11	1.26	20	2nd Order	Yes	Good contrast along bluffline

Table 2. Erosion rate error estimates and mean erosion. Quantitative estimate of error associated with erosion measurements from the satellite imagery. The estimate is based on the spatial resolution of the sensor, the mean RMS error of the georegistration process, and a digitization or user error. The measurement error between an image pair is provided as the dilution of accuracy as coined by Lantuit et al. [20]. The mean erosion between each image comparison is also provided.

Image Source	Date	Spatial Resolution (m)	Mean RMS Error (m)	Digitization Error (m)	Dilution of Accuracy (m)	Mean Erosion (m)
Quickbird	6-Apr-08	0.6	0.78	0.14		
Ikonos	20-Aug-08	1.0	0.44	0.14	1.48	10.9
Ikonos	20-Aug-08	1.0	0.44	0.14		
Geoeye 1	20-Jul-09	0.5	0.61	0.14	1.36	5.2
Geoeye 1	20-Jul-09	0.5	0.61	0.14		
Worldview 1	9-Jul-10	0.5	0.63	0.14	1.14	19.4
Worldview 1	9-Jul-10	0.5	0.63	0.14		
Worldview 2	25-May-11	0.5	0.67	0.14	1.18	6.7
Worldview 2	25-May-11	0.5	0.67	0.14		
Worldview 1	12-Sep-11	0.5	0.60	0.14	1.16	11.3
Worldview 1	12-Sep-11	0.5	0.60	0.14		
Worldview 1	9-Oct-11	0.5	0.85	0.14	1.27	5.7
Worldview 1	9-Oct-11	0.5	0.85	0.14		
Worldview 2	22-Jun-13	0.5	0.61	0.14	1.28	22.5

Table 3. Mean annual erosion and environmental conditions. Mean annual erosion along the Drew Point study coast from 2008 to 2012 relative to hypothesized environmental variables potentially responsible for the pattern of land loss. The mean erosion, total volume loss, number of open water days, open water mean sea surface temperature, summertime (June to September) thawing degree days, the number of storms, and corresponding storm power value are provided for context.

Year	Mean Annual Erosion (m)	Volume Loss (x 10⁶ m³)	Open Water Period (Days)	Open Water SST (°C)	Thawing Degree Days (Based on 0° C)	Number of Storms (West/East)	Accumulated Storm Power (m²/s² x days)
2008	16.1	0.55	86	3.21	429	10 (5/5)	788
2009	19.4	0.72	102	3.26	507	10 (2/8)	1269
2010	6.7	0.24	83	3.94	515	6 (1/5)	1287
2011	17.0	0.60	94	3.62	490	8 (0/8)	1343
2012	22.5	0.81	106	4.25	707	12 (5/7)	726

Table 4. Mean seasonal erosion and environmental conditions. Seasonal erosion measurements at Drew Point in 2008 and 2011. The mean erosion, maximum erosion, number of open water days, erosion per open water days, thawing degree days, mean sea surface temperature, the number of storms, and corresponding storm power value are provided for context.

Erosion Year	Erosion Season	Mean Erosion (m)	Maximum Erosion (m)	Number of Open Water Days	Change Rate (m/open water days)	Mean Sea Surface T (°C)	Number of Storms (West/East)	Storm Power Value (m²/s² x days)
2008	Early	10.9	45.3	25	0.44	1.3	3 (2/1)	347
	Late	5.2	18.4	58	0.09	4.1	7 (3/4)	441
2011	Early	11.3	17.8	49	0.23	3.0	3 (0/3)	125
	Late	5.7	34.2	36	0.16	4.2	5 (0/5)	1218

Chapter 3: Modern thermokarst lake dynamics in the continuous permafrost zone, northern Seward Peninsula, Alaska²

3.1 Abstract

Quantifying changes in thermokarst lake extent is of importance for understanding the permafrost-related carbon budget, including the potential release of carbon via lake expansion or sequestration as peat in drained lake basins. We used high-spatial resolution remotely sensed imagery from 1950/51, 1978, and 2006/07 to quantify changes in thermokarst lakes for a 700 km² area on the northern Seward Peninsula, Alaska. The number of water bodies larger than 0.1 ha increased over the entire observation period (666 to 737 or +10.7%), however, total surface area decreased (5,066 ha to 4,312 ha or -14.9%). This pattern can largely be explained by the formation of remnant ponds following partial drainage of larger water bodies. Thus, analysis of large lakes (>40 ha) shows a decrease of 24% and 26% in number and area, respectively, differing from lake changes reported from other continuous permafrost regions. Thermokarst lake expansion rates did not change substantially between 1950/51 and 1978 (0.35 m/yr) and 1978 and 2006/07 (0.39 m/yr). However, most lakes that drained did expand as a result of surface permafrost degradation before lateral drainage. Drainage rates over the observation period were stable (2.2 to 2.3 lakes/year). Thus, analysis of decadal-scale, high spatial resolution imagery has shown that lake drainage in this region

² Jones, B. M., G. Grosse, C. D. Arp, M. C. Jones, K. M. W. Anthony, and V. E. Romanovsky (2011), Modern thermokarst lake dynamics in the continuous permafrost zone, northern Seward Peninsula, Alaska, *Journal of Geophysical Research Biogeosciences* 116, G00M03, doi:10.1029/2011JG001666.

is triggered by lateral breaching and not subterranean infiltration. Future research should be directed towards better understanding thermokarst lake dynamics at high spatial and temporal resolution as these systems have implications for landscape-scale hydrology and carbon budgets in thermokarst lake-rich regions in the circum-Arctic.

3.2 Introduction

Thermokarst refers to the process by which characteristic landforms form following disturbance of the thermal equilibrium of the ground resulting in thaw of ice-rich permafrost or melting of massive ice [van Everdingen, 1998]. In areas with relatively low relief, a thick overburden of unconsolidated sediments, and high ground-ice content, this often results in the formation of thermokarst lakes. Thermokarst lakes are one of the most dynamic features in Arctic and sub-Arctic lowland landscapes as the lakes, besides facilitating further thaw settlement, often expand laterally through thermal and mechanical erosional processes. Thus, the lateral and vertical dynamics of thermokarst lake change results in complex interactions with topography, streams, neighboring thermokarst lakes, and permafrost. Given current and projected Arctic climate change it is important to conduct studies on thermokarst lake dynamics as they are thought to be an indicator of the effects of climate change on the landscape at least over broad geographic scales [Smith et al., 2005].

Thermokarst lakes have mainly formed during the course of the Holocene and are a sign of local permafrost degradation following post glacial climate warming [Rampton, 1988; Romanovskii et al., 2004; Walter et al., 2007]. Thermokarst lakes are abundant surface features across many high latitude regions, such as the Seward Peninsula

[Hopkins, 1949; West and Plug, 2008; Plug and West, 2009], the Arctic Coastal Plain [Sellmann et al., 1975; Hinkel et al., 2005] as well as several areas in Interior Alaska [Jorgenson and Osterkamp, 2005]; in Canada on Banks Island [Harry and French, 1983], Tuktoyaktuk Peninsula [Mackay, 1988], the Yukon Coastal Plain [West and Plug, 2008; Plug and West, 2009], and Richards Island [Burn, 2002], and in large regions of Siberia [Romanovskii et al., 2004, Tomirdiaro and Ryabchun, 1973; Zimov et al., 1997; Smith et al., 2005; Grosse et al., 2006; Walter et al., 2007; Grosse et al., 2013]. While not all northern, high-latitude lakes are of thermokarst origin [Jorgenson and Shur, 2007; Smith et al., 2007], their importance to global climate change and northern high latitude soil and permafrost-stored carbon cycling has been noted [Zimov et al., 1997; Walter et al., 2006; Walter et al., 2007]. Therefore quantifying changes in thermokarst lakes is of importance for understanding potential positive and negative feedbacks to the atmospheric carbon budget.

A suite of recent studies have utilized remotely sensed imagery to document changes in thermokarst lake extent in various locations across the Arctic and sub-Arctic (Figure 1). In general, thermokarst lakes are thought to be increasing in abundance and surface area in regions of continuous permafrost and decreasing in abundance and surface area in transitional permafrost zones (discontinuous, isolated, sporadic) [Smith et al., 2005]. For example, Smith et al. [2005] examined coarse resolution satellite imagery (150 m) to detect surface-area changes in lakes (≥ 40 ha) from 1973 to 1997/98 over a broad expanse of West Siberia ($\sim 515,000$ km²). They found that lakes had decreased by 11% during this time period, though the changes were not uniform across the study area.

Lake abundance and surface area decreased in the zones of discontinuous, sporadic, and isolated permafrost, while both increased in the zone of continuous permafrost. Lake change in Alaska also appears to follow this general pattern, though interpretation differs as to the relative roles of increasing aridity and permafrost dynamics [Riordan et al., 2006; Yoshikawa and Hinzman, 2003]. Recent studies have also shown the importance of precipitation on thermokarst lake surface area extent and its detection in moderate resolution (30 m) remotely sensed imagery [Plug et al., 2008; Jones et al., 2009a; Labrecque et al., 2009].

It has long been shown that thermokarst lakes have a tendency to drain laterally [Hopkins, 1949; Mackay, 1988; Brewer et al., 1993; Hinkel et al., 2007; Marsh et al., 2009]. Typical thermokarst lake drainage mechanisms in the continuous permafrost zone consist of bank overflow, ice-wedge degradation and development of a drainage network, headward stream erosion, lake tapping, coastal erosion, as well as expansion of a lake towards a drainage gradient. A few recent studies that have focused on drainage of thermokarst lakes in continuous permafrost environments found that rates of drainage have been fairly low [Hinkel et al., 2007] or even decreasing during the last ca. 50 years [Marsh et al., 2009]. However, the specific external or internal forcing mechanism remains poorly understood.

In order to more fully understand landscape dynamics in a thermokarst lake-rich landscape and their potential role in the northern high-latitude carbon cycle it is imperative to assess the balance between lake expansion and lake drainage. Since thermokarst lakes have been shown to act as an effective mechanism for the release of

organic carbon previously frozen in permafrost and since drainage of thermokarst lakes allows for organic carbon sequestration through the accumulation of peat in drained basins, landscape-scale analyses of carbon cycling should account for thermokarst lake dynamics. The objectives of our study were (1) to employ high spatial resolution remotely sensed imagery (1 m) acquired between 1950 and 2007 to detect changes in thermokarst lake extent in continuous permafrost on the northern Seward Peninsula, Alaska; (2) to quantify rates of change and analyze whether these rates changed over time; (3) to identify potential mechanisms of lake expansion and lake area loss; and (4) discuss implications of thermokarst lake change for the carbon cycling in these landscapes.

3.3 Study area

Our study area is located on the northern Seward Peninsula in northwestern Alaska, USA (Figure 1, site 12) and bounded by the Chukchi Sea to the north, Kotzebue Sound to the east, and Devil Mountain volcano and a chain of large maar lakes to the south (Figure 2). The northern Seward Peninsula represents one of the major lake districts in Alaska, where 7% of the 6,418 km² land area is covered in extant lakes larger than 1 ha [Arp and Jones, 2009]. This region is located in the central portion of Beringia, which during the Last Glacial Maximum (19-26.5 kyr ago) formed a largely non-glaciated land mass with exposed shelves between Siberia and Alaska (Figure 1) [Hopkins, 1967].

Throughout the Wisconsinan, much of the lowlands in the Bering Land Bridge were characterized by the accumulation of eolian and alluvial silt originating from braided floodplains crossing the exposed shelves and the formation of syngenetic

permafrost and ice-wedges [Hopkins et al., 1955]. For the northern Seward Peninsula region, wind-deposition is the favorable hypothesis for the aggradation of this land surface as silt/loam textures and grain-size analyses are typical of loess, and also due to the fact that the silt drapes the paleolandscape [Höfle et al., 2000]. Roughly 21.5 kyr ago, a hydromagmatic eruption created the Devil Mountain Maar Lake, the largest known maar on Earth, and deposited tephra over a 2,500 km² area in the Cape Espenberg lowlands of the northern Seward Peninsula [Beget et al., 1996]. Close to the maar lake the tephra thickness exceeds tens of meters, whereas in distal places thicknesses may still reach 1 m. The primary direction of the tephra outfall was to the north and west of the eruption [Beget et al., 1996], creating a matrix of ice-rich silt blanketed by volcanic tephra, which has subsequently been capped further by Late Pleistocene silt and a cover layer of Holocene soils and peat [Höfle et al., 2000].

Throughout the Holocene, much of the land surface in this region has been subject to permafrost degradation and thermokarst processes [Hopkins, 1949; Charron, 1995]. With a mean annual ground temperature of $\sim -3^{\circ}\text{C}$, the continuous permafrost in the study area is relatively warm today [Smith et al., 2010], but conditions remain favorable for the formation of permafrost and epigenetic ice wedges following drainage of thermokarst lakes [Hopkins et al., 1955]. The reworking of the landscape by thermokarst processes is clearly evident in the topography and landscape terrain. Within our 700 km² study area, a subset of the Cape Espenberg Lowland-Devil Mountain region (Figure 2), 73% of the landscape has been influenced by the formation and/or drainage of thermokarst lakes [Charron, 1995]. The ratio of thermokarst lake-affected vs. non lake-

affected landscape units in the study region is very similar to other ice-rich permafrost regions in northern Alaska [Hinkel et al., 2005] and Siberia [Grosse et al., 2006].

The vegetation of the northern Seward Peninsula is characterized as Bering Tundra. Ericaceous shrubs, including *Empetrum nigrum*, *Vaccinium uliginosum*, and *V. oxycoccus*, are common on the uplands, along with *Betula nana*, *Salix* spp., *Eriophorum vaginatum*, *Sphagnum fuscum*, *Rubus chamaemorus*, and *Polytrichum strictum*. Water-logged lowlands, including low-centered ice-wedge polygons and drained lake basins, are dominated by *Carex aquatilis*, *Eriophorum angustifolium*, *Eriophorum scheuchzeri*, and *Sphagnum riparium*. Mean annual temperature of the region is -6.1°C based on the 1971 to 2000 climate normal period, recorded at Kotzebue, Alaska, which is located on the Baldwin Peninsula roughly 80 km to the northwest (Figure 2). Mean July temperature is 12.6°C (warmest month) while mean February temperature is -19.7°C (coldest month). Mean annual precipitation is 255 mm with slightly more than half (130 mm) falling between July and September, presumably in the form of rainfall.

3.4 Methods

3.4.1 Imagery and classification

We used high-spatial resolution, contemporary satellite imagery and historical aerial photography, to quantify changes in thermokarst lakes and ponds larger than 0.1 ha from 1950 to 2007 (Table 1). Pan-sharpened, multi-spectral IKONOS[©] satellite imagery from 2006 and 2007 with a resolution of 1 m was available for a large portion of the Cape Espenberg Lowland-Devil Mountain region and its cloud-free extent defines our 700 km² study area (Figure 2). The imagery was georegistered to 1 m resolution, orthorectified,

aerial photography available for a portion of the region [Manley et al., 2007a-c]. In areas without recent orthorectified aerial imagery, terrain-corrected Landsat ETM+ imagery (processing level L1T) was used with stable lake centroids as additional control points [Sheng et al., 2008].

We compared lake and pond surface area from the registered IKONOS© imagery to orthorectified black and white photography from 1950/51 [Manley et al., 2007a] and orthorectified color infrared (CIR) photography from 1978 [Manley et al., 2007b]. For areas outside of the coverage provided by the Manley et al. [2007a-c] datasets, we acquired the appropriate aerial image frames from the U.S. Geological Survey, EROS Data Center in Sioux Falls, SD, USA and registered the frames to the IKONOS© imagery. In total, this required nine additional frames from ca. 1950 and three additional frames from 1978. Overall, mean RMS values associated with the Manley et al. [2007a, b] orthodatasets were 1.7 m for the 1950/51 imagery and 1.1 m for the 1978 imagery. Mean RMS values for the additional frames required to cover the study area were 1.5 m and 1.6 m, respectively.

We classified the imagery into water and non-water binary raster files using object-oriented classification algorithms available in the image processing software eCognition® [Frohn et al., 2005]. Each frame was processed with the multi-resolution segmentation parameter within eCognition® at a scale parameter of 10, shape factor of 0.1, and compactness and smoothness factor of 0.5 in the normal mode. This essentially converted the image from individual pixels, into pixels grouped as like objects, which nearly perfectly delineates lake and pond perimeters. The image was subjected to an

additional segmentation in spectral differencing mode that grouped like objects further. Following the second segmentation, the objects were classified as water or non-water based upon threshold values of the image objects. We employed this automated classification approach that provided initial perimeters of lakes and ponds, which was then supplemented with a semi-automated classification approach where we visually checked the accuracy of the water body perimeter and manually adjusted when needed, e.g. for shadows cast by steep lake banks and potentially flooded lake margins. This allowed for more rapid delineation of lakes and ponds over strict manual interpretation and allowed us to refine the classification and potentially account for differences in timing of imagery acquisition. The classified images were then converted from raster image files to vector files in order to assess changes in lake area and lake abundance for each of the three time slices. Owing to the high spatial resolution of the imagery (1 m) we were able to confidently assess area changes to lakes and ponds with a minimum mapping unit of 0.1 ha for each time slice. The 0.1 ha size was chosen for the cut off as it represented approximately three to five times the size of a typical low-centered ice wedge polygon pond.

Recent remote sensing studies have shown that total precipitation during the year prior to image acquisition may impact measured surface water area of thermokarst lakes [Plug et al., 2008; Jones et al., 2009a]. For our study area and image set, precipitation during the year preceding imagery acquisition for each time slice was fairly similar with 211 mm (1950/51), 227 mm (1978), and 241 mm (2006/07). However, more precipitation in the most recent time slice may be reflected as a net increase in surface

water area. Further, variations in the timing of imagery acquisition relative to break-up and freeze-up within a particular year may impact lake surface area measurements. While all of the imagery was acquired during the summer (SOM Table 1), such seasonal differences may also impact measurements of lake surface area. However, we felt that the comparisons between the three time slices to be relevant due to the steep profile of lake banks along both lowland and upland lake bluffs [West and Plug, 2008; Plug and West, 2009] which would limit the impact of water level fluctuations on the surface area measurements, the imagery resolution and methodology used to delineate water bodies, and the removal of floodplain lakes from the analysis [Smith et al., 2005]. In addition, vegetation growing along lake margins and disproportionate growth rates over time may also impact the ability to delineate shorelines effectively. However, this potential source of error is likely negligible due to the 1 m resolution imagery used in this study and the overall low canopy height in the tundra-dominated study area.

3.4.2 Lake shoreline change

Detailed lake expansion rates were determined with the Digital Shoreline Analysis System (DSAS) extension for ArcGIS© [Thieler et al., 2009]. DSAS generates orthogonal transects at user-defined intervals along a baseline, and calculates the rate of change between two vector files (lake perimeter from time 1 and time 2) based on the elapsed time and the linear distance. DSAS is generally used for coastal change studies; however, it is an appropriate tool for determining change rates with any time series vector file. We used a 5 m buffer of the most recent lake perimeter as the baseline and

orthogonal transects were cast at 50 m intervals around each lake perimeter and change rates were determined from 1950/51 to 1978 and from 1978 to 2006/07.

Error estimates of the linear expansion rate measurements were determined using a modified version of the equation used in determining errors associated with measurement of Arctic coastal erosion rates [Jones et al., 2009b] (1):

$$\text{Error} = \frac{\sqrt{(E_{p1})^2 + (E_{p2})^2 + (RMS_1)^2 + (RMS_2)^2}}{\Delta t} \quad (1)$$

where E_{p1} and E_{p2} represent the pixel resolution of the imagery (all 1 m) from a particular year, RMS_1 and RMS_2 are the root mean square errors associated with georegistration of an image mosaic from a particular year, and Δt is the time interval associated with a given time period. Thus, error associated with the expansion rate measurements were 0.09 m/yr and 0.09 m/yr, during the first (1950/51 to 1978) and second (1978 to 2006/07) time period, respectively.

3.4.3 Climate data analysis

Long-term (1950 to 2007) temperature and precipitation data were available from the climate station located in Kotzebue, Alaska (66.898°, -162.596°). Mean monthly air temperature (T_a) and precipitation (P) data were retrieved from the Alaska Climate Research Center (<http://climate.gi.alaska.edu/>) to assess any variations in climate between the time periods (1950/51 to 1978 and 1978 to 2006/07) used to monitor lake change. These time periods also roughly coincide with a shift in the Pacific Decadal Oscillation from a negative phase to a positive phase in 1976 [Hartmann and Wendler, 2005].

In order to estimate lake water balance, we calculated monthly evaporation (E) using the Blaney-Criddle method [McGuinness and Bordne, 1972] (2):

$$E = p(0.46T_a + 0.75) \quad (2)$$

during the period of open-water duration (June to September), where E is in cm and p is the monthly mean daily percentage of annual daylight hours for 67°N latitude. This empirical method has been compared to the Bowen ratio, energy-budget method for a lake in temperate latitudes and performed reasonably for a model based on T_a and day length [Rosenberry et al., 2007]. Subtracting E from P was used to indicate lake water balance (P-E) from the month of snow accumulation (October) through the summer to September.

Climate data were summarized according to hydro-climatic elements and periods hypothesized to influence inter-annual as well as long-term lake water balance and thermokarst processes. Winter precipitation (October – April) was analyzed as it determines snowmelt runoff, lake recharge, and the potential for overtopping of lake outlets, one aspect of catastrophic lake drainage. Annual water balance (October – September) summed to the late summer period of surface-area observation was analyzed to assess inter-annual variability in water levels and cumulative moisture conditions for both time periods. Finally, mean annual air temperature (MAAT) was analyzed as it relates to both lake and ground temperatures, which play a role in driving and resisting thermal erosion [Burn, 2002]. For each set of hydro-climatic data, we compared linear

regression models for the time periods 1950-1978 and 1978-2007 to evaluate trends and mean conditions that could explain observed lake change patterns.

3.5 Results and discussion

3.5.1 Lake and pond abundance and surface area

The number of thermokarst lakes and ponds larger than 0.1 ha in the 700 km² Cape Espenberg Lowland study area has increased from 666 in 1950/51, to 680 in 1978, to 737 in 2006/07, or a 10.7% increase during the last 57 years. Analysis of the frequency of lakes and ponds based on four size classes (Table 1) shows an increase of 3.4% in the smallest size class (0.1 to 1 ha) between the 1950s and 1978, while an additional increase of 11.9% occurred in this size class between 1978 and 2006/7 (Figure 3). The next smallest size class (1 to 10 ha) also experienced its largest change in the second time period. The 1 to 10 ha size class actually decreased slightly between the first two time slices (-0.9%), however increased 6.8% during the latter time period. The size class ranging from 10 to 40 ha showed an increase of 13.0% between 1950/51 and 1978 and remained stable between 1978 and 2006/07. The largest size class was the only class to consistently show a decreasing trend of 10.0% and 15.3% in the first and second time period, respectively. Thus, it is apparent that there has been a loss of large lakes in the study area and an increase in the number of small lakes and ponds. This increase in the number of small water bodies may be a result of partial drainage of these larger lakes, leaving multiple remnant lakes and ponds, or may result from the formation of new lakes as a result of permafrost degradation.

Of the 14 additional lakes mapped in 1978 relative to the 1950s, six resulted from the formation of new lakes (mean size of 0.12 ha), while the majority resulted from the partial drainage of larger thermokarst lakes and division into remnant water bodies. Similarly, the majority of the 57 additional lakes mapped in the 2006/07 imagery compared to the 1978 imagery were a result of the drainage of larger thermokarst lakes, with 96% representing lakes that resulted from drainage and division of a larger water body. During the latter time period, new thermokarst lake formation accounted for five lakes with a mean size of 0.27 ha. Further, all of these new lakes have formed in drained lake basins. There were a few instances (six) of new water bodies forming in remnant upland topography, however their size was below our minimum mapping unit of 0.1 ha. Thus, between 1950/51 and 2006/07, 85% of the increase in the number of lakes is actually a result of the partial drainage of larger thermokarst lakes.

As shown above, sole analysis of lake abundance without addressing lake area changes over time may be misleading, since lake number may increase as a result of partial lake drainage. Only the combination of analysis of lake surface area changes and lake abundance provides meaningful information for understanding thermokarst lake dynamics. Total lake surface area during 1950/51 was 5,066 ha, during 1978 it was 5,115 ha, and during 2006/07 it was 4,312 ha. Therefore, a total surface area increase of 1.0% occurred between 1950/51 and 1978, which was followed by a decrease of 15.7% between 1978 and 2006/07, resulting in an overall lake surface area reduction of 14.9% between 1950 and 2007. Further, mean lake size for the study area over the period of record has decreased as a result of the increase in small water bodies as well as the loss of

a number of larger lakes, declining from 7.6 ha (1950/51), to 7.5 ha (1978), to 5.9 ha (2006/07).

A number of recent studies have focused on the pattern and rate of change in lakes located in the Arctic and sub-Arctic (Figure 1). Two broad-scale geographic studies indicate that thermokarst lakes in the zone of continuous permafrost are increasing in both number and area, while in the zone of discontinuous permafrost they are decreasing in both number and area [Smith et al., 2005; Riordan et al., 2006]. Other studies have shown that thermokarst lake surface area is tightly coupled with precipitation patterns [Plug et al., 2008; Jones et al., 2009a; Labrecque et al., 2009]. The results from our study area in a relatively warm region of the continuous permafrost zone document a different pattern for thermokarst lake change. We show an increase in the total number of water bodies, yet a decrease in the total area of thermokarst lakes. This pattern can be explained by the formation of several small lakes and ponds following partial drainage. Including water bodies as small as 0.1 ha, we found that total lake number in this study area has increased by 10.7% since the 1950s, yet total lake surface area has decreased by 14.9%. However, if we increase the minimum lake size to 40 ha in order to draw comparisons with changes documented for large lakes in Siberia [Smith et al., 2005], we find that between 1950 and 2007 there has been a reduction in lake number by 24.1% and a reduction in lake area of 26.5%. Therefore, large lakes on the northern Seward Peninsula are draining and are not being replenished by the growth and coalescence of smaller lakes at the same rate. In order to more fully understand these

processes it is important to look further at the high resolution imagery to measure in detail thermokarst lake expansion rates and possible drainage mechanisms.

3.5.2 Thermokarst lake expansion rates

While expansion of thermokarst lakes in the continuous permafrost zone is a known phenomenon, there are very few data on linear expansion rates. Thermokarst lakes are thought to expand due to a number of different shoreline erosional processes, which include: (1) development of thermo-mechanic erosional niches [Tedrow, 1969]; (2) mass wasting through thaw slumps and block failures [Tomirdiaro and Ryabchun, 1973; Kokelj et al., 2009; Plug and West, 2009]; (3) mechanical erosion caused by ice-shove during break-up; and (4) by incorporation of polygonal ponds into the lake [Billings and Peterson, 1980]. In order to determine linear expansion rates and whether they may have changed over time, we analyzed lakes and ponds that continually expanded over our three image time slices within our 700 km² study region using the DSAS tool for two time periods, 1950/51 to 1978 and 1978 to 2006/07 (Figure 4). The number of lakes analyzed by this method was 370 and the water body size ranged from 0.1 ha to 378 ha.

Mean expansion rates for all lakes in the 1950/51 to 1978 time period was 0.34 m/yr, while in the 1978 to 2006/07 time period it was 0.39 m/yr. Owing to errors associated with image coregistration, lake perimeter delineation, and image pixel size (+/- 0.09 m/yr) the small difference in expansion rate between the two time periods is within our measurement uncertainty. Mean expansion rate for an individual lake ranged from a low of 0.02 m/yr to a high of 1.81 m/yr in the 1950/51 to 1978 time period and from a

low of 0.04 m/yr to a high of 1.55 m/yr in the 1978 to 2006/07 time period. Maximum expansion rate for an individual location was 4.25 m/yr and 6.01 m/yr in the first and second time period, respectively.

Analysis of individual lake expansion rates by lake surface area shows a weak, but positive correlation for the early ($r^2=0.30$) and late ($r^2=0.14$) periods and only slight coherence in rates between periods ($r^2=0.17$), suggesting somewhat variable expansion rates over time. However, categorizing expansion rates for lakes based on four distinct size classes (0.1 to 1 ha, 1 to 10 ha, 10 to 40 ha, and 40 to 400 ha) shows interesting results over time and between size classes (Table 1). Lakes in the smaller size class showed the largest discrepancy between the two time periods, with expansion rates increasing from 0.10 m/yr to 0.22 m/yr. Lakes in the middle size class expanded at slightly higher rates than the smallest size class, however the difference between the 1950/51 to 1978 and 1978 to 2006/07 was much smaller, increasing from 0.22 m/yr to 0.28 m/yr. For the two larger size classes, expansion rates were by far the highest. Both size classes showed fairly stable expansion rates (± 0.03 m/yr) however, the largest size class was the only class to show a slight decrease, from 0.62 to 0.59 m/yr. Although smaller lakes have not expanded at the same rate as larger lakes it is interesting that the smaller water bodies exhibited an increase in rates between the time periods, whereas the larger lakes did not. Presumably, these smaller water bodies expand more as a result of thermal erosion since their small surface area and open water extent does not provide adequate fetch for effective wave action and mechanical erosion. Thus, the increased rate

in smaller water bodies in the second time period may be a result of warmer water temperatures relative to the first time period.

In addition to water body size, another potential source of variation in expansion rates relates to the height of a lake margin bluff. Lake margins in the study area can be divided into two distinct categories: lowland and upland bluff types (Figure 5). Of our 7,423 point measurements of thermokarst lake expansion, lowland bluffs accounted for 88% and upland bluffs accounted for 12%. Lowland margins are indicative of expansion into drained thermokarst lake basins and typically have bank heights from 0.5 m to 3.0 m. Upland margins refer to erosional remnants or yedoma-like terrain that have not been modified previously by thermokarst lake processes. Lake bluff heights along such upland margins typically range from 6 m to 17 m. The lowland margin types exhibited fairly consistent expansion rates between the two time periods, 0.37 m/yr and 0.42 m/yr, respectively, while erosion of the upland margin types also showed a similar pattern, increasing slightly from 0.15 m/yr to 0.18 m/yr, respectively, again the slight increase is within our measurement uncertainty. Thus, not surprisingly, it appears that expansion rate is largely driven by the height of the bluff and the composition and state of the material that the thermokarst lake is expanding into, with higher expansion rates along margins at which less sediment material has to be removed. Thus, total variation in the expansion rate of individual lakes may largely be explained by a combination of lake size and bluff height of surrounding lake margin. In addition, bathymetry likely also plays a role in the expansion rate of a bluff section due to warmer water temperatures associated

with deeper lakes and greater disturbance to the ground thermal regime [Arp et al., 2011]; however, we lacked lake depth information to assess this for our dataset.

There is general agreement between thermokarst lake expansion rates from our study area and the limited data available from other thermokarst lake regions (Table 2). In various regions in Alaska, Canada, and Siberia, the long-term, mean expansion rate for thermokarst has been shown to vary between 0.10 and 0.70 m/yr for entire lake margins and upwards of 2.0 to 5.0 m/yr for individual locations along the lake perimeter. Thus, the mean thermokarst lake expansion rate of 0.35 to 0.39 m/yr that we have measured from two different time periods for the northern Seward Peninsula in Alaska falls within the range of expansion rates measured in other Arctic regions. However, all of the previous studies have included only a small number of lakes or provided hypothetical values based on limited data. Thus, our measurement of expansion rates at 7,423 points distributed across 370 lakes in our study region provides the first landscape-scale assessment of this typical process for thermokarst lakes located in the northern, high-latitude continuous permafrost zone.

Further research should be directed towards conducting similar types of landscape analyses in other thermokarst lake-rich regions. The determination of expansion rates is important for developing long-term monitoring programs focused on the use of repeat remote sensing imagery to assess thermokarst lake expansion over time. Thus, for our study area, given a rate between 0.30 and 0.40 m/yr, it would be feasible to acquire high-resolution imagery (1 m) at three to five year increments to document change in rates overtime. Reporting detailed expansion rate estimates is also important for interpreting

and understanding other lake change studies conducted with coarser resolution imagery. For example, widespread thermokarst lake expansion reported over a ~25 year period for Siberia using imagery with a spatial resolution of 150 m [Smith et al., 2005], indicates that expansion rates in their study area would have to have averaged at least 6 m/yr for many lakes over a large area, in order for an increase due to shoreline erosion and permafrost degradation to be detected. Given the results from our analysis and expansion rates reported from other thermokarst lake-rich regions this seems unlikely and other factors controlling lake surface area fluctuation may have also been detected [Plug et al., 2008].

3.5.3 Thermokarst lake drainage

As lakes expand, the chances for drainage increase due to the possibility of encountering a drainage gradient. As pointed out above, the majority of lakes in the study region are expanding, yet the increase in lake abundance can be explained by lake drainage and the division of a larger water body into several smaller water bodies. An analysis of the number of drainage events, defined as a >25% reduction in surface area [Hinkel et al., 2007], reveals that 130 lakes drained between 1950/51 and 2006/07, which has resulted in an average drainage rate of 2.3 lakes/yr. Analyzing the lake drainage events further, reveals that the thermokarst lake drainage rate has remained fairly stable over the last half-century, with a drainage rate of 2.2 lakes/yr between 1950/51 and 1978, and 2.3 lakes/yr between 1978 to 2006/07. However, in the second period there was an increase in the drainage rate of larger lakes, accounting for the drastic reduction in thermokarst lake surface area on the landscape (Table 1).

Hinkel et al., [2007] analyzed lakes larger than 10 ha for a portion of northern Alaska (34,000 km²) and found that 50 lakes drained (> 25% reduction in surface area) between ca. 1975 and ca. 2000, for a drainage rate of ~2 lakes/yr. Catastrophic lake drainage events have also been reported for a 5,000 km² area on the Tuktoyaktuk Peninsula, Canada. Mackay [1988] found that between 1950 and 1986 roughly 65 lakes had drained completely or partially, yielding a drainage rate of ~1.8 lakes/yr. More recently, Marsh et al. [2009] provide estimates of lake drainage events from the same region by looking at three time periods, 1950 to 1973, 1973 to 1985, and 1985 to 2000. Their results indicate a reduction in the drainage rate of thermokarst lakes in the region, from 1.13 to 0.93 to 0.33 lakes/yr in each time period, respectively. Thus, drainage rates for thermokarst lakes for our 700 km² study area on the northern Seward Peninsula are slightly higher, yet fairly similar to those documented for other regions in northern Alaska and NW Canada. However, if these drainage rates held up across the entirety of the northern Seward Peninsula it is likely that this region would exhibit the highest thermokarst lake drainage rates thus far found in the Arctic.

Drainage of thermokarst lakes can be divided into two distinct categories, lateral and internal, both of which relate to degradation of confining permafrost. Lateral thermokarst lake drainage has been reported from a number of regions in the circum-Arctic. Typical mechanisms thought to lead to the lateral drainage of thermokarst lakes in the zone of continuous permafrost are bank overflow, ice-wedge degradation and development of a drainage network, headward stream erosion, lake tapping, coastal erosion, as well as expansion of a lake towards a drainage gradient [Hopkins, 1949;

Mackay, 1988; Brewer et al., 1993; Hinkel et al., 2007; Marsh et al., 2009; Grosse et al., 2013]. In contrast, internal drainage of thermokarst lakes has been documented in discontinuous permafrost regions in instances where the talik or thawed zone beneath a lake penetrates the permafrost, allowing for drainage subterraneously [Hopkins, 1949; Yoshikawa and Hinzman, 2003]. Thus, it is important to try to determine the causal mechanism for lake drainage in a particular region to better understand the processes driving observed lake change. In the case of lateral lake drainage events, this can be accomplished with the use of high-resolution remotely sensed imagery because drainage channels can be visualized whereby in coarser resolution imagery they largely are not detectable because of their often small width.

Through analysis of the high spatial resolution imagery we classified the causal mechanism of a particular lake drainage event. Based on the total number of drainage events between 1950/51 and 2006/07, the majority of lake drainage events (71%) appear to be a result of lake expansion into a low lying area, such as an adjacent lake, a stream corridor, the coast, or topographic gradient (Figure 6). This class was determined through visible evidence of lake expansion and development of a drainage channel (Figure 7). Analysis of those lakes draining during the 1978 to 2006/07 time period showed that nearly all lakes expanded at a rate (0.42 m/yr), from 1950/51 to 1978, roughly equal to that of the mean for the entire study area (0.35 m/yr). However, without elevation data over the entirety of our study region other mechanisms cannot definitively be ruled out. The second most important mechanism appeared to be related to bank overtopping or possibly ice-wedge degradation (17%). This inference was based upon no

noticeable bluff erosion and lake expansion, however development of a distinct drainage channel. Further, it is likely that lake expansion and bank overtopping or ice-wedge degradation can occur in concert with one another at a given lake and also in areas where lake drainage clustering may have occurred due to expansion of one lake and subsequent drainage and flooding of a nearby lake, ultimately forcing it to overtop its bank. Thermokarst lake expansion into adjacent ice-rich permafrost also leads to incorporation of ground-ice melt water into the lake, which may also factor into bank overtopping. However, only excess ice that is situated above the lake water level can be counted for this additional water into the lake since melting excess ice below the lake water level may have an opposite effect due to the fact that produced water volume is smaller than original ice volume. Migration of river channels and subsequent lake tapping was likely responsible for the drainage of two lakes. For thirteen of the lakes that decreased in area over the study period no drainage outlet was visible in the high-resolution imagery, possibly indicating that these lakes shrunk as a result of drying rather than drainage. It is possible that these drained internally, however, they were all very small (mean area of 0.20 ha) and permafrost in this region may be up to 100 m thick. Thus, through the analysis of high-resolution imagery we have determined that the vast majority of lake drainage events in our study area result from lateral drainage and surface permafrost degradation.

Hinkel et al. [2007] also tried to infer the causal mechanism for lake drainage events in northern Alaska and found that 38% resulted from lake expansion, 16% from stream meandering, 26% by headward erosion of a stream, and 2% through coastal

erosion. For 18% it remained unclear as to how the lakes drained. Thus, with the exception of lakes draining via coastal erosion and positively identifying headward erosion (instead we consider bank overtopping or ice-wedge degradation and development of a drainage channel), the relative pattern is similar. Further, the authors also reported a number of cases where human disturbance caused the drainage of lakes near Barrow, Alaska [Hinkel et al., 2007]. For our study, we are unaware of the impact of humans on the drainage of lakes in this region.

3.5.4 Climate data observations from 1950 to 2007

Analysis of climate data from Kotzebue, Alaska, located 60 miles to the northwest of the study region, showed distinct differences in climatology between lake change observation periods. The earlier period (1950-1978) was characterized by low and stable winter precipitation of 6.8 cm (Figure 8a), decreasing P-E of 0.4 cm/yr ($r^2=0.18$) (Figure 8b), and a MAAT of -6.3°C (Figure 8c). The latter period (1978-2007) was characterized by increasing winter precipitation 0.1 cm/yr ($r^2=0.10$) (Figure 8a), a fairly stable yet slightly wetter annual water balance (Figure 8b), and a slightly warmer MAAT of -5.0°C (Figure 8c). The step-change observed between these periods is consistent with a shift in the Pacific Decadal Oscillation from a negative to positive phase in 1976 [Hartman and Wendler, 2005].

Thus, it is somewhat surprising that the expansion rate and drainage rate of thermokarst lakes in the study area has remained fairly constant over the last ~60 years. However, the slight increase in expansion rate as well as drainage rate, although within measurement uncertainty, may reflect these shifts in climate. The possibility also exists,

that the Kotzebue climate station data does not directly represent climatic conditions in our study region. Despite the close proximity, Kotzebue is located on a narrow isthmus of land that juts into the ocean. Future research and field studies should be directed towards gaining a better understanding of the factors controlling lake expansion and lake drainage as an accurate assessment of the causal mechanisms are critical for understanding how thermokarst lakes may respond to climate change.

3.5.5 Thermokarst lake and carbon cycle dynamics

As demonstrated above, thermokarst lake expansion and drainage is an active landscape change mechanism operating on the northern Seward Peninsula. Thermokarst lakes have expanded at a mean rate of 0.35 to 0.39 m/yr since the 1950s. However, as lakes expand the possibility of drainage increases due to the encroachment towards a topographic gradient. For our study area, the lateral expansion of lakes has resulted in their lateral drainage through surface permafrost degradation at a rate of roughly 2.3 lakes/yr. In a simple analysis of the landscape that has been impacted by these two mechanisms we determined land lost through time as a result of thermokarst lake expansion and land gained through time as a result of thermokarst lake drainage (Figure 9). This indicates that during the first time period (1950/51 to 1978) the landscape was in near equilibrium, losing approximately 390 ha and gaining 340 ha of land area. However, due to the drainage of several large lakes in the second time period (1978 to 2006/07), land area gained (1200 ha) was nearly four times the area lost (410 ha) due to thermokarst lake expansion.

Several studies have documented landscape scale controls on the emission of greenhouse gases from northern high-latitude regions [Bartlett et al., 1992; Christensen et al., 2007; Flessa et al., 2008; Schneider et al., 2009]. In general, the importance of Arctic and sub-Arctic freshwater systems as a net emitter has been noted for some time [Coyne and Kelley, 1974; Kling et al., 1991; Cole et al., 1994; Phelps et al., 1998]. More recently, Walter et al. [2006] highlighted the potential importance of northern high-latitude thermokarst lake methane fluxes on the global atmospheric carbon budget. However, high lake methane fluxes are linked to a specific type of thermokarst lake that has formed in thick ice-rich and organic-rich sediments (yedoma or yedoma-like permafrost), whereas thermokarst lakes in basin-rich lowlands largely occupy fully or partially the basins of previous lake generations filled with lacustrine sediments already depleted in labile carbon, resulting in lower CH₄ emissions during subsequent lake generations [Walter Anthony et al., this volume]. Drainage of such low-emitting later generation thermokarst lakes and the formation of wetlands in the basin could, despite carbon accumulation in peat, result in a short-term increase in CH₄ emissions.

In the case of carbon dioxide fluxes from thermokarst lake and basin-rich lowland Arctic landscapes, Zona et al. [2010] noted that the formation and drainage of thermokarst lakes factor in prominently to net CO₂ emissions at the landscape scale, with increased emissions in recently drained basins and progressively decreasing emissions as a drained basin ages and less productive plant species colonize. However, once vegetated, all basins served as a CO₂ sink. Similarly, for a shrinking thermokarst lake in central Alaska, Wickland et al. [2009] found that within the first 15 years of drainage the

freshly exposed lake sediments acted as a CO₂ source. However, 30 years post-drainage, as a result of a decrease in labile compounds and establishment of terrestrial vegetation in the basin, CO₂ emissions were reduced to the point where the basin acted as a net C sink [Wickland et al., 2009].

Bastviken et al. [2011] recently found that globally, freshwater methane emissions act to offset the net continental or terrestrial carbon sink. Thus, if lakes on the landscape are draining as a result of surface permafrost degradation and the basins left behind begin to sequester carbon in the form of peat, lake drainage may serve as a negative feedback to global warming. However, in our study area, the net C budget for each lake/basin system is dependent on a complex set of thermokarst lake characteristics, lake history, substrate and organic carbon quality, environmental and climate conditions, and subsequent drainage and wetland characteristics complicating extrapolation of the role of expanding and draining lakes on the landscape.

Since thermokarst lake dynamics likely factor into landscape-scale carbon fluxes, we must gain a better understanding of the short-term and long-term C dynamics of these systems and regions [Frolking and Roulet, 2007] and incorporate these fluxes into terrestrial greenhouse gas emission scenarios. The balance between expanding lakes and draining lakes on the landscape is important for up-scaling carbon emission and sequestration estimates over short- as well as long-time scales [Hinkel et al., 2003; Zona et al., 2010; Jones et al., 2012]. Thus, further research is needed to more fully understand the role of thermokarst lake dynamics at the landscape-scale and how these prominent lowland Arctic landscapes factor in the northern, high-latitude carbon cycle.

3.6 Conclusion

Thermokarst lakes are a dynamic component of lowland Arctic landscapes with ice-rich permafrost. Our assessment of lakes and ponds >0.1 ha in a 700 km² area using high resolution remotely sensed imagery from 1950/51, 1978, and 2006/07 revealed that the majority of thermokarst lakes are actively expanding as a result of surface permafrost degradation. However, as lakes expand the opportunity for drainage increases due to the encroachment towards a drainage gradient. Thus, total surface area of lakes in the study region declined by 15% due to the lateral drainage of several large lakes. Long-term mean expansion rates of thermokarst lakes in the region ranged from 0.35 m/yr and 0.39 m/yr and long-term lake drainage rates from 2.2 lakes/yr to 2.3 lakes/yr in the first (1950/51 to 1978) and second (1978 to 2006/07) observation periods, respectively. Analysis of climate data over the 57 year study period did not reveal any definitive link in regards to the response of thermokarst lakes to climatic forcing. However, given future climate projections, it is likely that thermokarst lake-rich Arctic lowlands will change dynamically as a result of surface permafrost degradation. In turn, this will likely impact the northern high-latitude carbon budget.

3.7 Acknowledgements

This study was supported by NASA grant NNX08AJ37G and NSF IPY grant #0732735. Any opinions, findings, conclusions, or recommendations expressed in this material are those of the authors and do not necessarily represent the views of the National Science Foundation or NASA. Any use of trade, product, or firm names is for descriptive purposes only and does not imply endorsement by the U.S. Government. We thank the

National Park Service Fairbanks Office for providing high-resolution satellite imagery of parklands and permits to do fieldwork in the Bering Land Bridge National Preserve. We also thank the GAM and LRS programs of the USGS for additional support. This manuscript benefited from the reviews of Karen Murphy, Amy Larsen, and one anonymous reviewer.

3.8 References

Arp, C. D., and B. M. Jones (2009), Geography of Alaska Lake Districts: Identification, description, and analysis of lake-rich regions of a diverse and dynamic state, *U.S. Geol. Surv. Sci. Invest. Rep. 2008-5215*.

Arp, C. D., B. M. Jones, F. E. Urban, and G. Grosse (2011), Hydrogeomorphic processes of thermokarst lakes with grounded-ice and floating-ice regimes on the Arctic coastal plain, Alaska, USA, *Hydrological Processes*, 25, 2422-2438, doi:10.1002/hyp.8019.

Bartlett, K. B., P. M. Crill, R. L. Sass, R. C. Harriss, and N. B. Dise (1992), Methane emissions from tundra environments in the Yukon-Kuskokwim Delta, Alaska, *Journal of Geophysical Research*, 97(D15), 16,645–16,660, doi:10.1029/91JD00610.

Bastviken, D., L. J. Tranvik, J. A. Downing, P. M. Crill, and A. Enrich-Prast (2011), Freshwater methane emissions offset the continental carbon sink, *Science*, 331, 50.

Beget, J., D. M. Hopkins, and S. D. Charron (1996), The largest known maars on earth, Seward Peninsula, northwest Alaska, *Arctic*, 49, 62-69.

Billings, W. D., and K. M. Peterson (1980), Vegetational change and ice-wedge polygons through the thaw-lake cycle in Arctic Alaska, *Arctic and Alpine Research*, 12, 413-432.

Brewer M. C., L. D. Carter, R. Glenn, and D. F. Murray (1993), Sudden Drainage of A Thaw Lake on the Alaskan Arctic Coastal Plain, Proceedings of the 6th International Conference on Permafrost, Beijing, 48-53.

Burn, C. R. (2002), Tundra lakes and permafrost, Richards Island, western Arctic coast, Canada. *Canadian Journal of Earth Sciences*, 39, 1281-1298.

Charron, S. D. (1995), Surficial mapping of the Cape Espenberg-Devil Mountain Region and lake core analyses from North Killeak Lake, Bering Land Bridge National Preserve, Western Alaska, Unpublished Masters thesis, University of Massachusetts.

Christensen, T. R., T. Johansson, M. Olsrud, L. Strom, A. Lindroth, M. Mastepanov, N. Malmer, T. Friborg, P. Crill, and T. V. Callaghan (2007), A catchment-scale carbon and greenhouse gas budget of a subarctic landscape, *Phil. Trans. Royal Society A*, 365, 1643-1656.

Cole, J. J., N. F. Caraco, G. W. Kling, and T. K. Kratz (1994), Carbon dioxide supersaturation in the surface waters of lakes, *Science*, 265, 1568-1570.

Coyne, P. I., and J. J. Kelley (1974), Carbon dioxide partial pressures in Arctic surface waters, *Limnology and Oceanography*, 19, 928-938.

Flessa, H., A. Rodionov, G. Guggenberger, H. Fuchss, P. Magdons, O. Shibistove, G. Zrazhevskaya, N. Mikheyeva, O.A. Kasansky, and C. Blodau (2008), Landscape controls of CH₄ fluxes in a catchment of the forest tundra ecotone in northern Siberia, *Global Change Biology*, 14, 2040-2056.

Frohn, R. C., K. M. Hinkel, and W. R. Eisner (2005), Satellite remote sensing classification of thaw lakes and drained thaw lake basins on the North Slope of Alaska, *Remote Sensing of Environment*, 97, 116-126.

Frolking, S. and N. T. Roulet (2007), Holocene radiative forcing impacts of northern peatland carbon accumulation and methane emissions, *Global Change Biology*, 13, 1079-1088.

Grosse, G., L. Schirrmeister, and T. J. Malthus (2006), Application of Landsat-7 satellite data and a DEM for the quantification of thermokarst-affected terrain types in the periglacial Lena-Anabar coastal lowland, *Polar Research*, 25, 51-67.

Grosse, G., B. M. Jones, and C. D. Arp (2013), Thermokarst lakes, drainage, and drained basins, In: Editor-in-Chief: John F. Shroder, *Treatise on Geomorphology*, Academic Press, San Diego, 325-353, ISBN 9780080885223, doi: 10.1016/B978-0-12-374739-6.00216-5.

Harry, D. G. and H. M. French (1983), The orientation and evolution of thaw lakes, southwest Banks Island, Canadian Arctic. In "Fourth International Conference on Permafrost." (T. L. Pewe, and J. Brown, Eds.). National Academy Press, Fairbanks, Alaska.

Hartmann, B., and G. Wendler (2005), The significance of the 1976 Pacific climate shift in the climatology of Alaska, *Journal of Climate*, 18, 4824-4839.

Hinkel, K. M., W. R. Eisner, J. G. Bockheim, F. E. Nelson, K. M. Peterson, and X. Dai (2003), Spatial extent, age, and carbon stocks in drained thaw lake basins on the Barrow Peninsula, Alaska, *Arctic, Antarctic and Alpine Research*, 35, 291-300.

Hinkel, K. M., R. C. Frohn, F. E. Nelson, W. R. Eisner, and R. A. Beck (2005), Morphometric and Spatial Analysis of Thaw Lakes and Drained Thaw Lake Basins in the Western Arctic Coastal Plain, Alaska, *Permafrost & Periglacial Processes*, 16, 327-341.

Hinkel, K. M., B. M. Jones, W. R. Eisner, C. J. Cuomo, R. A. Beck, and R. C. Frohn, (2007), Methods to assess natural and anthropogenic thaw lake drainage on the western Arctic coastal plain of northern Alaska, *J. Geophys. Res.*, 112, F02S16.

Hopkins, D. M. (1949), Thaw lakes and thaw sinks in the Imuruk Lake area, Seward Peninsula, Alaska, *Journal of Geology*, 57, 119-131.

Hopkins, D. M., T. N. V. Karlstrom, R. Black, T. L. Pewe, A. T. Fernold, and E. H. Muller (1955), Permafrost and Ground Water in Alaska, *U. S. Geol. Surv. Prof. Pap.*, 264, 70 pp.

Höfle, C., M. E., Edwards, D. M. Hopkins, D. H. Mann, and C. L. Ping (2000), The full-glacial environment of the northern Seward Peninsula, Alaska, reconstructed from the 21,500 year old Kitluk paleosol, *Quaternary Research*, 53, 143-153.

Hopkins, D. M. (ed.) (1967), *The Bering Land Bridge*, Stanford Univ. Press, Stanford.

Jones, B. M., C. D., Arp, K. M. Hinkel, R. A. Beck, J. A. Schmutz, and B. Winston (2009a), Arctic lake physical processes and regimes with implications for winter water availability and management in the National Petroleum Reserve Alaska, *Environmental Management*, 43(6), 1071-1084.

Jones, B. M., C. D. Arp, M. T. Jorgenson, K. M. Hinkel, J. A. Schmutz, and P. L. Flint (2009b), Increase in the rate and uniformity of coastline erosion in Arctic Alaska, *Geophysical Research Letters*, 36, L03503, doi:10.1029/2008GL036205.

Jones, M. C., G. Grosse, B. M. Jones, and K. M. Walter Anthony (2012), Peat accumulation in drained thermokarst lake basins in continuous, ice-rich permafrost, northern Seward Peninsula, Alaska, *Journal of Geophysical Research*, 117, G00M07, doi:10.1029/2011JG001766.

Jorgenson, M. T., and T. Osterkamp (2005), Response of boreal ecosystems to varying modes of permafrost degradation, *Canadian Journal of Forestry Research*, 35, 2100-2111.

Jorgenson, M. T., and Y. Shur (2007), Evolution of lakes and basins in northern Alaska and discussion of the thaw lake cycle. *J. Geophys. Res.*, 112, doi:10.1029/2006JF000531.

Klein, E., E. E. Berg, and R. Dial (2005), Wetland drying and succession across the Kenai Peninsula Lowlands, south-central Alaska, *Canadian Journal of Forest Research*, 35, 1931-1941.

Kling, G. W., G. W. Kipphut, and M. C. Miller (1991), The flux of CO₂ and CH₄ from lakes and rivers in arctic Alaska, *Hydrobiologia*, 240, 23-36.

Kokelj, S. V., T. C. Lantz, J. Kanigan, S. L. Smith, and R. Coutts (2009), Origin and polycyclic behavior of tundra thaw slumps, Mackenzie Delta Region, Northwest Territories, Canada, *Permafrost & Periglacial Processes*, 20, 173-184.

Labrecque, S., D. Lacelle, C. R. Duguay, B. Lauriol, and J. Hawkings (2009), Contemporary (1951-2001) evolution of lakes in the Old Crow Basin, Northern Yukon, Canada: remote sensing, numerical modeling, and stable isotope analysis, *Arctic*, 62(2), 225-238.

Mackay, J. R. (1988), Catastrophic lake drainage, Tuktoyaktuk Peninsula area, District of Mackenzie, *Current Research, Part D, Geological Survey of Canada, Paper 88-1D*, 83-90.

Manley W. F., E. G. Parrish, D. M. Sanzone, and L. R. Lestak (2007a), High-Resolution Orthorectified Imagery from Approximately 1950 for the Coastal Areas of Bering Land Bridge NP (BELA) and Cape Krusenstern NM (CAKR), Northwest Alaska: Fairbanks, AK: National Park Service, Arctic Network I&M Program. Digital Media.

Manley W. F., E. G. Parrish, D. M. Sanzone, and L. R. Lestak (2007b), High-Resolution Orthorectified Imagery from Approximately 1980 for the Coastal Areas of Bering Land Bridge NP (BELA) and Cape Krusenstern NM (CAKR), Northwest Alaska: Fairbanks, AK: National Park Service, Arctic Network I&M Program. Digital Media.

Manley W. F., E. G. Parrish, D. M. Sanzone, and L. R. Lestak (2007c), High-Resolution Orthorectified Imagery from 2003 for the Coastal Areas of Bering Land Bridge NP (BELA) and Cape Krusenstern NM (CAKR), Northwest Alaska: Fairbanks, AK: National Park Service, Arctic Network I&M Program. Digital Media.

Marsh, P., M. Russell, S. Pohl, H. Haywood, and C. Onclin (2009), Changes in thaw lake drainage in the Western Canadian Arctic from 1950 to 2000, *Hydrological Processes*, 23, 145-158.

Phelps, A. R., K. M. Peterson, and M. O. Jeffries (1998), Methane efflux from high-latitude lakes during spring ice melt, *Journal of Geophysical Research*, *103* (D22), 29,029–29,036, doi:10.1029/98JD00044.

Plug, L. J., C. Walls, and B. M. Scott (2008), Tundra lake changes from 1978 to 2001 on the Tuktoyaktuk Peninsula, western Canadian Arctic, *Geophysical Research Letters*, *35*(3), L03502.

Plug, L. J. and J. J. West (2009), Thaw lake expansion in a two-dimensional coupled model of heat transfer, thaw subsidence, and mass movement, *Journal of Geophysical Research*, *114*, F01002.

Rampton, V. M. (1988), Quaternary Geology of the Tuktoyaktuk Coastlands, Northwest Territories, *Geological Survey of Canada memoir 423*, 98 pp.

Riordan, B., D. Verbyla, and A. D. McGuire (2006), Shrinking ponds in subarctic Alaska based on 1950–2002 remotely sensed images, *Journal of Geophysical Research*, *111*, G04002.

Romanovskii, N. N., H.-W. Hubberten, A. V. Gavrilov, V. E. Tumskoy, and A. Kholodov (2004), Permafrost of the east Siberian Arctic shelf and coastal lowlands, *Quaternary Science Reviews*, *23*, 1359-1369.

Rosenberry, D. O., T. C. Winter, D. C. Buso, and G. E. Likens (2007), Comparison of 15 evaporation methods applied to a small mountain lake in the northeastern USA, *Journal of Hydrology*, *340*, 149-166.

Schneider, J., G. Grosse, and D. Wagner (2009), Land cover classification of tundra environments in the Arctic Lena Delta based on Landsat 7 ETM+ data and its application for upscaling of methane emissions, *Remote Sensing of Environment*, *113*, 380-391.

Sellmann, P. V., J. Brown, R. I. Lewellen, H. L. McKim, and C. J. Merry (1975), The classification and geomorphic implications of thaw lakes on the Arctic Coastal Plain, Alaska, U.S. Army Cold Regions Research and Engineering Laboratory, Hanover, New Hampshire, 21 pp.

Sheng, Y., C. A. Shah, and L. C. Smith (2008), Automated Image Registration for Hydrologic Change Detection in the Lake-Rich Arctic, *IEEE Geoscience and Remote Sensing Letters*, *5*(3), 414-418.

Smith, L. C., Y. Sheng, G. M. MacDonald, and L. D. Hinzman (2005), Disappearing Arctic Lakes, *Science*, *308*, 1429.

Smith, L. C., Y. Sheng, and G. M. MacDonald (2007), A first pan-Arctic assessment of the influence of glaciation, permafrost, topography and peatlands on northern hemisphere lake distribution, *Permafrost & Periglacial Processes*, 18, 201-208.

Smith S. L., V. E. Romanovsky, A. G. Lewkowicz, C. R. Burn, M. Allard, G. D. Clow, K. Yoshikawa, and J. Throop (2010), Thermal state of permafrost in North America: a contribution to the International Polar Year. *Permafrost and Periglacial Processes*, 21, 117–135. DOI: 10.1002/ppp.690.

Tedrow, J. C. F. (1969), Thaw lakes, thaw sinks and soils in northern Alaska, *Biuletyn Peryglacjalny*, 20, 337-345.

Thieler, E. R., E. A. Himmelstoss, J. L. Zichichi, and A. Ergul (2009), Digital Shoreline Analysis System (DSAS) version 4.0—An ArcGIS extension for calculating shoreline change, *U.S. Geological Survey Open-File Report 2008-1278*.

Tomirdiaro, S. V., and V. K. Ryabchun (1973), Lake thermokarst on the Lower Anadyr Lowland. In: *Permafrost: USSR Contribution to the Second International Conference*, Yaktusk, USSR. Washington, DC, National Academy of Science, pp. 94-100.

van Everdingen, Robert, ed. 1998 revised May 2005, Multi-language glossary of permafrost and related ground-ice terms, Boulder, CO: National Snow and Ice Data Center/World Data Center for Glaciology.

Walter, K. M., S. A. Zimov, J. P. Chanton, D. Verbyla, and F. S. Chapin, III (2006), Methane bubbling from Siberian thaw lakes as a positive feedback to climate warming, *Nature*, 443, 71–75.

Walter, K. M., M. E. Edwards, G. Grosse, S. A. Zimov, and F. S. Chapin III (2007), Thermokarst lakes as a source of atmospheric CH₄ during the last deglaciation, *Science*, 318, 633–636, doi:10.1126/science.1142924.

West, J. J., and L. J. Plug (2008), Time-dependent morphology of thaw lakes and taliks in deep and shallow ground ice, *Journal of Geophysical Research*, 113, F01009.

Wickland, K., J. A. O'Donnell, J. C. Koch, M. T. Jorgenson, J. W. Harden, R. G. Striegl, and L. Anderson (2009), Fate of carbon in sediments of a drying high latitude lake, Interior Alaska, *Eos Trans. AGU*, 90(52), Fall Meet. Suppl., Abstract U41C-0057.

Yoshikawa, K. and L. D. Hinzman (2003), Shrinking thermokarst ponds and groundwater dynamics in discontinuous permafrost near Council, Alaska, *Permafrost & Periglacial Processes*, 14, 151-160.

Zimov, S. A., Y. V. Voropaev, I. P. Semiletov, S. P. Davidov, S. F. Prosiannikov, F. S. Chapin III, M. C. Chapin, S. Trumbore, and S. Tyler (1997), North Siberian Lakes: A Methane Source Fueled by Pleistocene Carbon, *Science*, 277, 800-802.

Zona, D., W. C. Oechel, K. M. Peterson, R. J. Clements, K. T. Paw, and S. L. Ustin (2010), Characterization of the carbon fluxes of a vegetated drained lake basin chronosequence on the Alaskan Arctic Coastal Plain, *Glob. Change Biol.*, 16, 1870-1882, doi:10.1111/j.1365-2486.2009.02107.

3.9 Figures

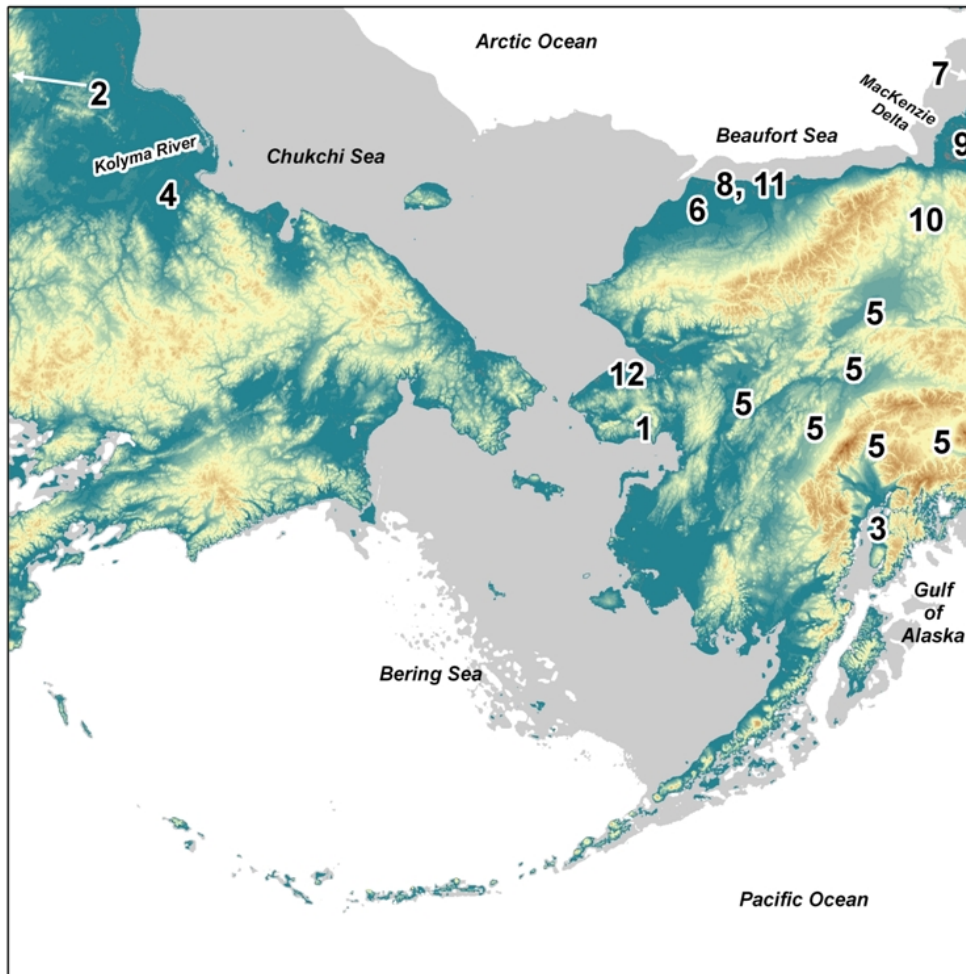


Figure 1: Arctic and Sub-Arctic lake change detection studies. Digital elevation model base map showing the location of Arctic and sub-Arctic lake change detection studies: (1) Yoshikawa and Hinzman, 2003, (2) Smith et al., 2005, (3) Klein et al., 2005, (4) Walter et al., 2006, (5) Riordan et al., 2006, (6) Hinkel et al., 2007, (7) Plug et al., 2008, (8) Jones et al., 2009a, (9) Marsh et al., 2009, (10) Labrecque et al., 2009, (11) Arp et al., 2011 (12) Jones et al., this study. Exposed portions of the continental shelf during the last glacial maximum are shown in gray.

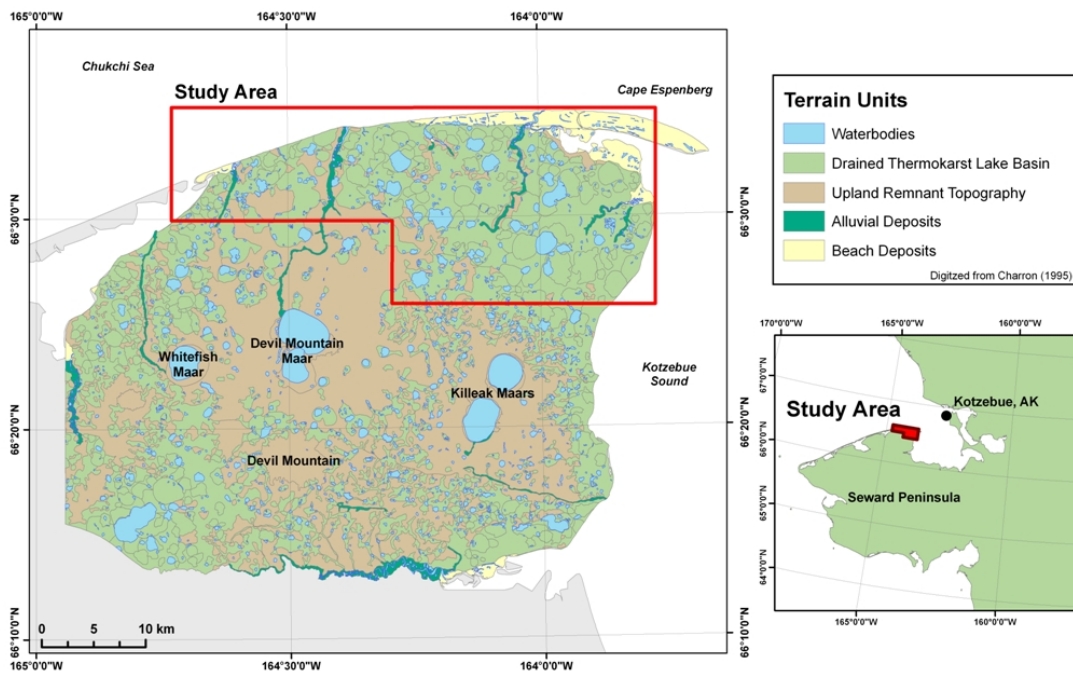


Figure 2: Cape Espenberg Lowlands study area. Terrain unit map of the Cape Espenberg Lowland - Devil Mountain region (digitized from Charron, [1995]). The 700 km² study area is outlined in red and the location of Kotzebue relative to our study area is shown in the inset.

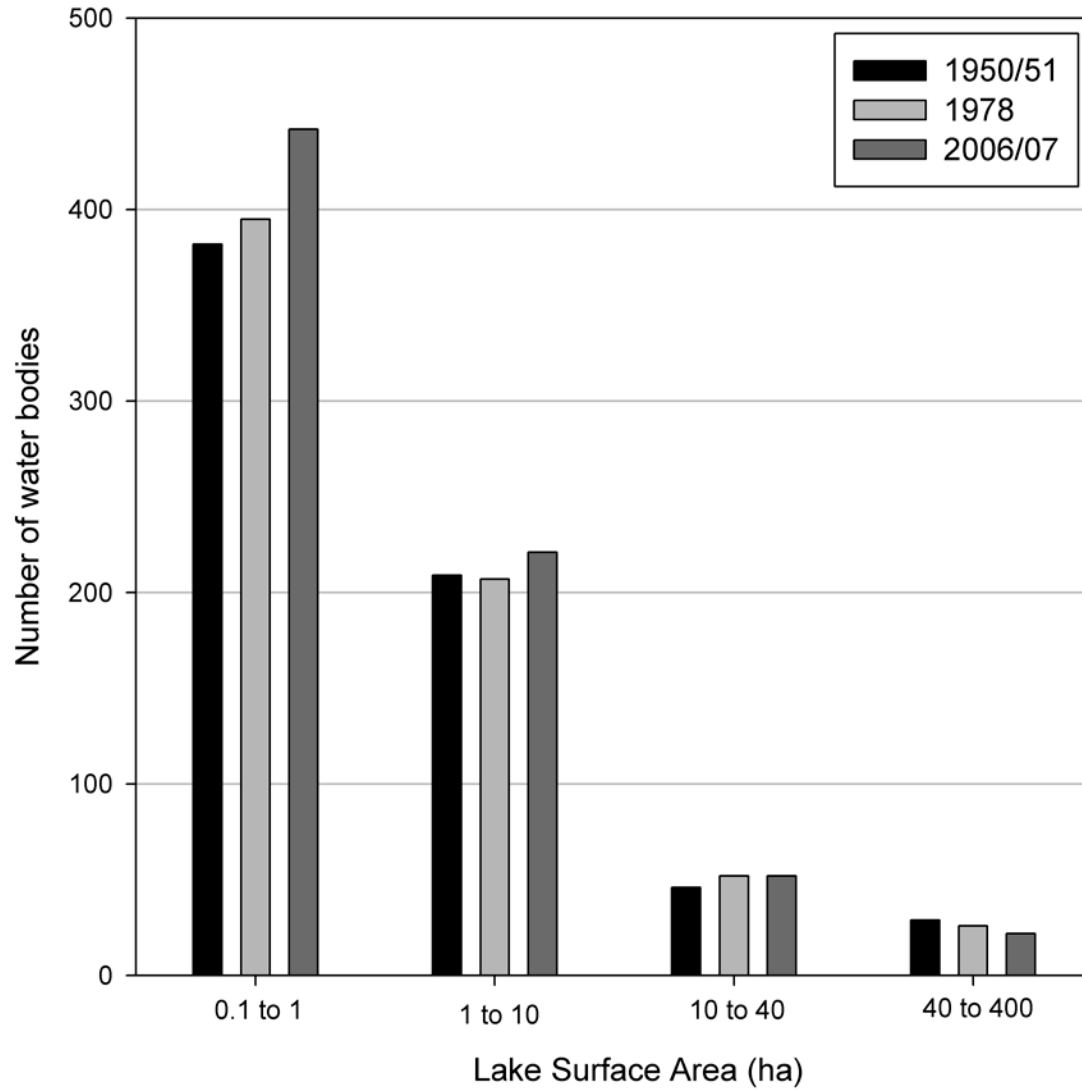


Figure 3: Number of water bodies in various size classes. Comparison of the number of water bodies in four size classes in 1950/51, 1978, and 2006/07. The increase in smaller water bodies can largely be attributed to the partial drainage of larger water bodies.

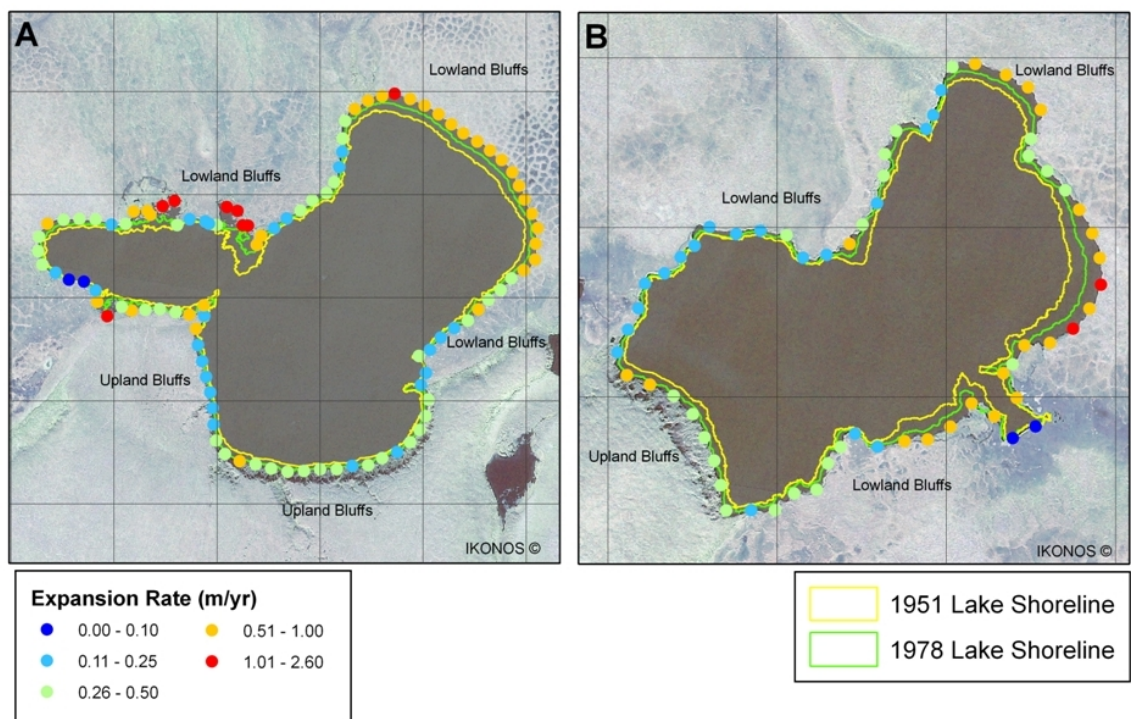


Figure 4: Thermokarst lake expansion rate measurements. Example of expansion rate measurements at two lakes in the study area. Rates determined with the DSAS tool [Thieler et al., 2009] at 50 m increments around the perimeter of the lake. (A) Lake Rhonda expanded at a mean rate of 0.53 m/yr and (B) Lake Luna expanded at a mean rate of 0.44 m/yr over the observation period. The 1951 lake shoreline is shown as a yellow polygon, the 1978 lake shoreline as a green polygon, and the background image is from 2006. The 100 m grid in each frame shows the scale.

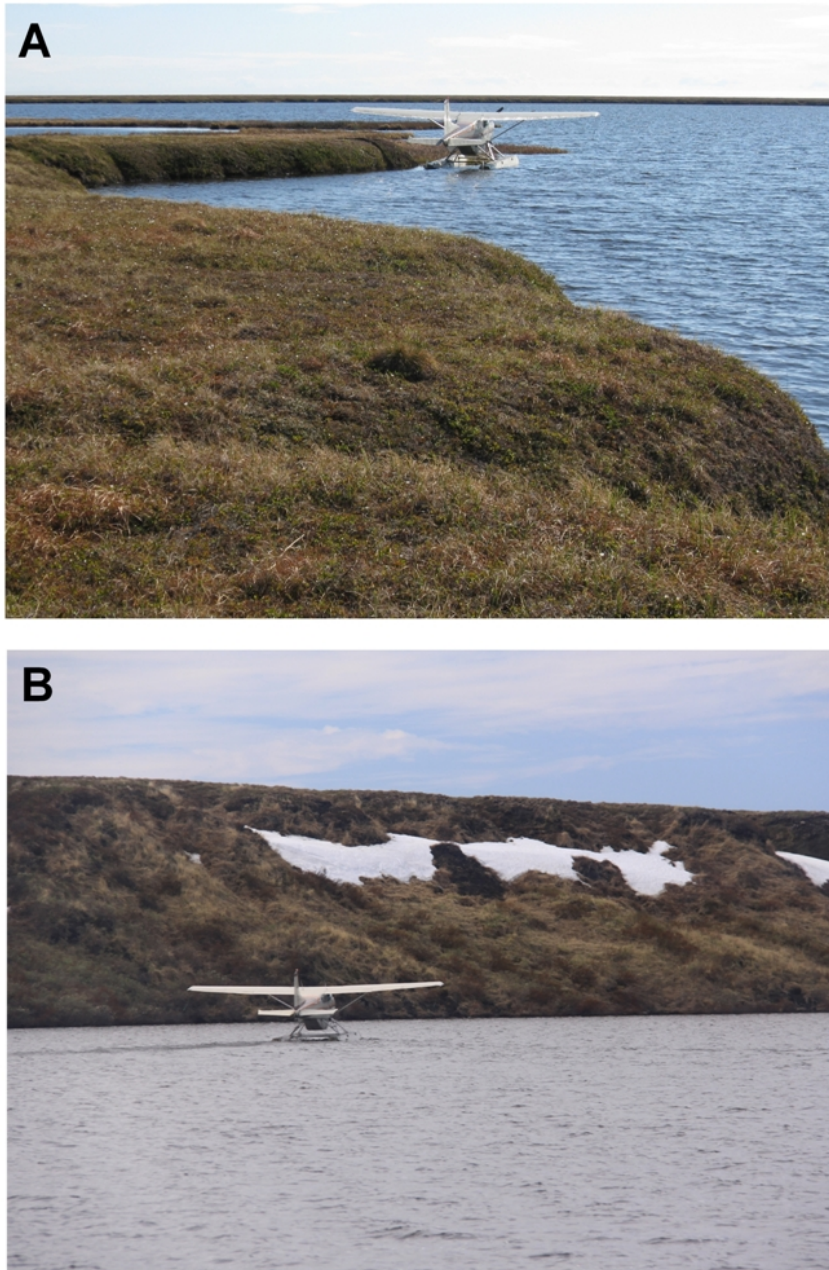


Figure 5: Field photographs showing differences in bluff types. (A) Photo showing a typical lowland bluff and (B) and a typical upland bluff. A Cessna 185 floatplane in each photo provides a scale.

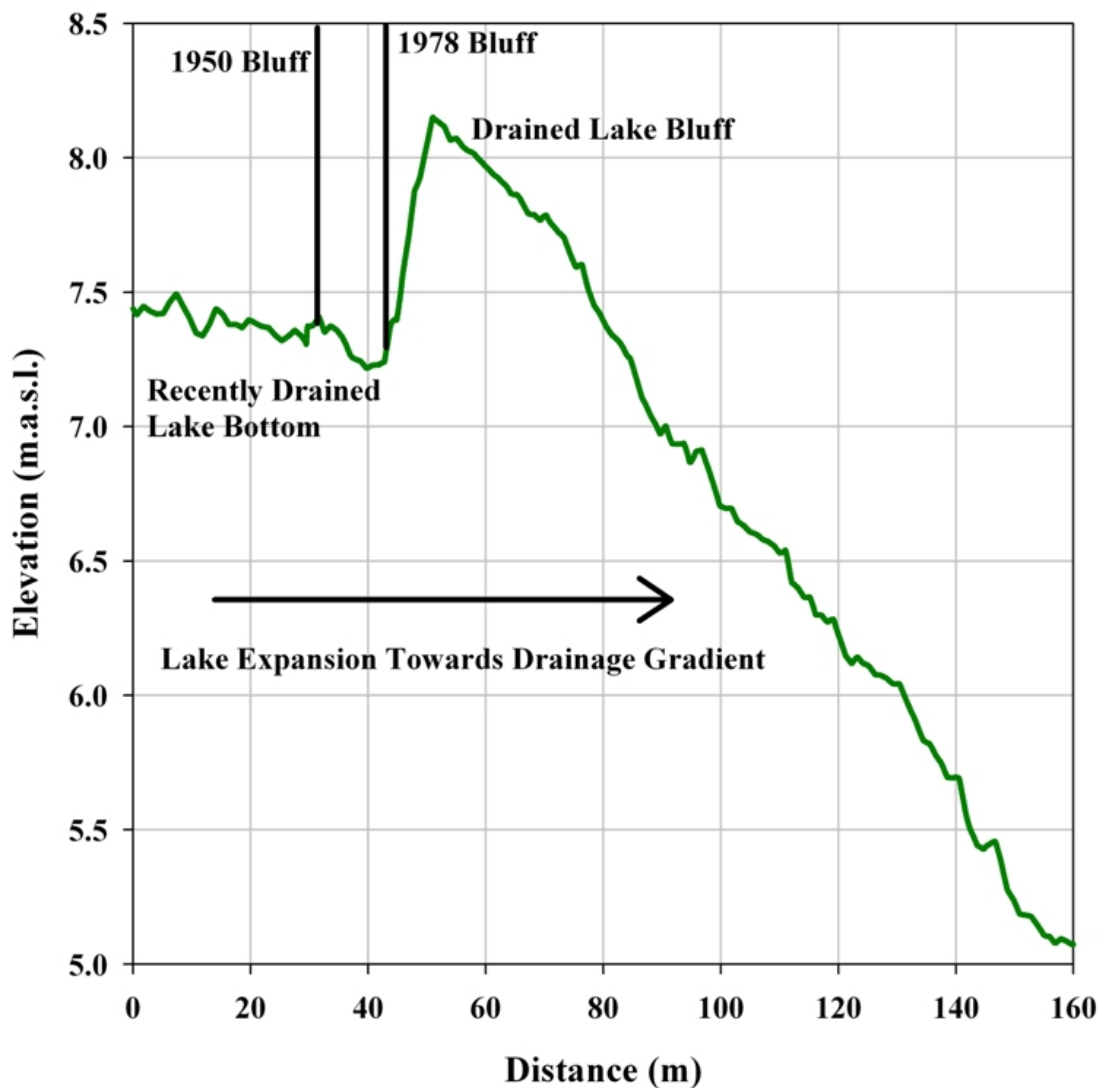


Figure 6: Topographic profile adjacent to a recently drained lake. Graph showing a topographic profile adjacent to a lake that drained during our observation period. The topographic profile is from a LIDAR dataset available for a small portion of the study region. The bluffline positions from 1950 and 1978 are marked with a vertical black line. Note expansion of the lake towards a drainage gradient. The drained of the lake created an incised channel ranging in depth from 0.7 to 1 m.

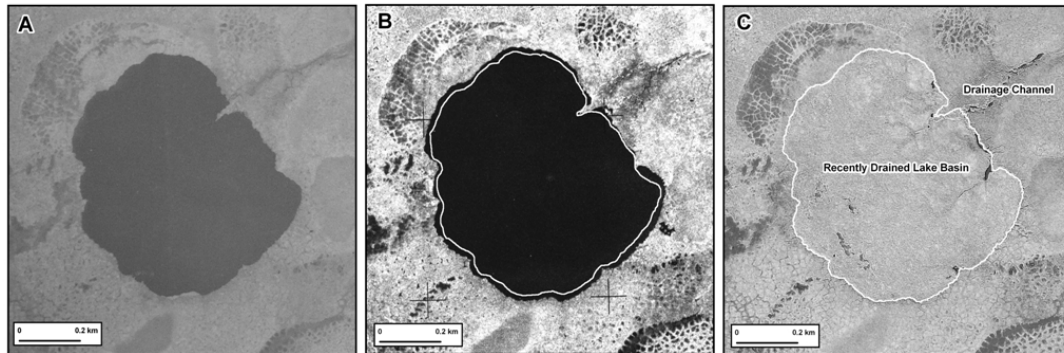


Figure 7: Image time series showing lake dynamics. Image time series showing expansion of a lake between (A) 1950 and (B) 1978 followed by its drainage between (B) 1978 and (C) 2006. The white polygon in the image from (B) 1978 shows the lake perimeter from 1950. The white polygon in the (C) 2006 image shows the lake perimeter from 1978. The lake likely drained soon after 1978 as little additional expansion occurred prior to drainage.

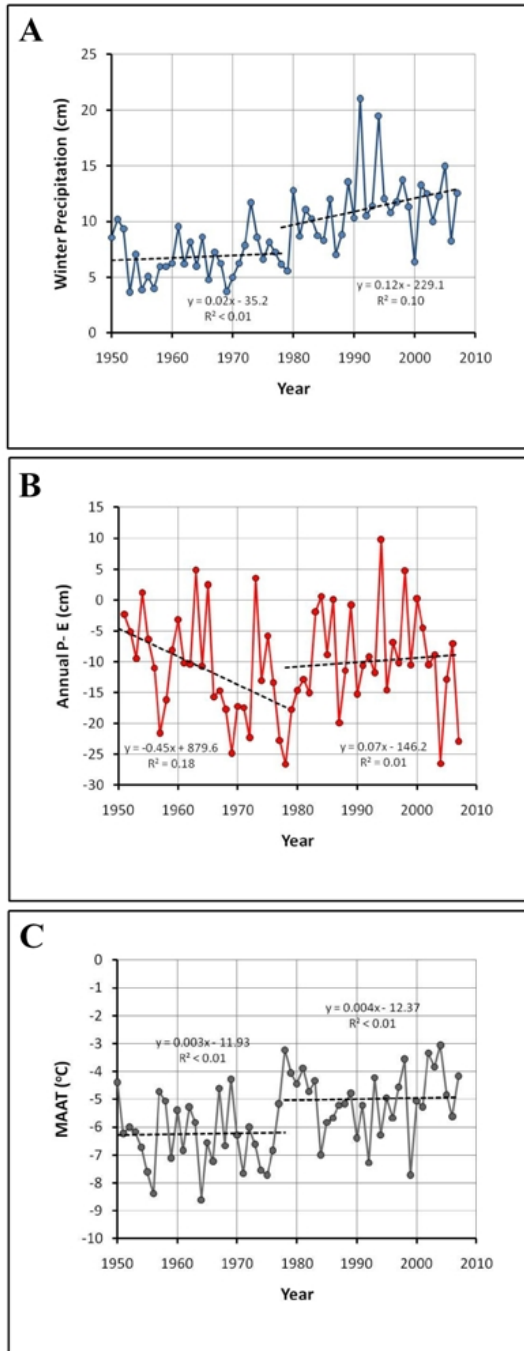


Figure 8: Climate data parameters during the study period. Climate data showing (A) winter precipitation, (B) P-E index, and (C) MAAT variation from 1950 to 2007. The first (1950 to 1978) and second (1978 to 2007) time periods are separated by different regression lines.

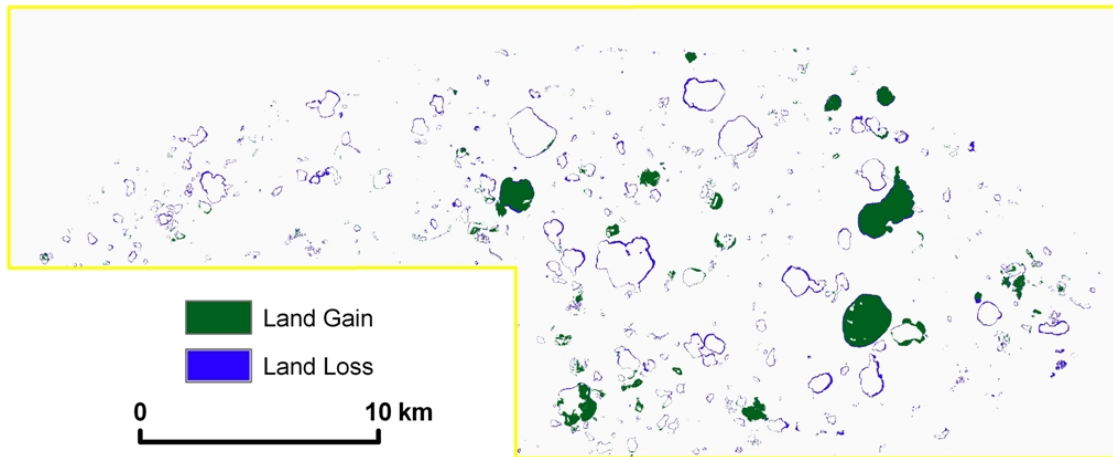


Figure 9: Landscape-scale observations of lake dynamics. Comparison of land lost (blue) through thermokarst expansion and land gained (green) as a result of thermokarst lake drainage between 1950 and 2007.

3.10 Tables

Table 1: Thermokarst lake change numbers. Change in lake number, lake area, expansion rate, and drainage events from 1950/51 to 1978 and 1978 to 2006/07 for four lake size classes.

Lake Size Class (ha)	Lake Number Change		Lake Area Change (ha)		Lake Expansion Rates (m/yr)		Lake Drainage Events	
	1950/51 to 1978	1978 to 2006/07	1950/51 to 1978	1978 to 2006/07	1950/51 to 1978	1978 to 2006/07	1950/51 to 1978	1978 to 2006/07
0.1 to 1	➤ +13	➤ +47	➤ +11	➤ +26	➤ 0.10	➤ 0.22	➤ 31	➤ 38
1 to 10	➤ -2	➤ +14	➤ -47	➤ +37	➤ 0.22	➤ 0.28	➤ 18	➤ 12
10 to 40	➤ +6	➤ 0	➤ +81	➤ +27	➤ 0.35	➤ 0.38	➤ 7	➤ 10
40 to 400	➤ -3	➤ -4	➤ +3	➤ -883	➤ 0.62	➤ 0.59	➤ 5	➤ 8

Table 2: A synthesis of thermokarst lake expansion rates. A synthesis of previously published measurements on thermokarst lake expansion rates in the Circum-Arctic.

Region	Sub-region	Number of Lakes Analyzed	Mean Expansion Rate (m/yr)	Source
Alaska	Eastern North Slope	Unknown	0.30	<i>Schell and Ziemann [1983]</i>
	Barrow Peninsula	8	0.73	<i>Lewellen [1970]</i>
	Fish Creek	Unknown	0.10	<i>Jorgenson and Shur [2007]</i>
	Northern Teshekpuk Lake Special Area	13	0.70	<i>Arp et al. [2011]</i>
	Interior Alaska	Unknown	0.10 to 2.0 (maximum rate)	<i>Jorgenson and Osterkamp [2005]</i>
	Northern Seward Peninsula	370	0.35 to 0.39	<i>this study</i>
Canada	Mayo Territory	3	0.70	<i>Burn and Smith [1990]</i>
	Hudson Bay Lowlands	Unknown	2.0 (maximum rate)	<i>Dyke and Sladen [2010]</i>
Siberia	Central Yakutia	2	0.12 to 0.52	<i>Are et al. [1979]</i>
	Lower Anadyr Lowlands	Unknown	0.5 to 5.0 (maximum rate)	<i>Tomirdiaro and Ryabchun [1973]</i>

3.11 Supporting online material

SOM Table 1: Imagery information.

Year	Julian Day	Image ID*	Image Type	Scale	Spatial Resolution (m)	RMS Error (m)	Source
1950	264	0062_0010	B&W Photography	1:43,000	1	1.6	<i>Manley et al., 2007a</i>
1950	264	0062_0013	B&W Photography	1:43,000	1	1.5	<i>Manley et al., 2007a</i>
1950	264	0062_0015	B&W Photography	1:43,000	1	1.4	<i>Manley et al., 2007a</i>
1950	264	0069_0174	B&W Photography	1:43,000	1	1.6	<i>Manley et al., 2007a</i>
1950	264	0069_0176	B&W Photography	1:43,000	1	1.7	This study
1950	264	0070_0030	B&W Photography	1:43,000	1	1.6	This study
1950	264	0095_0002	B&W Photography	1:43,000	1	1.8	<i>Manley et al., 2007a</i>
1950	264	0095_0004	B&W Photography	1:43,000	1	1.5	This study
1950	264	0095_0006	B&W Photography	1:43,000	1	1.7	This study
1950	264	0095_0032	B&W Photography	1:43,000	1	1.3	This study
1950	264	0095_0034	B&W Photography	1:43,000	1	1.5	This study
1950	264	0095_0039	B&W Photography	1:43,000	1	1.6	<i>Manley et al., 2007a</i>
1950	264	0095_0040	B&W Photography	1:43,000	1	0.6	This study
1950	264	0095_0042	B&W Photography	1:43,000	1	1.7	This study
1950	264	0095_0089	B&W Photography	1:43,000	1	2.0	<i>Manley et al., 2007a</i>
1951	194	0032_0034	B&W Photography	1:43,000	1	1.3	<i>Manley et al., 2007a</i>
1951	194	0032_0072	B&W Photography	1:43,000	1	2.2	<i>Manley et al., 2007a</i>
1978	176	0007_0010	CIR Photography	1:64,000	1	1.1	<i>Manley et al., 2007b</i>
1978	176	0007_0012	CIR Photography	1:64,000	1	0.8	<i>Manley et al., 2007b</i>
1978	176	0007_0014	CIR Photography	1:64,000	1	1.1	<i>Manley et al., 2007b</i>
1978	176	0007_0022	CIR Photography	1:64,000	1	1.1	<i>Manley et al., 2007b</i>
1978	176	0007_0024	CIR Photography	1:64,000	1	1.7	This study
1978	176	0007_0026	CIR Photography	1:64,000	1	1.7	This study
1978	176	0007_0028	CIR Photography	1:64,000	1	1.4	This study
1978	176	0007_0030	CIR Photography	1:64,000	1	1.2	<i>Manley et al., 2007b</i>
2006	236	Strip 785	IKONOS pan-sharpened multi-spectral satellite imagery	N/A	1	1.4	National Park Service, Fairbanks, AK Field Office
2007	190	Strip 926	IKONOS pan-sharpened multi-spectral satellite imagery	N/A	1	2.2	National Park Service, Fairbanks, AK Field Office

* For aerial photography image id refers to roll number and frame number (rrrr_ffff) and for IKONOS the strip number was provided by the National Park Service

Chapter 4: Identification of unrecognized tundra fire events on the North Slope of Alaska³

4.1 Abstract

Characteristics of the natural fire regime are poorly resolved in the Arctic, even though fire may play an important role cycling carbon stored in tundra vegetation and soils to the atmosphere. In the course of studying vegetation and permafrost-terrain characteristics along a chronosequence of tundra burn sites from AD 1977, 1993, and 2007 on the North Slope of Alaska, we discovered two large, previously unrecognized tundra fires. The Meade River fire burned an estimated 500 km² and the Ketik River fire burned an estimated 1,200 km². Based on radiocarbon dating of charred twigs, analysis of historic aerial photography, and regional climate proxy data, these fires likely occurred between AD 1880 and 1920. Together, these events double the estimated burn area on the North Slope of Alaska over the last ~100 to 130 years. Assessment of vegetation succession along the century-scale chronosequence of tundra fire disturbances demonstrates for the first time on the North Slope of Alaska that tundra fires can facilitate the invasion of tundra by shrubs. Degradation of ice-rich permafrost was also evident at the fire sites and likely aided in the presumed changes of the tundra vegetation post-fire. Other previously unrecognized tundra fire events likely exist in Alaska and other Arctic regions and identification of these sites is important for better understanding disturbance regimes and carbon cycling in Arctic tundra.

³Jones, B. M., A. L. Breen, B. V. Gaglioti, D. H. Mann, A. V. Rocha, G. Grosse, C. D. Arp, M. L. Kunz, and D. A. Walker (2013), Identification of unrecognized tundra fire events on the north slope of Alaska, *Journal of Geophysical Research* 118, doi:10.1002/jgrg.20113.

4.2 Introduction

Fire influences vegetation distribution and structure, carbon cycling, land-atmosphere energy exchange, and climate, and it represents an important and widespread disturbance mechanism in several major biomes [Bowman et al., 2009]. However, the role of fire in shaping ecosystem patterns in Arctic tundra remains poorly resolved due to the rarity of reported fires, the geographic remoteness of the region, and the short observational record in the region [Barney and Comiskey, 1973; Wein, 1976; Giglio et al., 2006; Rocha et al., 2012]. As a result, an accurate representation of the Arctic in models depicting the geographic distribution of wildfires and potential shifts in global wildfire activity and pyrogenic gas emissions is lacking [Bond et al., 2005; Krawchuk et al., 2009; van der Werf et al., 2010]. Given ongoing climate change in the Arctic [ACIA, 2005; AMAP, 2011], the frequency, severity, and areal extent of tundra fires is predicted to increase [Higuera et al., 2008; Hu et al., 2010]. Thus, a better understanding of the role of fires in the tundra biome is needed since tundra vegetation, peat, and frozen soils in the Arctic store large, globally significant amounts of labile carbon [McGuire et al., 2009; Tarnocai et al., 2009], and pulse disturbances, such as fire, can play an important role in releasing this carbon [Grosse et al., 2011; Mack et al., 2011].

Since the middle of the 20th Century, Arctic tundra fires have been primarily documented in Alaska [Wein, 1976; Barney and Comiskey, 1973; Racine et al., 1985; AICC, 2012]. Historically, a spatial gradient in annual area burned in tundra vegetation extended from the Seward Peninsula (frequent and extensive fires) towards the northeast (fewer and smaller fires) [Racine et al., 1985]. A more contemporary analysis of the fire

history database [AICC, 2012] reveals a northward shift in annual area burned in the Alaskan tundra regions from 1950-2012, with an increase in the size of fires north of the Arctic Circle over the past two decades [Rocha et al. 2012]. Interestingly, analysis of a portion of the fire history database indicates a weak but positive correlation between declining summer sea ice extent in the Arctic Ocean and an increasing trend in the area of tundra burned since 1979 [Hu et al., 2010].

The 2007 Anaktuvuk River fire burned more than 1,000 km² on the North Slope of Alaska [Jones et al., 2009] and factors prominently in these emerging trends. This large event has prompted the notion that the northern Alaska tundra fire regime may be shifting [Jones et al., 2009; Hu et al., 2010; Mack et al., 2011; Rocha et al. 2012]. While the Anaktuvuk River tundra fire has created a natural laboratory to study the impact of fire on Arctic ecosystems it has also raised several questions, including (1) is it possible that other large tundra fires occurred prior to the period of record keeping, (2) how complete is the record of tundra fires in northern Alaska, and (3) what is the long-term impact of tundra fires on vegetation and permafrost-terrain characteristics? Here we report results from ground-based observations and measurements of vegetation and surface permafrost terrain characteristics in the aftermath of tundra fires that occurred in 1977, 1993, and 2007. Through these efforts we were able to gain a better understanding of the role of tundra fire on landscape change on the North Slope of Alaska over decadal time-scales. Analysis of post-fire vegetation and landscape succession in concert with remotely sensed imagery led to the discovery of two large and eight small unrecognized tundra fire events in the region. Here we primarily describe and characterize previously

unrecognized tundra fires in the Meade and Ketik River watersheds and discuss their potential significance in ecological and climate change contexts.

4.3 Study area and methods

The study area consists of the northern portion of the Arctic Foothills on the North Slope of Alaska (Figure 1). Aerial observations and ground surveys were conducted between 69° to 70° N latitude and 150° to 163° W longitude, covering much of the loess belt, or a region which typically contains Pleistocene-aged, ice-rich permafrost deposits (Yedoma) [Kanevskiy et al., 2011]. Combined, these efforts led to the development of criteria for identifying old tundra fires based on post-fire characteristics of geomorphology and vegetation. This information was then combined with remotely sensed imagery to map the previously unrecognized tundra fires. Additional field surveys were then conducted to validate the interpretation of the remotely sensed imagery.

4.3.1 Landscape-scale aerial observations

In order to develop landscape-scale criteria for the impact of tundra fires on the North Slope, we conducted aerial observations of active fires as well as known, past burn sites. We did this to describe the basic patterns and processes of wildfires in tundra and to identify key characteristics that would aid in the recognition of prehistoric fires. Aerial observations of the tundra burn sites on the North Slope of Alaska began in September 2007 during the period of rapid expansion of the Anaktuvuk River Fire. Aerial reconnaissance conducted during this period allowed for the observation of fire behavior as it migrated across the landscape (Figures 2a and 2b). Aerial reconnaissance was also

conducted at the 1993 and 1977 burns in July 2011 and June 2012 to assess post-fire patterns of landscape change (Figures 2c and 2d). While flying over the region, we observed other areas that resembled the landscape characteristics of these previously burned sites but were not identified as having burned during the historic period (Figures 2e and 2f).

4.3.2 Ground observations and surveys

Ground-based surveys at the 2007 Anaktuvuk River Fire [Jones et al., 2009], the 1993 DCKN190 Fire [Barrett et al., 2012], the 1977 Kokolik River Fire [Hall et al., 1978], two unburned control sites, and two putative fire sites were conducted in July 2011 and late-June 2012 (Figure 1). The surveys focused on upland tundra settings and provided information on vegetative and geomorphological differences between burned and unburned sites. We selected unburned sites that were moist tussock tundra dominated by tussock cottongrass (*Eriophorum vaginatum*), which is the most commonly burned vegetation community in Arctic Alaska [Rocha et al., 2012]. The burned sites were then selected in areas of similar elevation and topography that were inferred to be moist tussock tundra pre-fire based on the presence and abundance of live or dead *E. vaginatum* tussocks. The tussocks, especially in the younger fire scars, often showed evidence of charring at their base. Our aim in this sampling design was to establish a chronosequence of sites that vary in time since last fire to better understand post-fire vegetation successional trajectories. While we cannot be certain plant communities followed the same post-fire successional pathway in this space-for-time substitution, we use the chronosequence approach as an exploratory method given the absence of direct

repeat post-fire observations on the North Slope. A recent analysis found chronosequences are most appropriate for studying plant communities that are following convergent successional trajectories and have low biodiversity, and low frequency and severity of disturbance [Walker et al., 2010] suggesting this approach has high potential to be applicable in the Arctic.

Full floristic surveys were conducted using the point intercept sampling method recommended by the Alaska Interagency Fire Effects Task Group [2007]. Plant species and height were recorded every 1-m along three (burned sites) and two (unburned sites) 30-m transects. All taxa that touched the sampling pin were recorded as 'hits'. Percent cover was calculated by dividing the number of hits for each taxa by the total number of points along each transect. The transects from the two unburned sites were pooled for a total of four transects in undisturbed moist tussock tundra. Nomenclature follows the Panarctic Species List (v. 1.0) developed for the Arctic Vegetation Archive [Walker & Raynolds 2011; Walker et al., 2013]. Plant species were grouped into broad functional types (SOM Table 1; shrub, forb, grass, sedge, rush, bryophyte, lichen or other), averaged across transects within a site, and a chi-square contingency analysis was used to determine if functional types were randomly distributed across sites or more predominant at some sites compared to others. To test if canopy height differed among sites, we used an analysis of variance (ANOVA) followed by *a posteriori* (Student's T) contrasts to compare mean canopy height across sites. The putative fire sites were not included in this analysis since we could not perform an ANOVA with 6 sites and a sample size of only 3-4 transects per site.

Micro-topographic surveys along linear transects across a series of ice-wedge polygons and troughs were conducted at each site using a survey-grade Leica Viva® differential global positioning system (DGPS). A base station was established at each site that recorded fixed positions, and DGPS data collection was acquired with a rover antenna using real time kinematic corrections. This resulted in high resolution, horizontal (<1 cm) and vertical (2-4 cm), topographic data. These surveys allowed us to identify variation in relief due to degradation of ice wedges (thermokarst) in burned and unburned upland terrain settings. Given the time of the year associated with site visits we were not able to conduct robust measures of variability in active layer thickness.

4.3.3 Analysis of remotely sensed imagery

Delineation of the putative fire sites relied primarily on the surface expression or apparent increase in texture in high resolution (<2 m) remotely sensed imagery (Figure 3), aerial and ground-based surveys, and natural barriers such as river corridors that showed sharp contrasts between what was interpreted as burned and unburned tundra. The entire perimeter of the Meade River site was covered by high resolution satellite imagery acquired between 2002 and 2012; whereas, the Ketik River site had approximately 50% coverage by high resolution satellite imagery from 2002 to 2012. Where high resolution imagery was lacking, we assessed spectral bands 4, 2, and 1 from a Landsat TM image (30 m) acquired on 09 July 2010 by applying a 2% linear histogram stretch within an upland tundra setting that exhibited the characteristic increase in image texture visible in the high resolution imagery. This technique emphasized the vegetative characteristics associated with the putative fire sites and was used to further delineate the

perimeters. By combining terrain surface roughness characteristics with remotely sensed vegetative characteristics, we manually delineated the estimated burn perimeters at a scale of 1:40,000. Vegetation metrics such as NDVI and EVI were determined for the Landsat scene; however, the utility in accurately delineating these features using these indices proved unfruitful.

4.3.4 Field verification of unrecognized fire events

The two putative tundra fire sites were visited in June 2012 to validate our remote sensing analysis. We did this by conducting aerial surveys across the mapped area as well as complementary vegetative and micro-topographic surveys to determine whether the upland tundra settings in these sites were more similar to known burn sites or to the unburned sites. We also dug several soil pits at randomly selected locations to look for charcoal. In the field, we tested for the presence of charcoal by smearing samples on white paper. In the laboratory we examined these samples under 10-50x magnification. Approximately 5 mg of charred woody material was extracted from each site and sent to Beta Analytic Inc. for radiocarbon dating using accelerator mass spectrometry. Calibration of the dated material was conducted using the $\delta^{13}\text{C}$ -adjusted age and CALIB 6.1 [Reimer et al., 2009].

4.4 Results

4.4.1 Delineation of unrecognized tundra fires

We delineated the perimeters of two large and previously unrecognized tundra fires by combining field observations with remotely sensed imagery (Figure 4). The Meade River fire burned an estimated area of 500 km². The centroid of the burn

perimeter lies at 69° 56.4' N, 157° 24.6' W. The fire was bounded by the Meade River on its eastern margin and burned a north to south distance of 40 km. The Ketik River fire burned an estimated area of 1,200 km²; however, the delineation of the perimeter at this site was hampered by the lack of contemporary high resolution satellite imagery. Thus, portions of this fire extent were based on the histogram-stretched Landsat image and natural landscape barriers. The centroid of the burn perimeter lies at 69° 45.3' N, 159° 36.0' W. Based on this delineation, the Ketik River fire burned a distance of 60 km north and south and was largely confined between the Ketik River on the east and the Koalak River on the west.

4.4.2 Charred material and age control

In order to find indisputable evidence that these sites had burned, we extracted soil plugs to look for charcoal layers. We visited three sites within the Meade River fire and found charcoal preserved at all three sites. The charred layer was approximately 1 cm thick and was buried beneath 7-9 cm of organic matter that had accumulated post-fire (Figure 5a). A total of eight sites were visited in the Ketik River fire and charred material was encountered at two. The best preserved site contained a 0.5 cm thick charred layer that was overlain by 12 cm of peat and vegetation (Figure 5b). At the sites where we did not find charcoal, there was approximately 10 to 12 cm of organic material accumulation directly atop mineral soil.

Several pieces of charred woody material from one location at each site were used to determine the approximate, maximum time since fire. The measured radiocarbon age of the charred material from the Meade River fire was 70±30 ¹⁴C yrs BP and the

measured radiocarbon age of the Ketik River fire was 100 ± 30 ^{14}C yrs BP, where "BP" indicates radiocarbon years before AD 1950 (Table 1). Calibration of these sample ages to calendar years using the $\delta^{13}\text{C}$ -adjusted ages resulted in six possible age ranges for the Meade River site that span from AD 1695 to 1954 and three possible age ranges for the Ketik River site that span approximately the same time interval. Of the six possible calibrated age ranges for the Meade River sample, the periods AD 1695-1726 and AD 1876-1918 account for 20% and 60% of the total probability under the calibrated age distribution, respectively (Table 1). Of the three possible age ranges for the Ketik River sample, the highest probability under the calibrated age distribution (74%) is the period AD 1812-1919 (Table 1).

4.4.3 Vegetative and geomorphic characteristics

The distribution of plant functional types differs markedly among sample sites (Figure 6 and Figure 7; SOM Table 1; $\chi^2=236.728$, d.f.=35, $P<0.0001$). At the three sites that burned since the mid-1970s, grass cover (primarily *Arctagrostis latifolia* and *Calamagrostis lapponica*) was higher relative to the unburned moist tussock tundra sites, which were dominated by sedge species (primarily *Eriophorum vaginatum* and *Carex bigelowii*). At the two newly identified fires, the greatest deciduous shrub cover was observed (primarily *Salix pulchra*, *Betula nana* and *Rhododendron tomentosum* ssp. *decumbens*), while grass cover was lower than that observed for the sites that burned more recently (Figure 6b). Bryophyte and lichen cover was greatest in the unburned site and oldest fire sites, while lichens were absent from the two more recent Anaktuvuk

River and DCKN fires. The bryophytes at these two more recent fires were primarily the early colonizing pyrophytes including *Marchantia polymorpha* ssp. *ruderalis*, *Ceratodon purpureus*, *Leptobryum pyriforme* and *Pohlia nutans*. In contrast, bryophyte taxa such as *Sphagnum* were only observed at the unburned sites. We also observed a significant difference among sites in the height of the vegetation, with canopy heights from 1/2 to six-times greater in burned versus unburned areas (Figure 6a; ANOVA, $F_{3,9} = 386.56$, $P < 0.0001$). In particular, taller shrubs tended to be found in the burned upland tundra sites relative to the unburned upland tundra sites.

There were also differences in micro topography among sites with varying time since fire (Figure 7). The typical micro-relief associated with ice wedge troughs in the unburned, upland control sites was 0.2 to 0.5 m. In contrast, micro-relief associated with ice wedge troughs in the DCKN190 fire site ranged from 0.7 to 1.3 m, while at the Kokolik River site it ranged from 0.5 to 1.0 m. Micro-relief across ice-wedge troughs at the Meade River fire survey site ranged from 0.7 to 1.1 m and from 0.5 to 1.0 m at the Ketik River fire survey site.

4.5 Discussion

4.5.1 Spatial and temporal context of fire on the North Slope of Alaska

Between 1950 and 2012, forty-two tundra fires are known to have occurred on the North Slope of Alaska, with the earliest reported burn in 1959 [AICC, 2012]. These forty-two fires burned a combined area of 1,635 km². The majority (~83%) of these fires have been small, burning areas <10 km². Four of the five largest fires observed on the North Slope over this period occurred in the past two decades, which define the pattern

described by Rocha et al. [2012]. There has also been an increase in the total number of fires detected on the North Slope, particularly in the last decade, but many of these are very small ($< 0.5 \text{ km}^2$), and their detection likely a result of better observational coverage [Miller, 2010]. Spatially, tundra fires have primarily occurred in the Arctic Foothills between the Brooks Range and the Arctic Coastal Plain (Figure 1). Only three fires have been documented on the Arctic Coastal Plain and all three of these occurred between 2011 and 2012.

Together the Meade River (500 km^2) and Ketik River ($1,200 \text{ km}^2$) fires roughly equal the area burned on the North Slope of Alaska over the period of record keeping [AICC, 2012]. Addition of these sites to the fire history database would make the Ketik River fire potentially the largest documented event and the Meade River fire the third largest documented event in the region. However, these delineated areas should be viewed as approximations as it is even difficult to accurately delineate fire perimeters that occur during the remote sensing period, which began around the 1950s [Kasischke and Turetsky, 2006; Barrett et al., 2012]. These delineated areas should also be viewed as maximum burn extents since tundra fires exhibit a heterogeneous burn pattern with numerous unburned inclusions. A patchy burn pattern at the Ketik River site could explain the lack of charcoal encountered within the estimated burn perimeter. This could also result from the presence of a more uniformly graminoid-rich tundra at the time of the burn because this vegetation type often leaves no partially burned charred material [Cofer et al., 1990]. Alternatively, it could indicate that the fire severity varied across the burn extent or that we have over-estimated the size of this fire.

Both the Meade River and Ketik River fires likely occurred as single events sometime during the last 300 years (Table 1). Due to limitations associated with radiocarbon dating during this period we can only provide the possibility of the fires in several different age ranges. In addition, the charcoal material we dated was fixing atmospheric carbon before these fires occurred. We consider the period between C fixation and fire (in-built age) for the material we dated (burned twigs) to be a few years and at most a few decades [Gavin, 2006]. Nevertheless, we can further constrain the timing of the two fires by assessing the probability distribution of calendar year calibration ages, historic aerial photographs, and regional climate proxy records.

For both the Meade and Ketik sites the most recent calibrated age range occurred between AD 1952 and 1954. However, this age window accounts for a low probability of the sample (2-3%) making it very unlikely to be the calendar age of the charcoal. Furthermore, analysis of aerial photography acquired in the late-1940s revealed that the increased landscape texture and inferred fire perimeters at the Meade and Ketik sites were already present at this time (SOM Figure 1). The oldest possible age range for both fires occurred between AD 1695 and 1725. The probability that the Meade and Ketik fires occurred during this time period are 20% and 24%, respectively. This period is coincident with the Little Ice Age (LIA), and in particular the coldest and driest phase of the LIA on the North Slope [Bird et al., 2009]. While, presumably this was a period with little thunderstorm activity, large tundra fires could have occurred owing to the dry conditions. The final possible calibrated calendar year age ranges for these events occur between AD 1810 and 1920. The probability distribution for both the Meade and Ketik

sites is highest during this time, 77% and 74%, respectively. Within this time period, results from the Meade River sample indicate four possible age ranges, with AD 1876 to 1918 yielding a 60% probability. Results from the Ketik sample only indicate the one age range (AD 1812 to 1919) during this period. Jorgenson et al. [2006] noted the possibility of widespread thermokarst pit formation between AD 1850 and 1940 for a study site approximately 200-300 km to the northeast of these fires sites. Furthermore, Bird et al. [2009] suggest that the period after AD 1880 marked a transition to regionally warm and dry conditions. Thus, given the probability distribution of ages from radiocarbon dating, the presence of fire altered tundra in the 1940s photography, and regional climate proxy data both fires likely occurred between AD 1880 and 1920 or shortly thereafter when considering the in-built age factor [Gavin, 2006].

The discovery of the Meade and Ketik Fires indicate large tundra fires on the North Slope of Alaska have likely occurred as recently as the last ~100 to 130 years. It is likely that other fire events of variable size have also occurred in the region that remain to be discovered (SOM Figure 2) and that the role of fire as a disturbance agent in Arctic tundra in general has likely been underestimated. Efforts that seek to determine the historical context of large fires on the North Slope are still in their nascent stage. In addition, our cursory analysis of a subset of the remote sensing archive for the region identified eight small tundra fires not documented in the fire history database (Figure 1). While the focus of this paper is on the detection of the large pre-historic events, a recent study highlighted the important role of small fire events on fire regimes and that globally

there was a 35% underestimate in the area burned as a result of omission of small fires [Randerson et al., 2012].

These data also add to the growing observations concerning the fire regime of the North Slope region. Based on recent (AD 1950 to present) [Rocha, et al., 2012] and paleo (last ~5000 years) [Hu et al., 2010; Higuera et al., 2011] estimates of fire rotation periods (the amount of time it would take for a specified region to burn) and fire return intervals (the number of years between successive fires at a given location) for the North Slope of Alaska converge on a time frame of 4000–5000 years, respectively. Addition of our sites to this estimate for the region using the highest probability calibrated age ranges (AD 1810 to 1920) and the definition of the North Slope as provided in Rocha et al. [2012] indicate a fire rotation period that ranges from approximately 3000 to 7000 years. Up to this point, the North Slope has a scant and evolving data set of past fire frequency compared to other systems where fire rotation periods have been estimated based on decades of research [e.g., Sousa, 1984]. Estimates of a fire rotation period for the study area have proven to be highly variable when using different calibrated age ranges of the fires discovered here. For example, using the period AD 1810–2012 results in a fire rotation period of ~7000 years and using the period AD 1920–2012 results in a fire rotation period of ~3000 years. Given the uncertainties in a minimal number of radiocarbon samples, the in-built age factor, and the fact that future work is needed to better reconstruct the fire history in the region, we have included these calculations in this paper a bit reluctantly. In addition, a recent modeling effort focused on fire return

intervals in Alaska found values that ranged from 100 to 200 years, 500 to 700 years, and greater than 2000 years for various locations on the North Slope of Alaska [Pfeiffer et al. 2013]. These wide ranging estimates in the repeated burning of Arctic tundra in this region highlight the need for more concentrated work with respect to potential past tundra burning.

4.5.2 Wildland fires and shrub invasion of tundra

Direct measures of the ecological impacts of tundra fires on vegetation on the North Slope of Alaska over decadal and centennial time scales are sparse to non-existent. Observations at the Anaktuvuk River Fire indicate that graminoid cover is substantially greater than shrub cover in the first four years post-fire [Jandt et al., 2012; Bret-Harte et al., 2013]. Observations at the 1977 Kokolik River site spanning the first five years post-fire also support this pattern [Racine et al., 1987]. At the other large historic tundra fire site, the 1993 DCKN190, graminoid cover remained greater than shrub cover 17 years post-fire, but the proportion of grasses relative to sedges had increased [Barrett et al., 2012]. Remotely sensed observations of vegetation change in tundra sites that burned in the last several decades also follow this general pattern with an increase in both albedo and greenness that is interpreted as an increase in grass cover [Rocha et al., 2012]. Our observations from one site located in the northern portion of the Anaktuvuk River Fire also follow this short-term trajectory, but we note a substantial difference in grass cover (primarily *Arctagrostis latifolia* and *Calamagrostis lapponica*) relative to our unburned upland moist tussock tundra site in the first five years post-fire (Figures 6b and 7b). Our

results also indicate a greater abundance of grass cover at the 1993 fire site (Figures 6b and 7c) similar to that found by Barrett et al. [2012], whereas vegetation present at the 1977 burned site resembled the younger fire sites but with the addition of lichens that were absent from the 2007 Anaktuvuk River and 1993 DCKN190 fires (Figure 6b and 7d).

Addition of the Meade River and Ketik River sites to the chronosequence of burned upland tundra used to infer fire-related changes in vegetation indicates the relative proportion of grasses is less than more recently burned sites, yet still far greater than unburned tundra, likely reflecting the legacy of past burning. Moreover, the proportion of shrubs is greatest at these two sites (Figures 6b, 7e, and 7f). We interpret the greater abundance of shrubs to reflect secondary succession from grass to shrub dominance post-fire. On the more southerly, warmer Seward Peninsula post-fire secondary succession in tundra is known to be accompanied by a transition from grasses to shrubs over a time scale of several decades, [Racine et al., 2006]. However, on the North Slope of Alaska this transition has not been documented previously, and our results provide the first compelling evidence of a shift towards shrubbier conditions post-fire in the region. These findings have implications when interpreting the modern distribution of shrubs on the North Slope of Alaska [Beck et al., 2011] and indicate that fire could play a key role in the ongoing "shrubification" of the region [Sturm et al. 2001; Tape et al., 2006].

4.5.3 Fire history and permafrost degradation

Tundra fires can trigger thermokarst by removing insulating layers of vegetation and peat and decreasing albedo at the ground surface. In the southern portion of the

Anaktuvuk River Fire, Mann et al. [2010] noted the widespread occurrence of active layer detachment slides and several thaw slumps forming over the first three years following the burn. Rocha et al. [2012] synthesized thaw depth measurements for all known tundra burn sites in Alaska and found that there was a sustained increase in the thaw depth within burned sites even three decades post-fire. While we lack robust measures of active layer thickness variation and did not see widespread evidence of stabilized detachment slides and thaw slumps, we did notice widespread formation of thermokarst pits at our sites and conducted micro-topographic surveys to capture the relief associated with ice-wedge troughs, as the formation of thermokarst pits is also an indicator of permafrost degradation [Jorgenson et al., 2006].

The microtopography of ice-wedge polygons (raised centers to troughs) in undisturbed upland tussock tundra settings was 0.2 to 0.5 m (Figure 7a). When viewing these sites in high-resolution remotely sensed imagery, it is difficult to distinguish individual polygons (Figure 3a). However, in images from the Anaktuvuk River fire four years after the burn, the increase in texture is evident (Figure 3b), and the ice wedge trough micro-topography show initial signs of thermokarst (Figure 7b). For the sites that had burned in 1977 and 1993, the relief associated with ice wedge troughs ranges from 0.5 to 1.3 m indicating that the fires disrupted the soil thermal regime leading to permafrost degradation (Figures 7c and 7d). This shows up in the high resolution imagery as an increase in texture (Figures 3c and 3d). DGPS surveys conducted at the Meade River and Ketik River sites were more similar to the burn sites than the unburned sites, with micro-relief associated with the ice wedge troughs on the order of 0.5 to 1.1 m

(Figures 7e and 7f). However, one notable difference between these sites and the sites that burned in 1977 and 1993 (Figures 3c and 3d) was the lack of ponded water in the ice wedge troughs (Figures 3e and 3f). We interpreted that this could be the result of a more integrated drainage network in these older burn sites or paludification of the troughs and infilling with peat and vegetation.

The presence of near-surface, ice rich permafrost terrain with massive ice in the form of wedges was essential for the identification of the previously unrecognized tundra fire events. The degradation of ice-rich permafrost terrain likely plays an important role in post-fire vegetation succession trajectories as noted by Bret-Harte et al. [2013]. Thus, the increase in shrubbiness at the century-old fire sites is likely due in part to ice-rich permafrost degradation and it was the combination of vegetative and geomorphic change that aided in our ability to identify these sites. While it appears that large fires on the North Slope tend to occur in this belt of ice-rich permafrost, several small historic fires have occurred in areas not indicative of ice-rich permafrost terrain (Figure 1). Detection of fires that pre-date the period of record keeping in these area would be difficult to detect by using the techniques applied in this study. These findings also have implications for potential future successional trajectories associated with the Anaktuvuk River fire. Figure 1 indicates that the northern two-thirds of this fire perimeter may experience more widespread ground subsidence as a result of post-fire permafrost degradation relative to the southern one-third, where surface permafrost deposits tend to be less ice rich. Thus, spatially variable responses in vegetation succession should be expected as a result of this fire event in the years and decades to come.

4.6 Broader implications

Identification of the Meade River and Ketik River fires may have Arctic-wide implications. Mack et al. [2011] found that the 2007 Anaktuvuk River fire released 2.1 Tg of C to the atmosphere, which is equivalent to the annual net C sink for the entire Arctic biome. If the Meade River and Ketik River fires released similar amounts of C during combustion, these events may have had a similar immediate impact on atmospheric carbon. There may also be an important long-term impact of these disturbances because the fires here may promote the degradation of the yedoma-like deposits (areas with Pleistocene aged permafrost deposits that can be high in ice and carbon content) that occur in this region (Figure 1) [Kanevskiy et al., 2011]. The apparent shift from sedge-dominated tundra to shrub-dominated tundra that we documented in the older burn sites could also have a positive feedback on climate warming due to the combination of a decrease in albedo and an increase in evapotranspiration associated with this transition [Euskirchen et al., 2009; Bonfils et al., 2012]. Thus, during a period of already rapid shrub expansion in the Arctic [Myers-Smith et al., 2011] in which tundra fires are becoming larger and more frequent [Rocha et al., 2012], this process may be exacerbated. Further, an increase in shrub abundance may also lead to an increase in the frequency, severity, and areal extent of tundra fires [Higuera et al., 2008], which may lead to an increase in C release [Mack et al., 2011]. However, very little is known about the balance of C storage following tundra fires. The complexities associated with the long-term C budget at burned tundra sites underscore the

importance of better understanding the spatial and temporal context of tundra fires in the Arctic.

4.7 Conclusions

We discovered two large and previously unrecognized tundra fire events on the North Slope of Alaska using the increase in landscape texture that resulted from vegetation changes and ice-wedge degradation post-fire. The Meade River fire burned an estimated 500 km² and the Ketik River fire burned an estimated 1,200 km². Based on radiocarbon dating and analysis of historic aerial photography, and climate proxy data, these fires likely occurred between AD 1880 and 1920, making them the oldest delineated tundra fire perimeters in Arctic Alaska. Recognition of these fires potentially doubles the estimated area of burned tundra on the North Slope of Alaska during the last ~100 to 130 years. Identification of these sites also provides a centennial-scale chronosequence of post-fire vegetation and geomorphic change providing a valuable temporal context for better understanding the impacts of tundra fires during a period in which they are expected to increase in their number, size, and frequency.

4.8 Acknowledgements

The authors gratefully acknowledge support provided by the U.S. Geological Survey - Alaska Science Center and the Bureau of Land Management - Arctic Field Office. We thank Dr. Philip Higuera, Dr. Eric Kasischke, and Eric Miller for their constructive and helpful reviews. We are also grateful to Drs. Misha Zhurbenko and Olga Afonina of the Komarov Botanical Institute at the Russian Academy of Sciences for identification of lichens and bryophytes. We would like to thank Jim Webster of Webster's Flying Service

as his expertise over the last several years has been invaluable. Any use of trade, product, or firm names is for descriptive purposes only and does not imply endorsement by the U.S. Government.

4.9 References

ACIA (2005), *Impacts of a warming arctic: arctic climate impact assessment*, Cambridge University Press, Cambridge, UK.

AICC (2012), *Fire History in Alaska*, Alaska Interagency Coordination Center, [Available at http://afsmaps.blm.gov/imf_firehistory/imf.jsp?site=firehistory].

Alaska Interagency Fire Effects Task Group (2007), *Fire Effects Monitoring Protocol* (version 1.0), Editors: Allen, J., K. Murphy, and R. Jandt http://depts.washington.edu/nwfire/publication/AK_Fire_Effects_Monitoring_Protocol_2007.pdf

AMAP 2011, *Snow, Water, Ice and Permafrost in the Arctic (SWIPA): Climate Change and the Cryosphere*. Arctic Monitoring and Assessment Programme (AMAP), Oslo, Norway. 538 pp.

Barney, R. J., and A.L. Comiskey (1973), *Wildfires and thunderstorms on Alaska's North Slopes*, USDA Forest Service Pacific Northwest Forest and Range Experiment Station, Portland, OR Research Note PNW-311.

Barrett, K., A.V. Rocha, M.J. van de Weg, and G. Shaver (2012), *Vegetation shifts observed in arctic tundra 17 years after fire*. *Remote Sens. Lett.*, 3, 729–36.

Beck, P. S. A., N. Horning, S.J. Goetz, M. M. Loranty, and K. Tape (2011), *Shrub cover on the North Slope of Alaska: a circa 2000 baseline map*, *Arctic, Antarctic and Alpine Research*, 43, 355-363 doi: 10.1657/1938-4246-43.3.355.

Bird, B. W., M. B. Abbot, B. P. Finney, and B. Kutchko (2009) *A 2000 year varve-based climate record from the central Brooks Range, Alaska*, *J Paleolimnol*, 41, 25-41.

Bond, W. J. et al., (2005), *The global distribution of ecosystems in a world without fire*, *New Phytologist*, 165, 525-538.

Bonfils, C. J. W., T. J. Phillips, D. M. Lawrence, P. Cameron-Smith, W. J. Riley, and Z. M. Subin (2012), *On the influence of shrub height and expansion on northern high latitude climate*, *Environ. Res. Lett.*, 7, 015503.

- Bowman, D. M. J. S. et al. (2009), Fire in the Earth System, *Science*, 324, 481-484.
- Bret-Harte, M. S., M. C. Mack, G. R. Shaver, D. C. Huebner, M. Johnston, C. Mojica, C. Pizano and J. A. Reiskind (2013), The response of Arctic vegetation and soils following an unusually severe tundra fire, *Phil. Trans. R. Soc. B.*, 368, 20120490.
- Cofer, W. R., J. S. Levine, E. L. Winstead, P. J. LeBel, A. M. Koller, and C. R. Hinkle (1990), Trace gas emissions from burning Florida wetlands, *J. Geophys. Res.*, 95, 1865–1870.
- Euskirchen, E. S., A. D. McGuire, F. S. Chapin, S. Yi, and C. C. Thompson (2009), Changes in vegetation in northern Alaska under scenarios of climate change, 2003-2100: implications for climate feedbacks, *Ecological Applications*, 19, 1022-1043.
- Gavin, D. G. (2006), Estimation of inbuilt age in radiocarbon ages of soil charcoal for fire history studies, *Radiocarbon*, 43, 27-44.
- Giglio, L., I. Csizsar, and C. O. Justice (2006), Global distribution and seasonality of active fires as observed with the Terra and Aqua Moderate Resolution Imaging Spectroradiometer (MODIS) sensors, *J. Geophys. Res.*, 111, G02016 doi:10.1029/2005JG000142.
- Grosse, G. et al. (2011), Vulnerability of high-latitude soil organic carbon in North America to disturbance, *J. Geophys. Res.*, 116, G00K06 doi:10.1029/2010JG001507.
- Hall, D. K., J. Brown, and L. Johnson (1978), The 1977 tundra fire at Kokolik River, Alaska, *Arctic*, 31, 54–58.
- Higuera, P. E., L. B. Brubaker, P. M. Anderson, T. A. Brown, A. T. Kennedy, and F. S. Hu (2008), Frequent fires in ancient shrub tundra: implications of paleorecords for arctic environmental change, *PLoS ONE*, 3, e0001744 doi: 10.1371/journal.pone.0001744.
- Higuera, P. E., M. L. Chipman, J. L. Barnes, M. A. Urban, and F. S. Hu (2011), Variability of tundra fire regimes in Arctic Alaska: millennial scale patterns and ecological implications, *Ecological Applications*, 21, 3211-3226.
- Hu, F. S., P. E. Higuera, J. E. Walsh, W. L. Chapman, P. A. Duffy, L. B. Brubaker, and M. L. Chipman (2010), Tundra burning in Alaska: linkages to climatic change and sea-ice retreat, *J. of Geophys. Res.*, 115, G04002 doi:10.1028/2009JG001270.
- Jandt, R. R., E. A. Miller, D. A. Yokel, M. S. Bret-Harte, C. A. Kolden, and M. C. Mack (2012), Findings of Anaktuvuk River Fire Recovery Study, 2007-2011, Bureau of Land Management, Fairbanks, AK http://arcticlcc.org/assets/products/ARCT2011-10/progress_reports/Anaktuvuk-River-Fire-StudyFINAL6-21-12.pdf.

Jones, B. M., C. A. Kolden, R. R. Jandt, J. Abatzoglou, F. Urban, and C. D. Arp (2009), Fire behavior, weather, and burn severity of the 2007 Anaktuvuk River tundra fire, North Slope, Alaska, *Arctic, Antarctic, and Alpine Research*, 41, 309-316 doi: 10.1657/1938-4246-41.3.309.

Jorgenson, M.T., and J. Grunblatt (2013), Landscape-level ecological mapping of northern Alaska and field site photography, Report prepared for the Arctic Landscape Conservation Cooperative, http://arcticlcc.org/assets/products/ALCC2011-06/reports/NorthernAK_Landscape_Mapping_Field_Photos_Final_RPT.pdf.

Jorgenson, M. T., Y. L. Shur, and E. R. Pullman (2006), Abrupt increase in permafrost degradation in Arctic Alaska, *Geophys. Res. Lett.*, 33, L02503 doi:10.1029/2005GL024960.

Kanevskiy, M., Y.L. Shur, D. Fortier, M. T. Jorgenson, and E. Stephani (2011), Cryostratigraphy of late Pleistocene syngenetic permafrost (yedoma) in northern Alaska, Itkillik River exposure, *Quaternary Research*, 75, 584-596.

Kasischke, E. S., and M. R. Turetsky (2006), Recent changes in the fire regime across the North American boreal region-spatial and temporal patterns of burning across Canada and Alaska, *Geophysical Research Letters*, 33, L09703 doi:10.1029/2006GL025677.

Krawchuk, M. A., M. A. Moritz, M-A. Parisien, J. Van Dorn, and K. Hayhoe (2009) Global Pyrogeography: the Current and Future Distribution of Wildfire, *PLoS ONE*, 4, e5102 doi:10.1371/journal.pone.0005102.

Mack, M. C., M. S. Bret-Harte, T. N. Hollingsworth, R. R. Jandt, E. A. G. Schuur, G. R. Shaver, and D. L. Verbyla (2011) Carbon loss from an unprecedented Arctic tundra wildfire, *Nature*, 475, 489-492 doi:10.1038/nature10283.

Mann, D. H., P. Groves, R. E. Reanier, M. L. Kunz (2010), Floodplains, permafrost, cottonwood trees, and peat: What happened the last time climate warmed suddenly in arctic Alaska, *Quaternary Science Reviews*, 29, 3812-3830 10.1016/j.quascirev.2010.09.002.

McGuire, A. D. et al. (2009), Sensitivity of the carbon cycle in the Arctic to climate change, *Ecol. Monogr.*, 79, 523–555 doi:10.1890/08-2025.1.

Miller, E. A. (2010), Basic statistics on North Slope tundra fires in Alaska, <http://www.frames.gov/rcs/12000/12510.html>.

Myers-Smith, I. H. et al. (2011), Shrub expansion in tundra ecosystems: dynamics, impacts and research priorities, *Environ. Res. Lett.*, 6, 045509.

Pfeiffer, M., Spessa, A., and J. O. Kaplan (2013), A model for global biomass burning in preindustrial time: LPJ-LMfire (v1. 0)., *Geoscientific Model Development*, 6, 643-685.

Racine, C. H., J. G. Dennis, and W. A. Patterson III (1985), Tundra fire regimes in the Noatak River Watershed, Alaska: 1956-83, *Arctic*, 38, 194-200.

Racine, C. H., L. A. Johnson, and L. A. Viereck (1987), Patterns of vegetation recovery after tundra fires in Northwestern Alaska, U.S.A., *Arctic and Alpine Research*, 19, 461-469.

Racine, C. H., J. L. Allen, and J. G. Dennis (2006), Long-term monitoring of vegetation change following tundra fires in Noatak National Preserve, Alaska Arctic Network of Parks Inventory and Monitoring Program, National Park Service Alaska Region Report no. NPS/AKRARC/NRTR-2006/02.

Randerson, J. T., Y. Chen, G. R. van derWerf, B. M. Rogers, and D. C. Morton (2012), Global burned area and biomass burning emissions from small fires, *J. Geophys. Res.*, 117, G04012, doi:10.1029/2012JG002128.

Reimer, P. J. et al. (2009), IntCal09 and Marine09 radiocarbon age calibration curves, 0–50,000 years cal BP, *Radiocarbon*, 51, 1111–1150.

Rocha, A. V. et al. (2012), The footprint of Alaskan tundra fires during the past half-century: implications for surface properties and radiative forcing, *Env. Res. Lett.*, 7, 044039 doi:10.1088/1748-9326/7/4/044039.

Sousa, W.P. (1984), The role of disturbance in natural communities, *Annual Review of Ecology and Systematics*, 15, 353-391.

Sturm, M., C. H. Racine, and K. Tape (2001), Increasing shrub abundance in the Arctic, *Nature*, 411, 546–547.

Tarnocai C., J. G. Canadell, E. A. G. Schuur, P. Kuhry, G. Mazhitova, and S. Zimov (2009), Soil organic carbon pools in the northern circumpolar permafrost region, *Global Biogeochem. Cycles*, 23, GB2023 doi:10.1029/2008GB003327.

Tape, K., M. Sturm, and C. H. Racine (2006), The evidence for shrub expansion in northern Alaska and the Pan-Arctic, *Global Change Biology*, 12, 686–702.

van der Werf, G. R. et al. (2010), Global fire emissions and the contribution of deforestation, savanna, forest, agricultural, and peat fires (1997–2009), *Atmos. Chem. Phys.*, 10, 11707-11735 doi:10.5194/acp-10-11707-2010, 2010.

Walker, D. A., and M. K. Reynolds (2011), An International Arctic Vegetation Database: A foundation for panarctic biodiversity studies CAFF Strategy Series Report nr 5, Conservation of Arctic Flora and Fauna, Akureyri, Iceland, 29 pp.

Walker, D. A., I. G. Alsos, C. Bay, N. Boulanger-Lapointe, A. L. Breen, H. Bültmann, T. Christiansen, C. Damgaard, F. J. A. Daniëls, S. Hennekens, M. K. Reynolds, P. C. Le Roux, M. Luoto, L. Pellisier, R. K. Peet, N.-M. Schmidt, L. Stewart, R. Virtanen, N. G. Yoccoz, and M. S. Wisz (2013), Rescuing valuable Arctic vegetation data for biodiversity models, ecosystem models and a Panarctic vegetation classification, *Arctic, InfoNorth*, 66, 133-137.

Walker, L. R., D. A. Wardle, R. D. Bardgett, and B. D. Clarkson, 2010, The use of chronosequences in studies of ecological succession and soil development, *Journal of Ecology*, 98, 725-736.

Wein, R. W. (1976), Frequency and characteristics of Arctic tundra fires, *Arctic*, 29, 213–222.

4.10 Figures

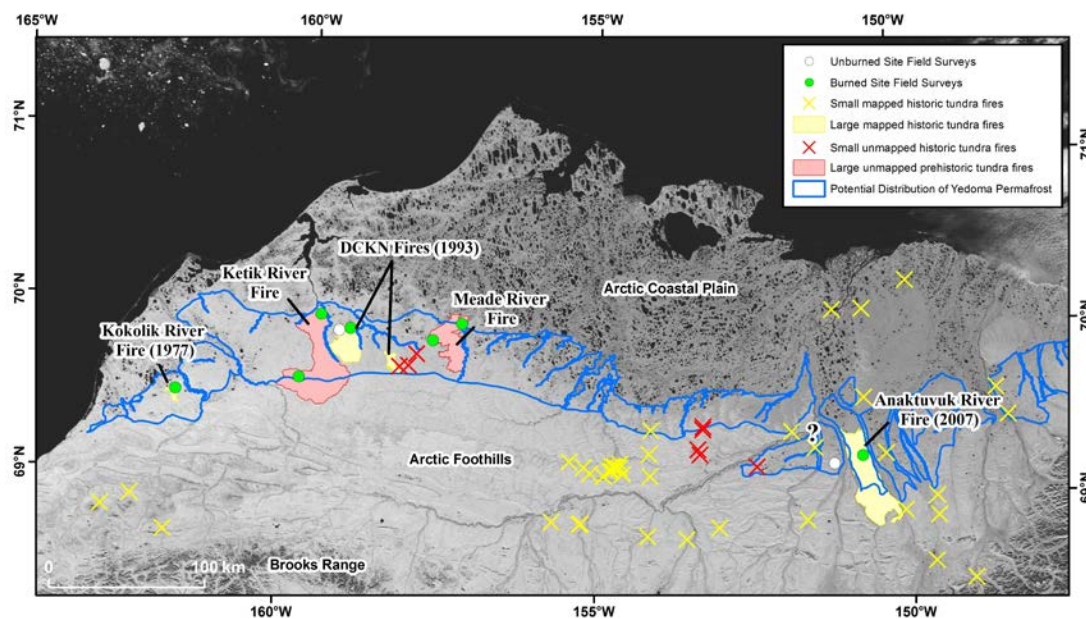


Figure 1: Fire distribution on the North Slope of Alaska. Regional map showing previously identified tundra fires, unrecognized tundra fire sites presented in this study, and field survey locations on the North Slope of Alaska. The blue polygon represents the likely distribution of Pleisto-cene-aged silt with high ice and carbon content (Yedoma) [Jorgenson and Grunblatt, 2013]. The question mark depicts the site shown in SOM figure 2.

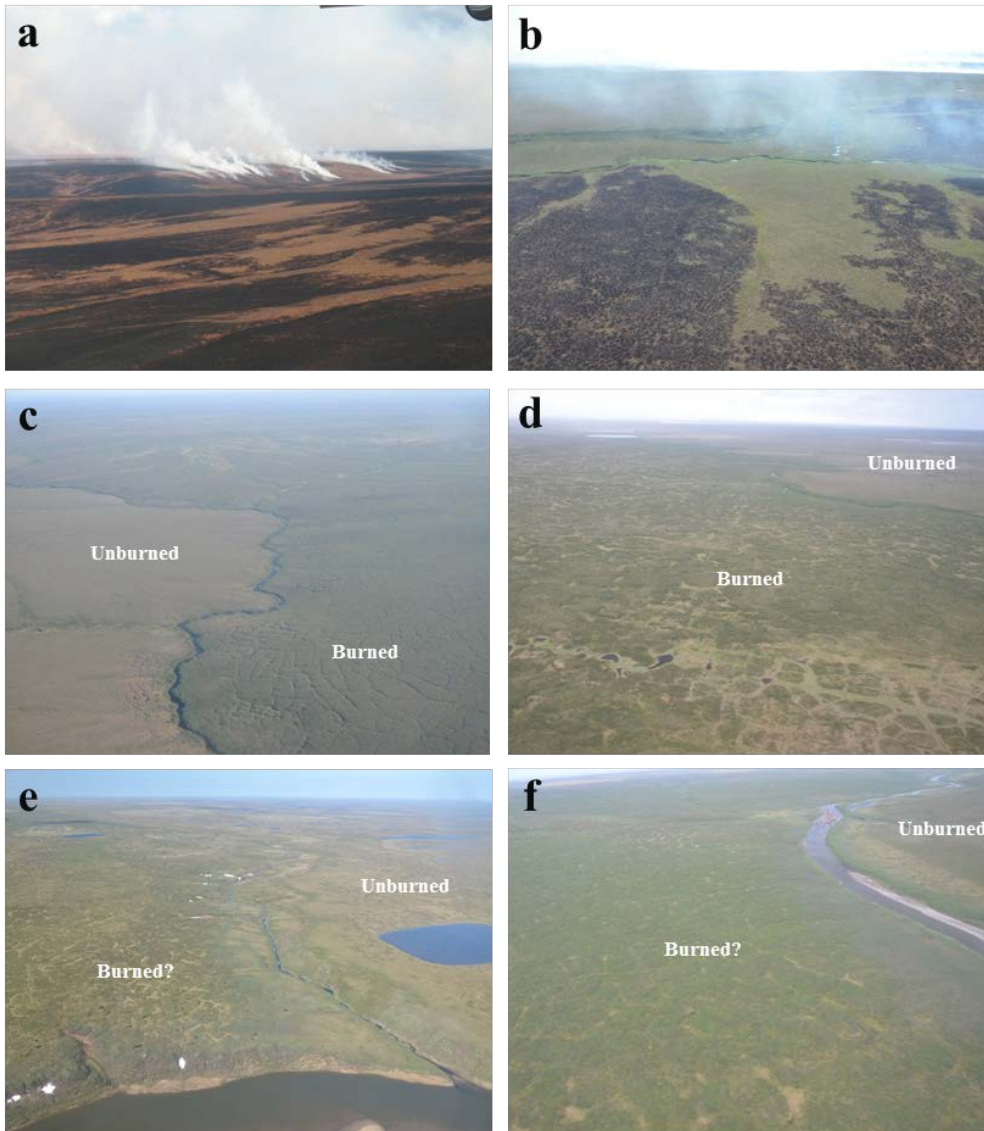


Figure 2: Oblique aerial photography of tundra fire sites. (a) The 2007 Anaktuvuk River fire showing the heterogeneous pattern associated with the burn, (b) the 2012 Kucher Creek fire showing a patchy burn pattern as well as a small stream prohibiting fire expansion, (c) the 1993 DCKN190 Fire showing an increase in landscape texture in the burned (right side of creek) versus unburned tundra (left side of creek), (d) the 1977 Kokolik River fire showing shrubbier tundra in the foreground (in burn) and typical graminoid tussock tundra in the background (outside burn), (e) the recently identified Meade River fire site, and (f) the recently identified Ketik River fire site.

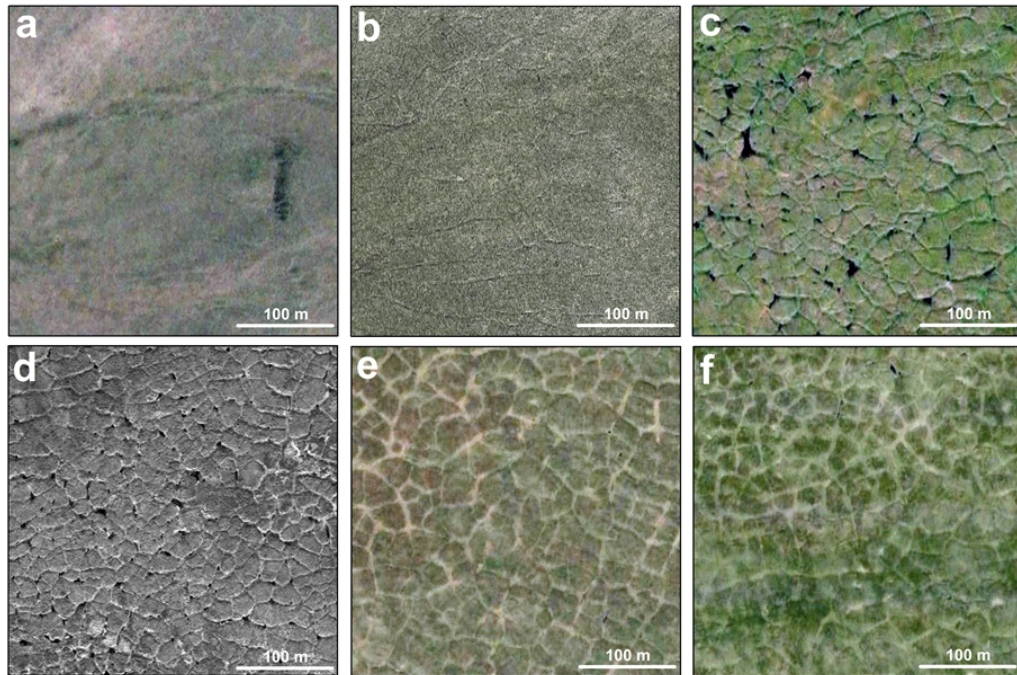


Figure 3: Increase in image texture following fire. High-resolution satellite images of upland tundra settings from (a) a site within the Anaktuvuk River fire prior to the burn, (b) the same site as in (a) four years after the fire, (c) the 1993 DCKN190 fire site, (d) the 1977 Kokolik River fire site, (e) the Meade River fire site, and (f) the Ketik River fire site.

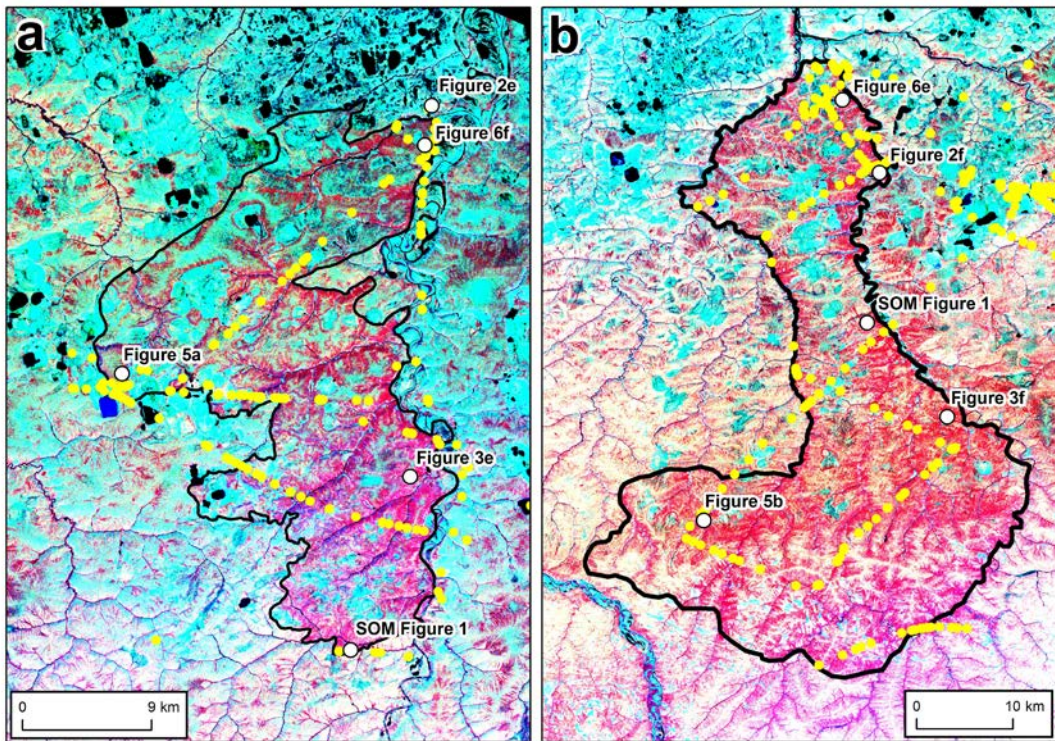


Figure 4: Enhanced Landsat images of the (a) Meade River and (b) Ketik River sites. The locations of survey sites mentioned in the text are marked with a white dot along with their corresponding figure number. The yellow dots represent the location of oblique geotagged photos taken during the aerial surveys in 2012.



Figure 5: Charred material preserved in soil column. Example of soil plugs taken from the (a) Meade River site and the (b) Ketik River site. Arrows depict charred horizon and smear tests shown in lower left.

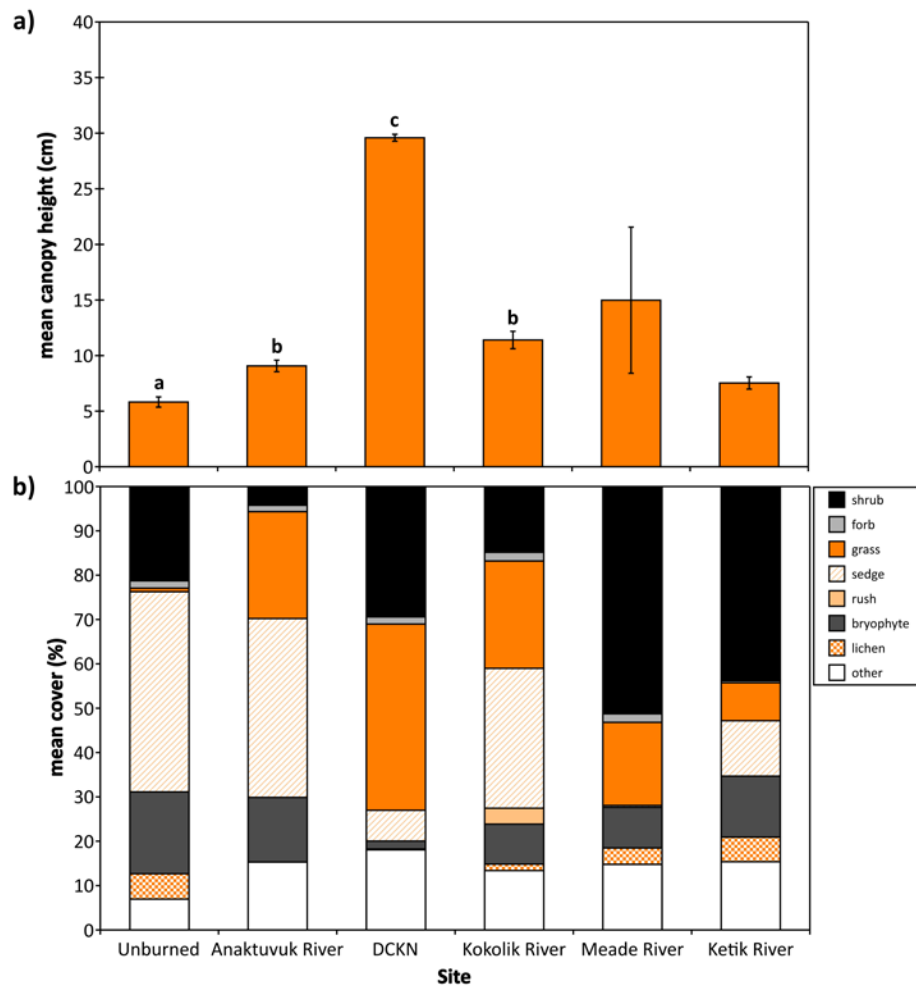


Figure 6: Difference in vegetation at burned and unburned sites. (a) Mean canopy height among unburned and burned tundra sites (ANOVA, $F_{3,9}=386.56$, $P < 0.0001$) and (b) the distribution of vascular plant functional types ($\chi^2=236.728$, d.f.=35, $P < 0.0001$). Bars in (a) show mean values and brackets denote associated standard errors and site means that differ significantly ($P < 0.05$) are indicated by a subscript. The x-axis is arranged from youngest to oldest fire event.

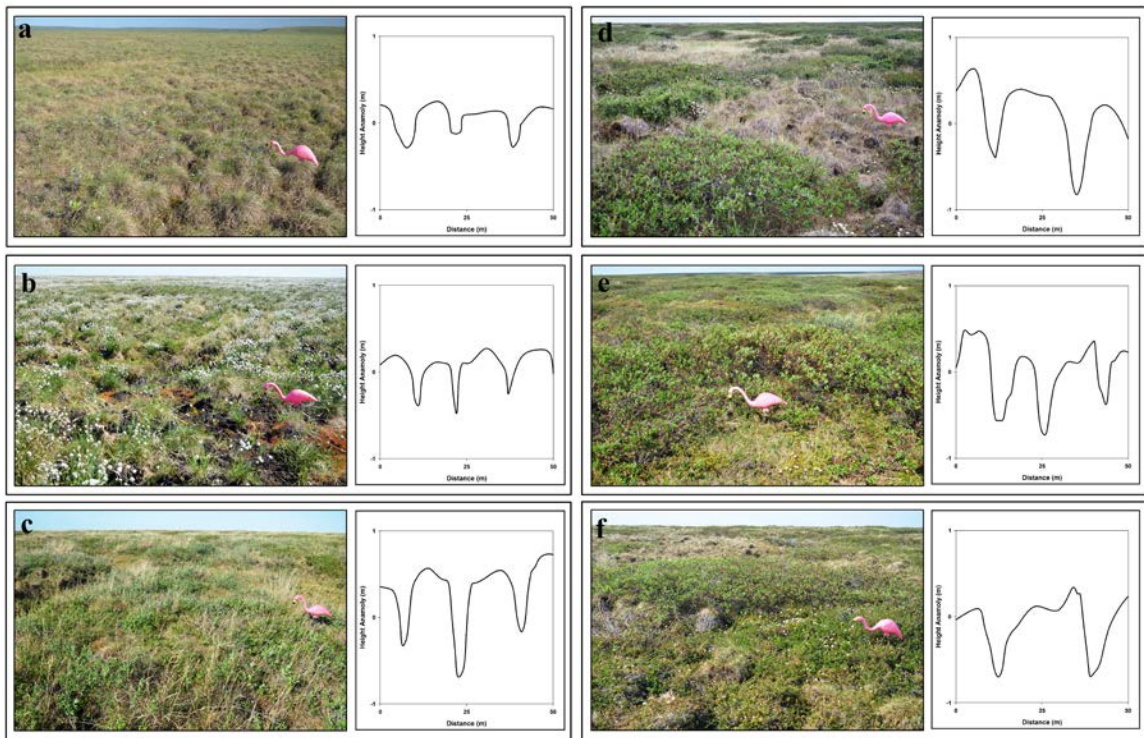


Figure 7: Ground-based surveys at burned and unburned sites. Field photos and DGPS survey data showing the vegetative and geomorphic expression of (a) an unburned site, (b) the 2007 Anaktuvuk River fire, (c) the 1993 DCKN190 fire, (d) the 1977 Kokolik River fire, (e) the Meade River fire, and (f) the Ketik River fire. The pink flamingo lawn ornament measures 50 cm from head to tail. All x-axes represent 50 m and all y-axes represent 2 m.

4.11 Tables

Table 1: Age control for Meade and Ketik fire sites. Results from radiocarbon dating of charred twig material found preserved in the soils at the previously unrecognized fire sites provided as a measured radiocarbon age, conventional radiocarbon age, 2- σ calibrated age, and the relative area under the distribution curve.

Laboratory Number	Field Site	Latitude (N)	Longitude (W)	Dated Material	^{14}C age ^a	1- σ error (\pm) ^b	$\delta^{13}\text{C}$ (‰) ^c	^{13}C -adjusted radiocarbon age ^d	1- σ error (\pm) ^b	2- σ Calibrated age range (cal yr AD) ^e	Relative area under distribution
Beta-327427	Meade	69° 55.8'	157° 44.3'	Charred Twig	70	30	-27.7	30	30	1695-1726	0.20
										1813-1838	0.14
										1842-1853	0.02
										1868-1873	0.01
										1876-1918	0.60
										1952-1954	0.03
Beta-336038	Ketik	69° 39.1'	159° 57.7'	Charred Twig	100	30	-27.5	60	30	1694-1727	0.24
										1812-1919	0.74
										1952-1954	0.02

^a Radiocarbon years before present where present is AD 1950

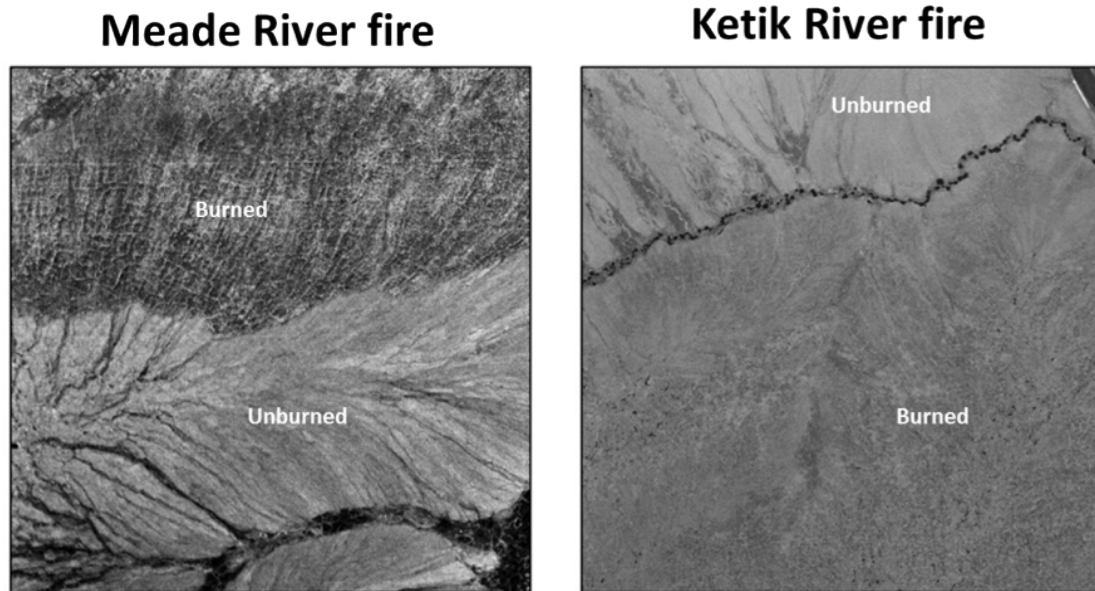
^b Quoted errors represent one relative standard deviation

^c Measured $^{13}\text{C}/^{12}\text{C}$ ratios ($\delta^{13}\text{C}$) were calculated relative to the PDB-1 standard

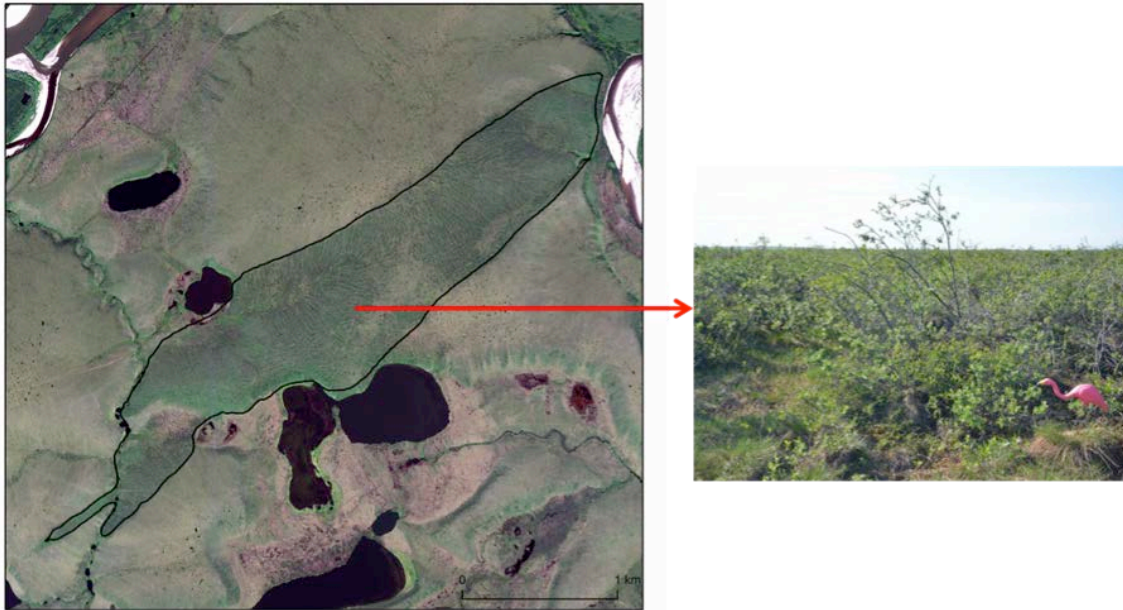
^d Represents the measured radiocarbon age corrected for isotopic fractionation and reported in years before present where present is AD 1950

^e Using Calib6 (Reimer et al., 2009) and the ^{13}C -adjusted radiocarbon age

4.12 Supporting online material



SOM Figure 1. Late-1940s aerial photography of fire sites. Late-1940s historic aerial photography of the Meade River and Ketik River sites showing that the increase in landscape texture was already apparent when the imagery was acquired. These images were used to rule out the possibility that these two events occurred after 1950.



SOM Figure 2. Likely tundra fire site near the Chandler River exhibiting the increase in texture in high resolution satellite imagery and a shrub-dominated vegetation community atypical of the upland tussock tundra community that lies outside the delineated perimeter (black polygon). Note standard pink flamingo lawn ornament for scale which measures 50 cm from head to tail. This site is shown in Figure 1 as the question mark.

SOM Table 1: Raw data table compiled from vegetation surveys. Raw data table showing species grouped by functional type (down) and listing transects and their localities sampled on the North Slope (across). Data are cover abundance (percentage). Species occurring on the transect that were not hit are indicated by an 'r' denoting these were rare species (cover << 1%). These data were used to compile Figure 7.

Taxa	Unburned				Burned									Undiscovered Burned					
	East		West		Anaktuvuk River (2007)			DCKN (1993)			Kokolik River (1977)			Meade River			Ketik River		
	1	2	3	4	5	6	7	8	9	10	11	12	13	14	15	16	17	18	19
Shrubs																			
<i>Andromeda polifolia</i>	1.23		1.08
<i>Arctous alpina</i>	.	0.89	r
<i>Betula nana</i>	6.17	2.68	5.38	4.29	2.60	r	r	0.50	.	.	4.49	10.53	5.88	5.00	.	20.21	5.19	.	13.43
<i>Cassiope tetragona</i>	2.47	2.68	4.30	r	.	.
<i>Dryas integrifolia</i>	.		1.08
<i>Empetrum nigrum</i>	.	0.89	0.65
<i>Rhododendron lapponicum</i>
<i>Rhododendron tomentosum</i> ssp. <i>decumbens</i>	8.64	1.79	5.38	7.14	.	r	.	0.87	.	0.96	1.12	.	3.92	20.00	9.76	3.19	11.69	12.33	4.48
<i>Rubus chamaemorus</i>	r	.	.	.	r	.	.	2.61	.	.	r	.	0.65	r	1.37
<i>Salix glauca</i>	22.77	20.72	36.54	r	3.19	.	.	.
<i>Salix niphoclada</i>	1.12
<i>Salix pulchra</i>	.	.	4.30	1.43	5.19	.	r	2.97	0.90	2.88	r	13.68	0.65	8.75	35.37	32.98	7.79	27.40	8.96
<i>Salix reticulata</i>	r
<i>Vaccinium uliginosum</i>	.	0.89	r	0.65
<i>Vaccinium vitis-idaea</i>	8.64	6.25	3.23	4.29	.	1.41	r	.	.	.	1.12	.	.	10.00	.	1.06	14.29	9.59	14.93
Forbs																			
<i>Artemisia tilesii</i>	r	.	0.96	.	4.21	r	r
<i>Bistorta plumosa</i>	.	r	1.08	.	r	r	r	r
<i>Chamerion angustifolium</i>	r	.	0.99	0.90	.	r	r	r
<i>Epilobium latifolium</i>	r
<i>Parrya nudicaulis</i>	r	.	.	.
<i>Pedicularis lapponica</i>	1.23
<i>Petasites frigidus</i>	r	r	.	3.48	0.50	.	r	r	.	r	.	.	r	.	.
<i>Pinguicula villosa</i>	r
<i>Pyrola grandiflora</i>	.	.	1.08	0.50	r	2.44
<i>Pyrola secunda</i> var. <i>obtusata</i>	r
<i>Saussurea angustifolia</i>	.	r	2.15	.	.	.	r	0.50	1.06	.	.	.
<i>Saxifraga cernua</i>	0.65
<i>Saxifraga species</i>	r
<i>Stellaria longipes</i> taxon <i>edwardsii</i>	0.50	1.22	1.06	.	.	.
<i>Stellaria longipes</i>	r	.	.	0.87	.	.	.	1.05	1.37
<i>Stellaria monantha</i>	r
<i>Taraxacum</i> cf. <i>alaskanum</i>	r
<i>Valeriana capitata</i>	.	.	1.08

SOM Table 1 continued

<i>Sphagnum rubellum</i>	1.23
<i>Sphagnum warnstorffii</i>	.	1.79	.	2.86
<i>Sphenolobus minutus</i>	r	.	r	r
Lichens																				
<i>Cetraria islandica</i>	.	r
<i>Cladonia amaurocraea</i>	1.23	0.89	1.08	1.12	.	2.61	.	.	.	6.49	1.37	1.49	.	.	.
<i>Cladonia arbuscula</i> s. lat.	r	2.68
<i>Cladonia cenotea</i>	r	.	.	.	r
<i>Cladonia cornuta</i>	5.00	1.22
<i>Cladonia cyanipes</i>	r
<i>Cladonia gracilis</i>	r	.	0.65
<i>Cladonia rangiferina</i>	3.70	.	r	r	.	1.49	.	.	.
<i>Cladonia stygia</i>	.	.	.	1.43
<i>Cladonia uncialis</i>	.	2.68	1.25
<i>Dactylina arctica</i>	.	0.89	1.08
<i>Dactylina ramulosa</i>	.	r
<i>Flavocetraria cucullata</i>	2.47	1.79	r	r
<i>Flavocetraria nivalis</i>	.	r
<i>Masonhalea richardsonii</i>	.	.	r
<i>Peltigera aphthosa</i>	.	0.89
<i>Peltigera canina</i>	0.50
<i>Peltigera leucophlebia</i>	2.50	.	1.06	.	.	1.49	.
<i>Peltigera neckeri</i>	1.30
<i>Peltigera rufescens</i>	.	.	1.08
<i>Peltigera scabrosa</i>	2.99
<i>Peltigera species</i>	r
<i>Sphaerophorus globosus</i>	.	r	r
<i>Thamnolia vermicularis</i> ssp. <i>subuliformis</i>	.	r	1.08
Other																				
Down dead wood	1.74
Litter	7.41	5.36	6.45	8.57	16.88	16.90	10.43	11.39	20.72	22.12	10.11	18.95	11.11	10.00	19.51	12.77	11.69	15.07	19.40	

Chapter 5: Quantifying landscape change in an arctic coastal lowland using repeat airborne LiDAR⁴

5.1 Abstract

Increases in air, permafrost, and sea-surface temperature, loss of sea-ice, the potential for increased wave energy, and higher river discharge may all be interacting to escalate erosion of arctic coastal lowland landscapes. Here we use airborne Light Detection and Ranging (LiDAR) data acquired in 2006 and 2010 to detect landscape change in a 100 km² study area on the Beaufort Sea coastal plain of northern Alaska. We detected statistically significant change (99% confidence interval), defined as contiguous areas (>10 m²) that had changed in height by at least 0.55 m, in 0.3% of the study region. Erosional features indicative of ice-rich permafrost degradation were associated with ice-bonded coastal, river, and lake bluffs, frost mounds, ice-wedges, and thermo-erosional gullies. These features accounted for about half of the area where vertical change was detected. Inferred thermo-denudation and thermo-abrasion of coastal and river bluffs likely accounted for the dominant permafrost-related degradational processes with respect to area (42%) and volume (51%). More than 300 thermokarst pits significantly subsided during the study period, likely as a result of storm surge flooding of low-lying tundra (< 1.4 m asl) as well as the lasting impact of warm summers in the late-1980s and mid-1990s. Our results indicate that repeat airborne LiDAR can be used to detect

⁴ Jones, B. M., J. M. Stoker, A. E. Gibbs, G. Grosse, V. E. Romanovsky, T. A. Douglas, N. E. M. Kinsman, and B. R. Richmond (*In Press*), Quantifying landscape change in an arctic coastal lowland using repeat airborne LiDAR, *Environmental Research Letters*.

landscape change in arctic coastal lowland regions at large spatial scales over sub-decadal time periods.

5.2 Introduction

Recent reductions in Arctic sea ice extent have been well documented (Stroeve *et al* 2012). Reduced sea ice cover, combined with earlier seasonal thaw and later winter freeze-up results in increased effective fetch for wind-wave generation and a longer time period of open water for storms to impact arctic coastal lowlands (Overeem *et al* 2011). Increases in river discharge may also be enhancing erosion along riverine corridors, although pan-Arctic evaluations of river discharge reveal contrasting regional trends (McClelland *et al* 2006). In addition, warming of terrestrial permafrost (Romanovsky *et al* 2010, Smith *et al* 2010) may lead to thermokarst development and other thaw related phenomena in ice-rich permafrost terrain (Jorgenson *et al* 2006). Thus, terrestrial, aquatic, and marine environmental changes occurring in the Arctic may be interacting to increase erosion of coastal lowland landscapes which in turn may lead to mobilization of carbon previously frozen in permafrost (Jorgenson and Brown 2005, Lantuit *et al* 2009).

Thus far, most remote sensing studies focused on identifying landscape change of near surface permafrost terrain in arctic lowland regions primarily rely on 2-dimensional measurements to quantify lateral rates of change for thermokarst lakes (Arp *et al* 2011, Jones *et al* 2011), thermokarst lake drainage (Hinkel *et al* 2007; Marsh *et al* 2009), retrogressive thaw slump headwall retreat (Lantz and Kokelj 2008, Lantuit and Pollard 2008), thermo-erosional gully formation and expansion (Fortier *et al* 2007), erosion of coasts by block collapse and mass wasting (Jones *et al* 2009), and degradation of ice

wedges and thermokarst pit formation (Jorgenson *et al* 2006). A few remote sensing studies in lowland permafrost terrain have targeted three-dimensional landscape change relying on Interferometric Synthetic Aperture Radar (InSAR) techniques (e.g. Liu *et al* 2010). While InSAR is capable of capturing broad regional dynamics of land surface heave and subsidence the method is limited in its applicability for detecting thermokarst features (Short *et al* 2011). In addition, stereo-photogrammetric change detection studies have been limited in nature and spatial extent in lowland permafrost regions (Lantuit and Pollard 2005, Günther *et al* 2013), whereas their use is more widespread in mountainous permafrost regions (e.g. Kääh 2008).

The ability to detect vertical change in permafrost regions is critical to advancing our understanding of landscape evolution and carbon cycling. Light Detection and Ranging (LiDAR) measurements provide a powerful method for imaging the spatial and vertical intricacies of the landscape (e.g. Ritchie 1995). Successful applications of airborne LiDAR include the study of stream morphology (e.g. Snyder, 2009), mapping coastline morphologic change (e.g. White and Wang 2003), measuring volumetric change in sand dunes (e.g. Woolard and Colby 2002), landslide monitoring (e.g. Glenn *et al* 2006), and topographic change of periglacial mountainous terrain (Fischer *et al* 2011). However, airborne LiDAR data has seldom been used to characterize periglacial lowland regions (Marsh *et al* 2009, Hubbard *et al* 2013). To date, an airborne LiDAR change detection study for coastal lowland permafrost terrain has not been attempted to the best of our knowledge.

In this study, we contrast airborne LiDAR data collected in July 2006 and July 2010 for a 100 km² area on the central Beaufort Sea coastal plain in northern Alaska. We use repeat LiDAR to test whether this approach is capable of detecting geomorphic changes occurring in arctic coastal lowland landscapes, particularly those associated with thermokarst and other thaw-related processes. We also present trends in mean annual air temperature, thawing degree days (TDD), near surface permafrost temperature, and active layer thickness for monitoring sites in close proximity to our study region. In addition, we provide an example of how repeat LiDAR data may be used regarding questions of carbon mobilization from permafrost terrain. These inquiries align with the increasing interest in the spatial and temporal dynamics of permafrost-dominated landscapes from a wide range of science and engineering disciplines (landscape ecology, hydrology, civil engineering, and biogeochemistry) and will be helpful in addressing land management issues such as infrastructure planning, habitat mapping, and landscape evolution in the Arctic.

5.3 Study area

The study area is located on the Beaufort Sea coastal plain of northern Alaska and was selected due to existing, overlapping coverage of airborne LiDAR data acquired in July 2006 and July 2010. Repeat LiDAR data were available for a nearly 100 km² land area along the coast from the Sagavanirktok River delta in the west to Point Thomson in the east, with an inland coverage of 2 to 4 km (figure 1). The study region contains thermokarst and other thaw-related landscape features as well as nearshore coastal and fluvial morphology (figure 2). The backshore lithology consists of ice-cemented, pebbly

silty sand, with 70-80% volumetric ground-ice content, and 10-20% by volume of ice-wedge ice (Jorgenson and Brown 2005; Kanevskiy *et al* 2013). Sea ice, predominantly landfast ice, is typically present along the coast for 8 to 9 months of the year. The astronomical tides in this region are typically less than 0.2 m, however, atmospheric and oceanic conditions have led to storm surges as high as 1.4 m above mean sea level during the last two decades (Sultan *et al* 2011). Long-term mean annual coastal erosion rates in our study region are 0.9 m/yr and maximum observed rates are 7.0 m/yr (Jorgenson and Brown 2005, Gibbs *et al* 2011), and there has been a doubling of the mean decadal-scale coastal erosion rate since the 1980s (Ping *et al* 2011). Estimates of total organic carbon (OC) in the upper 1 m of the landscape range from 56-66 kgOC/m² at particular sample sites (Ping *et al* 2008) and estimates of carbon mobilization in our study area as a result of coastal erosion range from 3.2-7.1 Gg/yr (Jorgenson and Brown 2005).

The study area also encompasses existing and planned oil and gas infrastructure. Development within the study area primarily consists of commercial resource extraction and resource transportation infrastructure emplaced by the oil and gas industries (e.g. drilling pads, pipelines, airstrips and docks). There are approximately eight known exploratory or production well sites within the bounds of the study area, the largest being the Badami oil field. Standard construction methods for development in this area utilize gravel pads to thermally buffer the underlying permafrost. These gravel features provide an excellent location for validating the comparability in the two LiDAR datasets as their vertical motion should be near zero (figure 3).

5.4 Methods

5.4.1 Airborne LiDAR data

LiDAR was collected in the summers of 2006 and 2010 by Aero-metric Inc. The 2006 data were delivered as classified point clouds in NAD 83 Alaska State Plane Zone 3 in feet, with elevations referenced to Geoid99 in US Survey feet. The 2010 data were delivered as last return point clouds in NAD 83 UTM zone 6N in meters, with elevations referenced to the GRS 1980 Ellipsoid. The 2006 data were transformed to match the horizontal and vertical units and Ellipsoid reference frame of the 2010 data. Nominal point spacing for the data was on average one point per 1-1.5 m for both datasets. Both last return, point cloud datasets were clipped to their overlapping extents, and then converted to surfaces, first by using Terrascan (version 12)® and a Triangulated Irregular Network (TIN) approach. The TIN connects LiDAR returns by a set of contiguous, non-overlapping, Delaunay triangles. The elevations between each triangle vertex are interpolated as definitions of planes and thus together construct a surface. These surfaces were then exported to lattice datasets, and finally converted to 1.5 m raster grids to be used in a GIS.

The two datasets were differenced to identify potential changes in elevation between 2006 and 2010. The reported vertical accuracies of the data were 0.12 m (2006 dataset) and 0.14 m (2010 dataset) RMSE. To determine if there were any errors introduced in the conversion/transformation process we compared elevations along transects that likely represented stable terrain features associated with oil infrastructure gravel pads between the two acquisition dates. The difference in elevation along the

unvegetated land surfaces were less than ± 0.10 m (figure 3). However to be conservative in our detection of change, and with the realization that comparison of the data acquired over gravel pads represent a best case scenario, we used the RMSE of the individual datasets to calculate (equation 1) a threshold that describes the minimum difference between both datasets that meets a significant elevation change at the 99% confidence level or those pixels exceeding three standard deviations (Jaw 2001):

$$3 * \text{SQRT}((2006 \text{ vertical accuracy})^2 + (2010 \text{ vertical accuracy})^2) = 0.55 \text{ m} \quad (1)$$

In the surface differenced raster, we considered any pixel with a height difference residual above or below 0.55 m as a statistically significant change in elevation. These areas were reclassified as <significant increase> or <significant decrease> per pixel. Objects demonstrating significant increases or decreases in elevation were extracted from the dataset by selecting areas that had at least five contiguous pixels of significant change. This resulted in a minimum object size greater than 10 m² and helped minimize potential errors associated with raster grid creation and horizontal positional accuracy (± 0.60 m). While there were detectable changes of smaller amplitude in the difference image we did not consider these in our further assessment. In addition, all changes interpreted as indicating water level differences as well as a result of human-caused landscape changes, such as from infrastructure construction or material movement, were excluded from further analysis.

5.4.2 Geomorphic classification of landscape change units

Objects that represented a statistically significant change in elevation were manually classified as one of 13 categories via visual inspection of the LiDAR imagery. Nine of

these classes represented land subsidence or loss and four represented land uplift or deposition. Objects that were indicative of subsidence included thermokarst and thaw-related features associated with ice-bonded coastal, river, and lake bluffs, frost mounds, ice-wedges, and thermo-erosional gullies. Non-thaw related erosional features included beaches and spits, river bars and deltas, and sand dunes. Areas that represented landscape uplift or deposition included permafrost heave features and deposition associated with beaches and spits, river bars and deltas, and sand dunes (often in close proximity to an eroding feature).

5.4.3 Air and permafrost temperature and active layer thickness measurements

The West Dock (WD) and Deadhorse (DH) Thermal State of Permafrost (TSP) permafrost observatories were established in the late 1970s (Osterkamp 2003). The WD TSP site is located 0.3-0.4 km from the coast and the DH TSP site is located 15 km from the coast (figure 1). Vegetation at each site consists of wet non-acidic tundra with a continuous cover of graminoid and moss species and wet and moist non-acidic tundra composed of graminoid-moss tundra and graminoid, prostrate-dwarf-shrub, moss tundra, respectively (Walker *et al* 2008). In 1986, a string of calibrated thermistors attached to a data logger were installed at each site (Osterkamp 2003, Romanovsky and Osterkamp 1995). In 1997, the measuring systems at each site were upgraded with new calibrated thermistor strings (MRC thermistor string) and Campbell Scientific data loggers (Romanovsky *et al* 2003). The old and new measuring systems were run concurrently for two years and differences in the temperature readings obtained from the two measuring systems at the same depth were typically within 0.2°C. Mean annual ground temperature

at a depth of 70 cm for the time period of 1987-2010 was calculated using the daily-averaged records from the WD and DH TSP sites. In 1996, a one hectare grid was established at each permafrost observatory to measure active layer thickness. Measurements were conducted every 10 m in accordance with the Circumpolar Active Layer Monitoring (CALM) program protocol (Brown *et al* 2000). To derive mean annual air temperature trends and TDD (based on 0°C) we used data from the Deadhorse airport climate station (figure 1). This station has been in operation since 1973, however due to data continuity issues we only present data for the period 1983 to 2010. These two permafrost monitoring sites and the climate station are considered representative of conditions within the repeat LiDAR study area.

5.5 Results

Comparison between the 2006 and 2010 LiDAR datasets revealed that 0.3% (by area) of the landscape experienced a statistically significant change in elevation (> 0.55 m) over the four year period. A total of 1,718 discrete objects (>10 m²) with significant change were identified. Changes in elevation were classified by geomorphic unit where the most likely mechanism of change was inferred to be: thaw slumping (figure 4a), coastal bluff erosion (figure 4b), river bluff erosion, thermokarst lake expansion, thermokarst pit subsidence (figure 4c), thermo-erosional gully erosion, permafrost heave, beach/spit erosion/deposition, delta/river bar erosion/deposition, and sand dune erosion/deposition (table 1). Coastal bluff erosion, thermokarst pit subsidence, and beach/spit erosion accounted for 66% of the identified objects. Thaw slumps, thermokarst lake expansion, river bluff erosion, thermo-erosional gullies, delta/river bar erosion, and sand dune

blowouts accounted for the remainder of the land lowering/loss. Beach/spit deposition accounted for 82% of the significant increase in surface elevation; whereas heave features, delta/river bar deposition, and sand dune accumulation accounted for the remainder of the detectable increase in the land surface elevation.

The largest individual, contiguous erosional objects by mean area were coastal bluffs (360 m²), beaches/spits (295 m²), and expanding thermokarst lake margins (115 m²). All other erosional and depositional objects had a mean surface area of less than 100 m². Coastal bluff erosion accounted for 40% of the total area where elevation changes were observed and beach spit erosion accounted for 43%. Thermokarst pit subsidence, river bluff erosion, and delta/river bar erosion each accounted for 2% of the area with observed elevation change. All other erosional features accounted for less than 1% of the total detectable surface area change. In terms of vertical change, coastal bluffs (4.4 m), river bluffs (3.8 m), beaches/spits (2.6 m), and thermokarst lake bluffs (2.4 m) accounted for objects with the greatest maximum change in elevation. Volumetrically, coastal bluff erosion accounted for 51% and beach/spit erosion 47% of the detectable changes. Beach/spit deposition accounted for 1.5% and all other features were equal to or less than 0.1% of the volume change.

5.6 Discussion

5.6.1 Airborne LiDAR change detection

Our results indicate that repeat airborne LiDAR measurements provide a straightforward, readily applied tool for quantifying landscape change in arctic coastal lowland regions. Comparison of the two LiDAR datasets revealed that 0.3% of the landscape area

experienced a significant change in elevation between 2006 and 2010 that resulted from thaw and non-thaw related processes. Thermokarst or thaw-related landscape features associated with ice-bonded coastal, river, and lake bluffs, thermokarst pits, thaw slumps, and thermo-erosional gullies accounted for 46% of the change in area over the four year study period and more than half of the significant change (56%) resulted from erosion and deposition associated with beach and spit deposits, riverine and deltaic flats, and sand dunes. These short-term landscape dynamics are likely a result of a combination of factors related to both natural processes and changes in the terrestrial, aquatic, and marine controls on the region.

Detailed examples of features detected in the study area include frost mound degradation (figure 4a); coastal bluff erosion, thermo-erosional gully expansion, and upland ice-wedge degradation (figure 4b); and lowland ice wedge degradation and thaw pit formation (figure 4c). Comparison between the 2006 and 2010 LiDAR data for the frost mound shows the excellent agreement (typically ± 0.15 m) between the two datasets for a vegetated and sloping surface that experienced a minimal change in height. Degradation or slumping of the eastern margin of the feature accounted for quantifiable change. In the example given in figure 4b, the ~4 m high bluff-face migrated 13 m inland over the four year study period. Also, evident in this example is an overall lower tundra relief in 2010 compared to 2006. Tundra lowering in this example did not meet our minimum threshold for change detection however, a consistent decrease in the elevation is visible in the plotted data that could be a result of top down permafrost thaw and soil consolidation. This general pattern of tundra relief lowering is also evident in

figure 4c for which we also detected a number of degrading ice wedges. The changes evident in this example may be a result of frequent inundation of the terrain during storm surges (Sultan *et al* 2011) which may lead to degradation of the ice-rich permafrost and degradation of ice wedges (figure 2b). With more local ground control statistically significant changes in elevation could be refined to capture these more subtle surface changes.

5.6.2 Factors contributing to landscape change

Arctic coastal lowland regions are particularly vulnerable to change given the interaction of atmospheric, terrestrial, aquatic, and marine influences on landscape configuration. Thermokarst and other thaw-related landscape features are driven by either local or regional disturbances. Jorgenson *et al* (2006) noted an abrupt increase in ice wedge degradation and thermokarst pit formation on the Beaufort Sea coastal plain that was attributed to an increase in TDD in the late 1980s and throughout the 1990s. A compilation of TDD from 1983 to 2010 for the Deadhorse climate station shows that the TDD in 2006, 2008, and 2010 exceeded the ~30 year average (figure 5). In addition, the 2006 to 2010 time period experienced some of the highest combined, continuous mean annual and mean summer temperatures over the course of the record for the Deadhorse climate station. No individual year rivaled the number of TDD that occurred in 1989, 1995, or 1998, which Jorgenson *et al* (2006) attributed to the widespread formation of thermokarst pits. It should be noted however that the warm summers in the late-1980s and mid-1990s could also be responsible for some of the observed increase in pit formation in our study region between 2006 and 2010, as the thermokarst pits that likely

formed during the 1990s have continued to subside. A recent analysis of thermokarst pit formation over a 60 year period in the Prudhoe Bay oil fields indeed shows a substantial increase in thermokarst pit formation between 1990 and 2001 that has continued through 2010 (Raynolds *et al* In Review).

Mean annual air temperature and the temperature of the ground as measured at a depth of 70 cm have warmed in the study region during the past ~20 to ~30 years, respectively (figure 5 and 6a). Interestingly, there is a mismatch between these warming trends and the trend in active layer thickness (figure 6b). This lack of coherence may be explained by the thaw of ice-rich permafrost and settlement of the ground surface as excess ice melts and the soil consolidates. Liu *et al* (2010) measured ground deformation using InSAR from 1992 to 2000 in this region and found that seasonal vertical displacements occurred as a result of freezing and thawing of the ground surface but that there was a secular subsidence of the land surface on the order of 1-4 cm/decade. Ground based studies on the Beaufort Coastal Plain from 2001 to 2006 indicate that 2.0 cm/yr of subsidence occurred and that when combined with mechanical probing measurements of the active layer that there was an increase in the “true” thaw depth (Streletskiy *et al* 2008). Thus, while general ground subsidence was not detected due to our conservative measure of change some of the lowering of the landscape observed in the data outside our defined level of confidence may indeed be a result of top down permafrost thaw.

The Alaskan Beaufort Sea coast has experienced varying levels of increased rates of erosion since the 1950s (Jones *et al* 2009, Gibbs *et al* 2011, Ping *et al* 2011). Factors responsible for this likely include loss of sea ice, warming ocean temperatures, and an

increase in total wave energy (Overeem *et al* 2011). While no comprehensive studies on river discharge or river bluff erosion exist in the study region, Arctic wide assessments indicate varying degrees of changes to river discharge (McClelland *et al* 2006) which may be impacting erosion of river bluffs. These changes are likely interacting to increase the effectiveness of thermal erosion and thermal abrasion of coastal and river bluffs in our study area. These processes likely accounted for the dominant permafrost-related degradational processes with respect to area (42%) and volume (51%) in the study region. In addition, areas lower than 1.4 m relative to mean sea level have been inundated during storm surges over the past two decades (Sultan *et al* 2011). Two of the ten highest storm surges between 1993 and 2010 occurred during our study period and all but one occurred between 2000 and 2010. Inundation of the low-lying coastal zone in our study area has likely contributed to the formation of thermokarst pits, with 60% of the observed change associated with these features below this approximate elevation (figure 4c). These inundation events may have also contributed to some of the general land lowering along the low-lying coastal zone that was observed in the data but outside our defined level of confidence.

5.6.3 Organic carbon mobilization

Estimates of total organic carbon in the upper 1 m of the studied landscape range from 56-66 kg OC/m² at sample sites located in the study region (Ping *et al* 2008). Based on these estimates, the loss of land between 2006 and 2010 along coast and river bluffs may have mobilized 1.8-2.1 Gg/yr. However, given our conservative estimates of quantifiable change this number should be viewed as a minimum estimate since long-term estimates

of carbon flux from this coastal stretch range from 3.0 to 7.0 Gg/yr (Jorgenson and Brown 2005). This exercise simply illustrates a basic type of analysis for carbon-related studies in permafrost terrain where repeat airborne LiDAR surveys have been acquired.

5.7 Conclusion

We compared airborne LiDAR data from 2006 and 2010 and demonstrated that it is possible to detect and characterize a number of thaw-related and non-thaw-related landscape changes occurring in arctic coastal lowlands. Erosion of ice-bonded coastal and river bluffs, thaw slumping, thermokarst lake expansion, thermokarst pit subsidence, and thermo-erosional gully expansion indicated ice-rich permafrost degradation and accounted for nearly half of the area and half of the volume change that occurred over the four year study period. Erosion and deposition associated with beach and spit deposits, riverine and deltaic flats, and sand dunes accounted for the majority of the remaining significant landscape change. Our study demonstrates the utility of assessing landscape change in an arctic coastal lowland with repeat airborne LiDAR data, in particular for spatially small but widespread permafrost thaw-related processes. We hope that this study will encourage the collection of repeat LiDAR data in other permafrost terrain.

5.8 Acknowledgements

Funding for this research was primarily provided by the U.S. Geological Survey – Alaska Regional Directors Office, Alaska Science Center, the Earth Resource and Observation Science Center, the National Geospatial Program, and the Coastal and Marine Geology Program. Additional support was provided by the Arctic Landscape Conservation Cooperative and GG was supported by NASA grant #NNX08AJ37G. TAD was

supported by funding from the Strategic Environmental Research and Development Program (SERDP) Project RC-2110. We kindly thank Stephan Gruber, Carl Markon, and an anonymous reviewer for their thoughtful and thorough critique of this manuscript. Any use of trade, product, or firm names is for descriptive purposes only and does not imply endorsement by the U.S. Government.

5.9 References

Arp C D, Jones B M, Urban F E and Grosse G 2011 Hydrogeomorphic processes of thermokarst lakes with grounded ice and floating ice regimes on the Arctic coastal plain, Alaska *Hydrological Processes* **25** 2422-2438

Brown J, Hinkel, K M and Nelson F E 2000 The Circumpolar Active Layer Monitoring (CALM) program: Research Designs and Initial Results *Polar Geography* **24** 163-258

Fischer L, Eisenbeiss H, Kääb A, Huggel C and Haeberli W 2011 Monitoring topographic changes in a periglacial high-mountain face using high-resolution DTMs, Monte Rosa East Face, Italian Alps *Permafrost Periglacial Processes* **22** 140–152

Fortier D, Allard M and Shur Y 2007 Observation of rapid drainage system development by thermal erosion of ice wedges on Bylot Island, Canadian Arctic Archipelago *Permafrost and Periglacial Processes* **18** 229-243.

Gibbs A E and Richmond B M 2009 Oblique aerial photography of the Arctic coast of Alaska, Nulavik to Demarcation Point, August 7-10, 2006 *U.S. Geological Survey Data Series* 436 <http://pubs.usgs.gov/ds/436/>

Gibbs A E, Harden E L, Richmond B M and Erikson L H 2011 Regional shoreline change and coastal erosion hazards in Arctic Alaska, in Wallendorf, L.A., Jones, C., Ewing, L, and Battalio, B. *Proceedings of the Solutions to Coastal Disasters Conference ASCE* 258-272

Glenn N F, Streutker D R, Chadwick D J, Thackray G D and Dorsch S J 2006 Analysis of LiDAR-derived topographic information for characterizing and differentiating landslide morphology and activity *Geomorphology* **73** 131-148

Günther F, Overduin P P, Baranskaya A, Opel T and Grigoriev M N 2013 Observing Muostakh Island disappear: erosion of a ground-ice-rich coast in response to summer

warming and sea ice reduction on the East Siberian shelf *The Cryosphere Discussions* **7** 4101-4176

Hinkel K M, Jones B M, Eisner W R, Cuomo C J, Beck R A and Frohn R 2007 Methods to assess natural and anthropogenic thaw lake drainage on the western Arctic coastal plain of northern Alaska *Journal of Geophysical Research* **112** F02S16.

Hubbard S S *et al* 2013 Quantifying and relating land-surface and subsurface variability in permafrost environments using LiDAR and surface geophysical datasets *Hydrogeology Journal* **21** 149-169

Jaw J 2001 Statistics-based fusion of terrain data sets and change detection in: Proceedings, 22nd Asian Conference on Remote Sensing, Singapore, November 5-9, 2001, Centre for Remote Imaging, Sensing and Processing, National University of Singapore, Singapore, 6 p., URL <http://www.crisp.nus.edu.sg/~acrs2001/pdf/278JAW.pdf>

Jones B M, Arp C D, Jorgenson M T, Hinkel K M, Schmutz J A and Flint P L 2009 Increase in the rate and uniformity of coastline erosion in Arctic Alaska *Geophysical Research Letters* **36** L03503

Jones B M, Grosse G, Arp C D, Jones M C, Anthony K W and Romanovsky V E 2011 Modern thermokarst lake dynamics in the continuous permafrost zone, northern Seward Peninsula, Alaska *Journal of Geophysical Research* **116** G00M03

Jorgenson M T and Brown J 2005 Classification of the Alaskan Beaufort Sea Coast and estimation of carbon and sediment inputs from coastal erosion *Geo-Marine Letters* **25** 69-80

Jorgenson M T, Shur Y L and Pullman E R 2006 Abrupt increase in permafrost degradation in Arctic Alaska *Geophysical Research Letters* **33** L02503

Kääb A 2008 Remote sensing of permafrost-related problems and hazards. *Permafrost Periglacial Processes* **19** 107-136

Kanevskiy M *et al* 2013 Ground ice in the upper permafrost of the Beaufort Sea coast of Alaska *Cold Regions Science and Technology* **85** 56-70

Lantuit, H and Pollard W H 2005 Temporal stereophotogrammetric analysis of retrogressive thaw slumps on Herschel Island, Yukon Territory *Natural Hazards and Earth System Sciences* **5** 413-423

Lantuit H and Pollard W H 2008 Fifty years of coastal erosion and retrogressive thaw slump activity on Herschel Island, southern Beaufort Sea, Yukon Territory, Canada *Geomorphology* **95** 84-102

Lantuit H, Rachold V, Pollard W H, Steenhuisen F, Ødegård R and Hubberten H W 2009 Towards a calculation of organic carbon release from erosion of Arctic coasts using non-fractal coastline datasets. *Marine Geology* **257** 1-10

Lantz T C and Kokelj S V 2008 Increasing rates of retrogressive thaw slump activity in the Mackenzie Delta region, NWT, Canada *Geophysical Research Letters* **35** L06502

Liu L, Zhang T and Wahr J 2010 InSAR measurements of surface deformation over permafrost on the North Slope of Alaska *Journal of Geophysical Research* **115** F03023

Marsh P, Russell M, Pohl S, Haywood H and Onclin C 2009 Changes in thaw lake drainage in the Western Canadian Arctic from 1950 to 2000 *Hydrological Processes* **23** 145-158.

McClelland J W, Déry S J, Peterson B J, Holmes R M and Wood E F 2006 A pan-arctic evaluation of changes in river discharge during the latter half of the 20th century *Geophysical Research Letters* **33** L06715

National Climate Data Center (NCDC) 2013 <http://www.ncdc.noaa.gov/cdo-web/>
Osterkamp T E 2003 Establishing long-term permafrost observatories for active layer and permafrost investigations in Alaska: 1977-2002 *Permafrost and Periglacial Processes* **14** 331-342

Overeem I, Anderson R S, Wobus C W, Clow G D, Urban F E and Matell N 2011 Sea ice loss enhances wave action at the Arctic coast *Geophysical Research Letters* **38** L17503

Ping C L, Michaelson G J, Jorgenson M T, Kimble J M, Epstein H, Romanovsky V E and Walker D A 2008 High stocks of soil organic carbon in the North American Arctic region *Nature Geoscience* **1** 615-619

Ping C L *et al* 2011 Soil carbon and material fluxes across the eroding Alaska Beaufort Sea coastline *Journal of Geophysical Research* **116** G02004

Raynolds M K *et al* In Review Cumulative effects of 62 years of infrastructure and climate change in ice-rich permafrost landscapes, Prudhoe Bay Oilfield, Alaska *Proceedings of the National Academy of Science* Submitted 26 August 2013

Ritchie J C 1995 Airborne laser altimeter measurements of landscape topography *Remote Sensing of Environment* **53** 91-96

Romanovsky V E and Osterkamp T E 1995 Interannual variations of the thermal regime of the active layer and near-surface permafrost in Northern Alaska *Permafrost and Periglacial Processes* **6** 313-335

Romanovsky V E, Sergueev D O and Osterkamp T E 2003 Temporal variations in the active layer and near-surface permafrost temperatures at the long-term observatories in Northern Alaska. *In: Permafrost*, Phillips, M., S. Springman, and L.U. Arenson (eds.), Swets & Zeitlinger, Lisse, 989-994

Romanovsky V E, Smith S L and Christiansen H H 2010 Permafrost thermal state in the polar Northern Hemisphere during the international polar year 2007–2009: A synthesis *Permafrost and Periglacial Processes* **21** 106-116

Short N, Brisco B, Couture N, Pollard W, Murnaghan K and Budkewitsch P 2011 A comparison of TerraSAR-X, RADARSAT-2 and ALOS-PALSAR interferometry for monitoring permafrost environments, case study from Herschel Island, Canada *Remote Sensing of Environment* **115** 3491-3506

Smith S L *et al* 2010 Thermal state of permafrost in North America: A contribution to the International Polar Year *Permafrost and Periglacial Processes* **21** 117-135

Snyder N P 2009 Studying stream morphology with airborne laser elevation data *EOS Transactions AGU* **90** 45-46

Streletskiy D A, Shiklomanov N I, Nelson F E and Klene A E 2008 Thirteen Years of Observations at Alaskan CALM Sites: Long-Term Active Layer and Ground Surface Temperature Trends *Ninth International Conference on Permafrost Fairbanks* 1727-1732
Stroeve J C, Serreze M C, Holland M M, Kay J E, Malanik J and Barrett A P 2012 The Arctic's rapidly shrinking sea ice cover: a research synthesis *Climatic Change* **110** 1005-1027

Sultan N J, Braun K W and Thieman D S 2011 North Slope trends in sea level, storm frequency, duration and intensity *Ice Tech Conference Prudhoe Bay Paper No. ICETECH10-155-R0*

Walker D A *et al* 2008 Patterned-ground ecosystems: A synthesis of field studies and models along a North American Arctic Transect *Journal of Geophysical Research* **113** G03S01

White S A and Wang Y 2003 Utilizing DEMs derived from LIDAR data to analyze morphologic change in the North Carolina coastline *Remote Sensing of Environment* **85** 39-47

Woolard J W and Colby J D 2002 Spatial characterization, resolution, and volumetric change of coastal dunes using airborne LIDAR: Cape Hatteras, North Carolina *Geomorphology* **48** 269-287

5.11 Figures

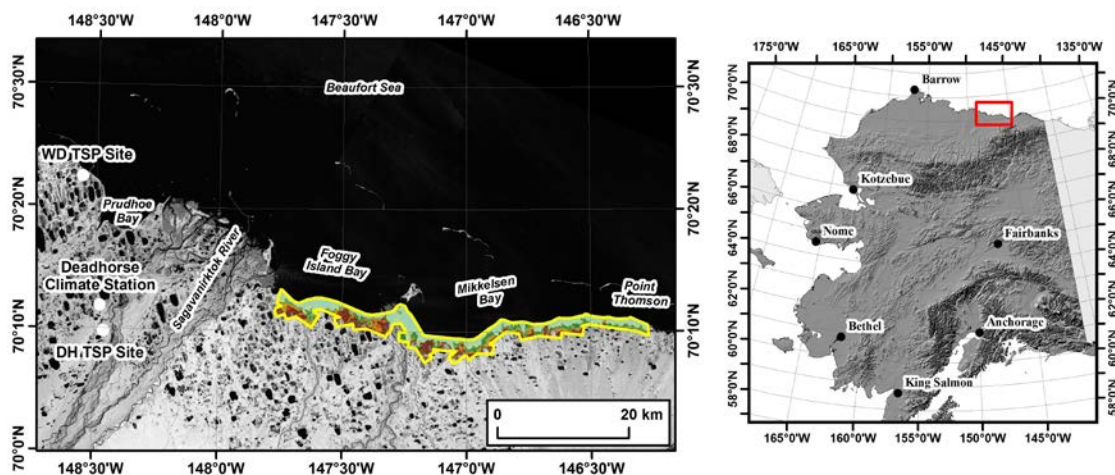


Figure 1. Repeat airborne LiDAR study area. The 100 km² repeat LiDAR study area on the central Beaufort Sea coastal plain is outlined with the yellow polygon. The background image is a 30 m resolution Landsat image. The climate station is the location of observations on mean annual air temperature and thawing degree day sums. The West Dock (WD) and Deadhorse (DH) Thermal State of Permafrost (TSP) observatories are the location of ground temperature data and active layer thickness measurements used in this study. The location of the study region (red box) in Alaska is shown in the map on the right.

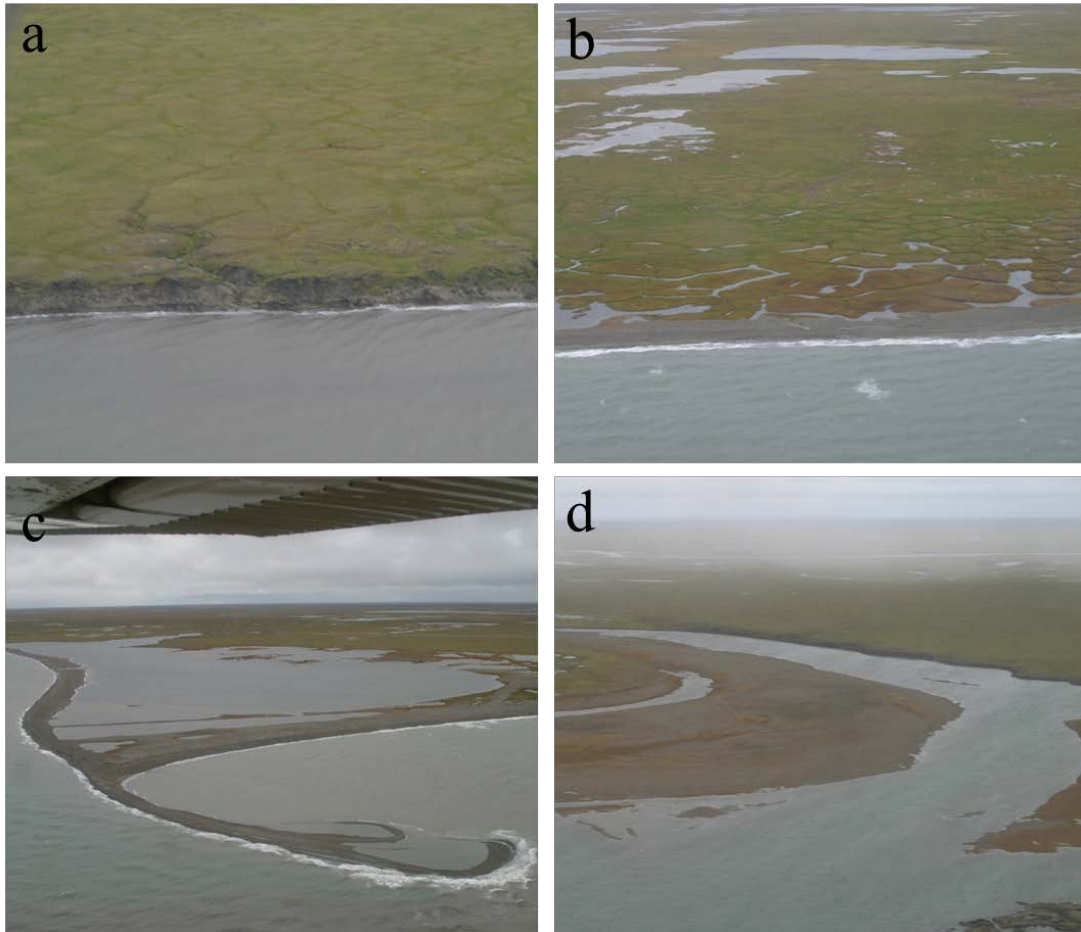


Figure 2. Oblique photos of features in the study region. Oblique photos from the study region acquired in 2006 showing the coastal setting and hinterland features (Gibbs and Richmond 2009). (a) A coastal bluff showing a thermo-erosional gully, thermo-denudation, and ice wedge polygons; (b) a coastal lowland setting showing degraded ice wedges, thermokarst ponds, and beach deposits; (c) spit and beach features enclosing a shallow lagoon; and (d) a low gradient river channel, river bar, and cut bank.

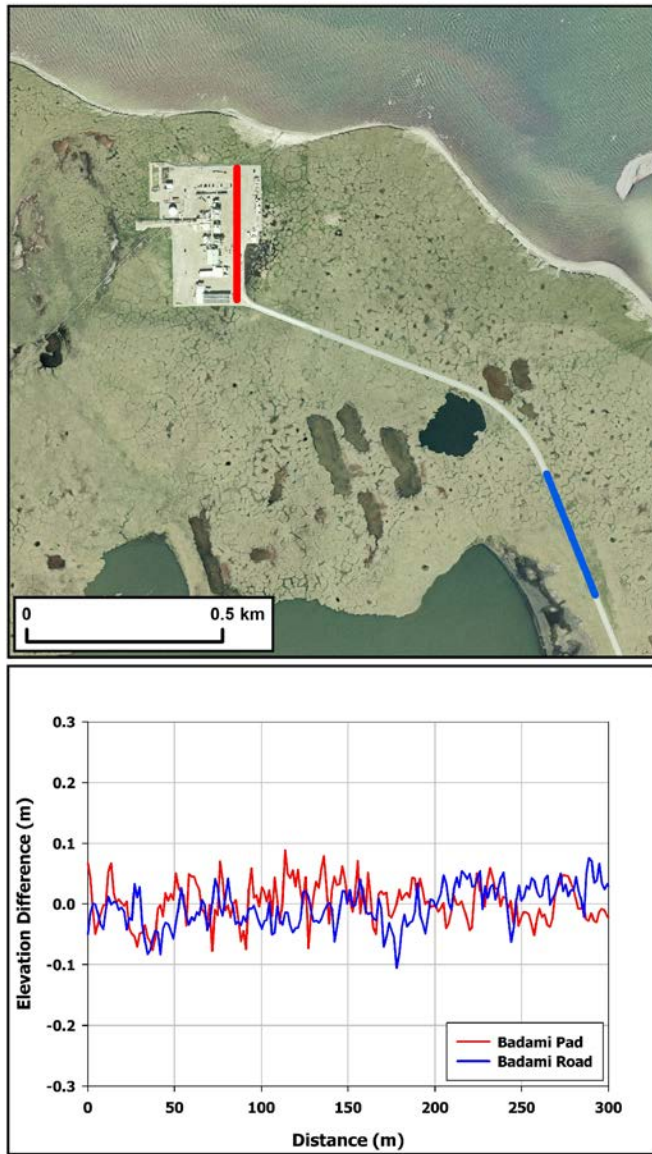


Figure 3. Example showing agreement between the two datasets. Detailed comparison between the 2006 and 2010 LiDAR datasets for presumed vertically stable features on an unvegetated land surface in the study area. The Badami oil field pad and road show that the difference in elevation between the two datasets is on the order of ± 0.1 m.

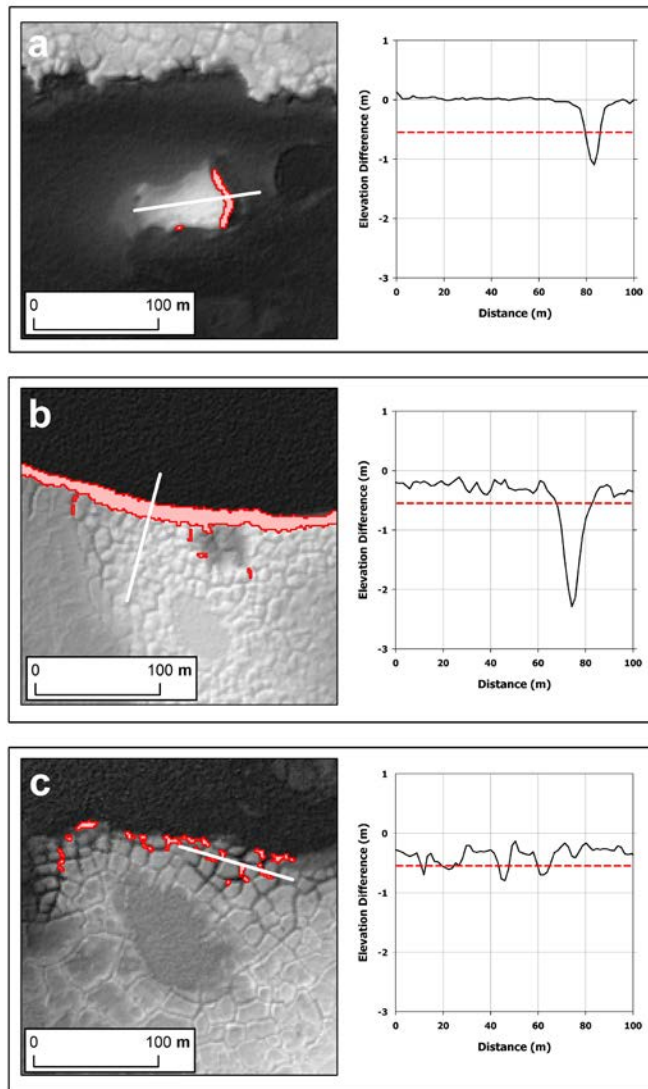


Figure 4. Examples of permafrost degradation features. Example of change detection results from the repeat LiDAR datasets showing a hillshade image on the left and elevation difference profiles on the right. The red polygons on the left indicate significant change objects as do the segments of the elevation difference profiles (taken from transects marked with white line on left) below the red dashed line. (a) Degradation of a frost mound in a drained thermokarst lake basin. Note the excellent agreement between the 2006 and 2010 profiles. (b) Erosion along a 4 m high coastal bluff. Thermokarst gully and thermokarst pit formation are also evident (similar to the setting in figure 2a). (c) Thermokarst pit formation in coastal lowland (similar to the setting in figure 2b). Note general lowering of the land surface in examples (b) and (c).

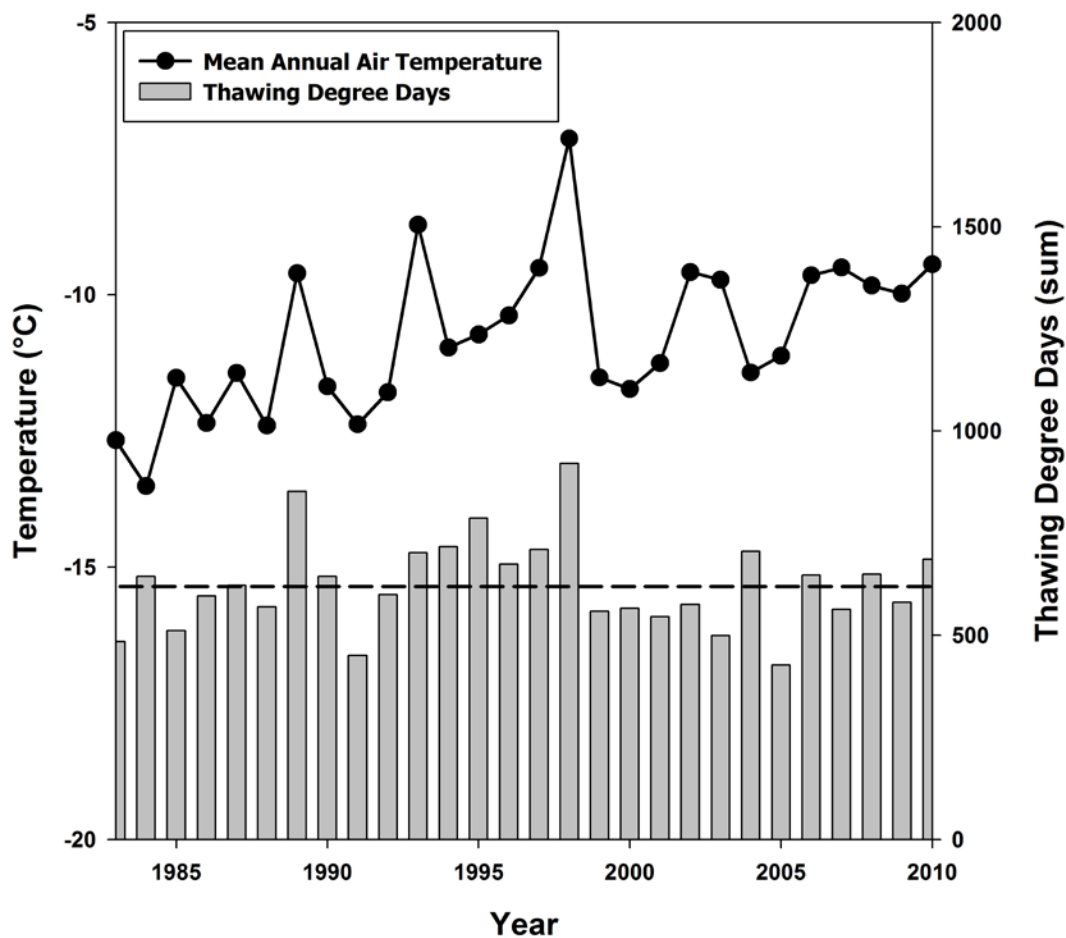


Figure 5. Air temperature and thawing degree day sums. Mean annual air temperature and summertime (June to September) thawing degree day sums from 1983 to 2010 for the Deadhorse, AK climate station (NCDC 2013). The dashed line indicates the mean value for TDD over the period of observation.

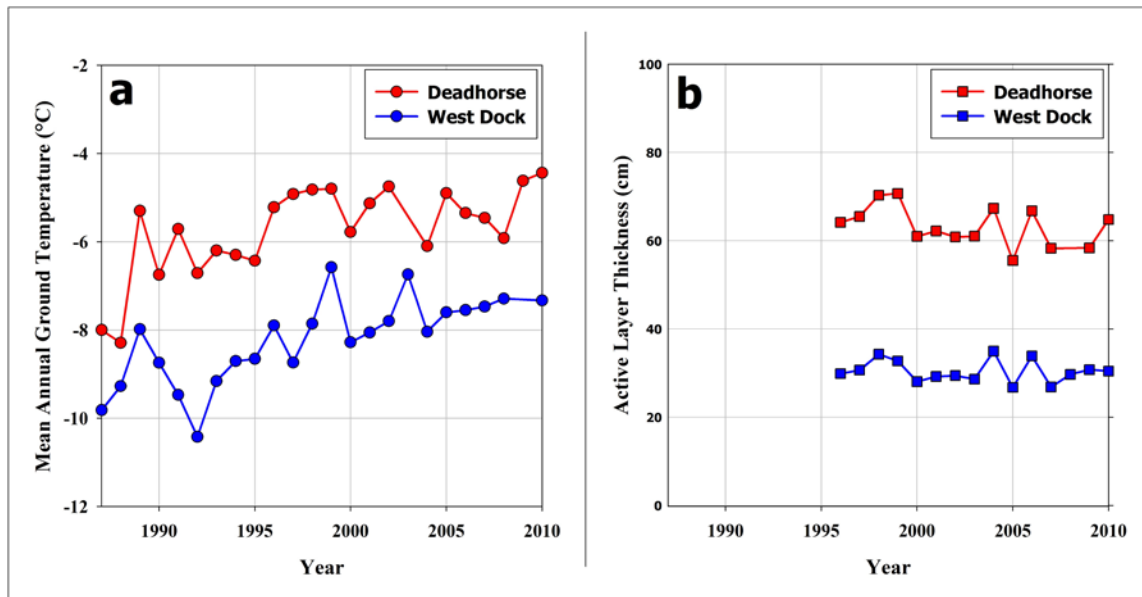


Figure 6. Permafrost temperature and active layer data. (a) Near surface permafrost temperature data measured at a depth of 70 cm and (b) active layer thickness measurements from the Deadhorse (DH) and West Dock (WD) Thermal State of Permafrost (TSP) sites between 1987 and 2010 and 1996 and 2010, respectively.

5.10 Tables

Table 1. Classified landscape change objects. Classified change objects in the repeat LIDAR study area. The table provides information on the type of feature, the number of discrete polygons greater than 10 m², the minimum, maximum, mean, and sum for 2-D and 3-D changes, and the rate of change in 2-D and 3-D space.

Feature Type	Number	Area (m ²)				Vertical Change (m)				Change Rate	
		Minimum	Maximum	Mean	Sum	Minimum	Maximum	Mean	Sum	Area (m ² /yr)	Volume (m ³ /yr)
Coastal Bluff Erosion	341	11	20115	360	123020	0.6	4.4	0.8	60541	30755	1861938455
River Bluff Erosion	113	11	648	61	6903	0.6	3.8	0.8	2780	1726	4797585
Thaw Slump	24	11	266	48	1161	0.7	1.6	0.8	452	290	131193
Thermokarst Lake Erosion	15	11	884	115	1725	0.7	2.4	0.9	889	431	383381
Thermokarst Pit	344	11	70	18	6237	0.6	1.0	0.7	1872	1559	2918916
Thermo-erosional Gully	43	11	250	29	1229.1	0.7	1.8	0.7	407	307	125061
Heave Features	42	11	131	25	1064	0.6	1.4	0.8	388	266	103208
Beach/Spit Erosion	451	11	11724	295	133112	0.6	2.6	0.7	51988	33278	1730056664
Delta/River Bar Erosion	124	11	693	55	6846	0.6	1.3	0.7	2178	1712	3727647
Dune Erosion	20	11	72	26	528	0.6	0.9	0.7	159	132	20988
Beach/Spit Deposition	194	11	2218	129	25148	0.6	1.6	0.7	8568	6287	53867016
Delta/River Bar Deposition	3	11	171	70	209	0.6	1.0	0.8	67.5	52	3527
Dune Deposition	4	11	52	22	88	0.6	1.3	0.8	32	22	704

Chapter 6: Summary

6.1 Overview

Surface air temperatures in the Arctic have warmed by $\sim 0.35^{\circ}\text{C}$ per decade between 1970 and 2000, which is two times faster than the average global rate of warming [Serreze and Francis, 2006]. In turn, permafrost has warmed throughout much of the Northern Hemisphere since the 1980s, with colder permafrost sites warming more rapidly than warmer permafrost sites [Romanovsky et al., 2010; Smith et al., 2010]. Warming of the near surface permafrost may lead to widespread terrain instability in ice-rich permafrost deposits in the Arctic and result in thermokarst development and other thaw-related landscape features [Jorgenson et al., 2006; Gooseff et al., 2009]. However, information on rates of landscape change as well as the spatial and temporal distribution of landscape disturbances remains limited. For my dissertation, I assessed four different facets of permafrost-related, arctic landscape dynamics using remote sensing. In particular, I focused on permafrost coastline erosion, thermokarst lake dynamics, fire-related arctic landscape change and disturbance, and the quantification of surface deformation using repeat airborne LiDAR data. Information from each of these studies demonstrates the utility of and need for applying high spatial resolution remote sensing for change detection studies in the Arctic.

6.2 Dissertation results

In Chapter 2, the acquisition of high-spatial resolution satellite imagery at high-temporal resolution between 2008 and 2013 allowed for the quantification of bluffline erosion rates on annual and seasonal scales [Jones et al., *In Review*]. This analysis

showed that the heightened erosion reported at Drew Point in the early to mid-2000s has generally been maintained. This annual-scale imaging of the permafrost bluffs also allowed for the comparison to several environmental variables thought to play a role in driving the rate of erosion. This analysis showed that the erosion of the permafrost bluffs at Drew Point has directly responded to an increase in the number of open water days and the number of storms impacting this coastline. These increases have likely resulted in an increase in the number of block collapse episodes per year.

In Chapter 3, I assessed the decadal-scale dynamics of thermokarst lakes on the northern Seward Peninsula using historical aerial photography and contemporary satellite imagery [Jones et al., 2011]. Surprisingly, decadal-scale thermokarst lake expansion rates have remained stable (~ 0.35 to 0.39 m/yr) from the 1950s to 1980s and 1980s to 2000s. Maximum measured expansion of lakes was on the order of 5 to 6 m/yr and approximately half of the lakes in the study region showed signs of lake expansion. Even though lake expansion was the prevailing mechanism driving lake change, lakes drained at a fairly constant rate (~ 2 lakes/yr) between the two time periods under observation. In the first time period the expansion of lakes and drainage of lakes offset one another, however, in the second time period the drainage of several large lakes resulted in three times more land gain relative to land loss. These observations were somewhat surprising given the reported lake change observations from other continuous permafrost regions. They also highlight the complexities associated with the role of thermokarst lakes in the northern high latitude carbon cycle.

In Chapter 4, I combined field surveys with remotely sensed data to demonstrate the ability to extend the northern Alaska fire history database beyond the late-1940s (the beginning of the remote sensing period for the region) [Jones et al., 2013]. This research was guided by the question: Was the Anaktuvuk River fire of 2007 unprecedented on the North Slope of Alaska? In order to address this question, I combined field observations with satellite imagery from past known tundra fire sites in northern Alaska in order to develop diagnostic characteristics of landscape change following fire. This information was then combined with aerial observations from the North Slope loess belt, historical aerial photography, high-resolution satellite imagery, and Landsat satellite imagery to identify other potential fire sites that likely predated the period of record keeping that began in the late-1940s. This coupled analysis essentially demonstrated how information could be used to extend the observations on tundra fire events beyond the remote sensing archive period by utilizing the remote sensing archive. It also demonstrated that other large tundra fire events occurred on the North Slope prior to 2007. Identification of these sites also provides a centennial scale chronosequence in which to study landscape change and carbon cycling associated with arctic tundra fires.

In Chapter 5, I highlight the utility of acquiring repeat airborne LiDAR data for quantifying vertical surface deformation in an arctic coastal lowland [Jones et al., *In Press*]. I demonstrated that it is possible to detect and characterize a number of thaw-related and non-thaw-related landscape changes occurring in arctic coastal lowlands with the use of repeat airborne LiDAR data. Erosion of ice-bonded coastal and river bluffs, thaw slumping, thermokarst lake expansion, thermokarst pit subsidence, and thermo-

erosional gully expansion indicated ice-rich permafrost degradation and accounted for nearly half of the area and half of the volume change that occurred over the four year study period. Erosion and deposition associated with beach and spit deposits, riverine and deltaic flats, and sand dunes accounted for the majority of the remaining significant landscape change. This study demonstrates the utility of assessing landscape change in permafrost dominated landscapes with repeat airborne LiDAR data, in particular for spatially small but widespread permafrost thaw-related processes. This is the first study to attempt this in the Arctic and I hope that it will lead to the acquisition of repeat LiDAR data in other permafrost terrain in the future.

6.3 Future directions

As previously mentioned, remote sensing provides an excellent tool for observing, documenting, and better understanding landscape change in the Arctic from local, to regional, to pan-Arctic scales. It has emerged as one of the primary tools for advancing the field of thermokarst research [Kokelj and Jorgenson, 2013]. Rowland et al. [2010] noted that with the scale of questions and facets of landscape change in the Arctic that “a particular focus must be placed on identifying existing and developing new remote sensing technologies to detect near-surface and subsurface changes in the Arctic”. With an increase in the number of high-resolution optical satellite observations since the early-2000s, the quantification of climate-induced landscape change and disturbance over large areas in the Arctic is now possible. However, analysis of high-resolution optical satellite imagery remains limited due to the often manually intensive classification and extraction techniques. Future work should be dedicated to the automated extraction of various

thermokarst and thaw-related landscape features in high-resolution imagery such that regional and pan-Arctic patterns of the response of the landscape to ongoing climate change in the Arctic will be realized. Also, going forward, the acquisition of repeat airborne or spaceborne LiDAR data will prove to be a valuable tool for the study of arctic landscape dynamics.

6.4 References

Gooseff, M. N., A. Balsler, W. B. Bowden, and J. B. Jones (2009), Effects of hillslope thermokarst in northern Alaska, *Eos, Transactions American Geophysical Union*, 90(4), 29–36.

Jones, B. M., A. L. Breen, B. V. Gaglioti, D. H. Mann, A. V. Rocha, G. Grosse, C. D. Arp, M. L. Kunz, and D. A. Walker (2013), Identification of unrecognized tundra fire events on the north slope of Alaska, *Journal of Geophysical Research* 118, doi:10.1002/jgrg.20113.

Jones, B. M., G. Grosse, C. D. Arp, M. C. Jones, K. M. W. Anthony, and V. E. Romanovsky (2011), Modern thermokarst lake dynamics in the continuous permafrost zone, northern Seward Peninsula, Alaska, *Journal of Geophysical Research Biogeosciences* 116, G00M03, doi:10.1029/2011JG001666.

Jones, B. M., G. Grosse, C. D. Arp, and J. Zhang (*In Review*), High spatial and temporal resolution remote sensing of a rapidly eroding segment of arctic coastline, *Remote Sensing*.

Jones, B. M., J. M. Stoker, A. E. Gibbs, G. Grosse, V. E. Romanovsky, T. A. Douglas, N. E. M. Kinsman, and B. R. Richmond (*In Press*), Quantifying landscape change in an arctic coastal lowland using repeat airborne LiDAR, *Environmental Research Letters*.

Jorgenson, M. T., Y. L. Shur, and E. R. Pullman (2006), Abrupt increase in permafrost degradation in Arctic Alaska, *Geophys. Res. Lett.*, 33, L02503, doi:10.1029/2005GL024960.

Kokelj, S. V., and M. T. Jorgenson (2013), Advances in Thermokarst Research, *Permafrost and Periglacial Processes*, 24(2), 108-119.

Romanovsky, V. E., S. L. Smith, and H. H. Christiansen (2010), Permafrost thermal state in the polar Northern Hemisphere during the international polar year 2007–2009: A synthesis, *Permafrost and Periglacial Processes*, 21, 106-116.

Rowland, J. C., et al. (2010), Arctic landscapes in transition: Responses to thawing permafrost, *Eos, Transactions American Geophysical Union*, 91(26), 229-230.

Serreze, M. C., and J. A. Francis (2006), The Arctic amplification debate, *Climatic Change*, 76, 241-264.

Smith, S. L., et al. (2010), Thermal state of permafrost in North America: A contribution to the International Polar Year, *Permafrost and Periglacial Processes*, 21, 117-135.